LONG-RANGE COULOMB INTERACTION FOR REACTIVE ATOMISTIC SIMULATIONS: APPLICATION TO GRAPHENE-WATER CAPACITORS

NWANKWO UDOKA

PhD

The Hong Kong Polytechnic University

2023

The Hong Kong Polytechnic University

Department of Applied Physics

Long-range Coulomb Interaction for Reactive Atomistic Simulations: Application to Graphene-Water Capacitors

NWANKWO Udoka

A thesis submitted in partial fulfilment of the requirement for the degree of Doctor of Philosophy

January 2023

Certification of Originality

I hereby declare that this thesis is my own work and that, to the best of my knowledge and belief, it reproduces no material previously published or written, nor material that has been accepted for award of any other degree or diploma, except where due acknowledgement has been made in the text.

NWANKWO Udoka

Abstract

Electrochemical processes often govern contemporary energy storage and electronic devices. Despite the significant signs of progress achieved toward unveiling the properties of these devices, the mechanisms that control their operations are not fully understood, especially at the atomic level. Besides experiment limits, atomistic simulations can provide unprecedented insights and details about the processes and improve device development. Atomic description of these systems requires reactive interaction potential to be able to describe (i) the chemistry between atoms and those existing in molecules and (ii) the evolving charge distribution and polarization effects. Calculating Coulomb electrostatic interactions and polarization effects required a more accurate estimate of partial charge distribution in molecular systems, at least for the proper prediction of the stability and solubility of the system. To this purpose, the applications of many-body, partial bond-order potential alongside geometry-dependent partial atomic charge evaluation scheme led to the development of reactive force fields such as ReaxFF and the charge equilibration (QEq) models used in reactive molecular dynamics (MD) simulations. However, these models include Coulomb interactions up to only a short-range distance cut-off for better computational speeds, limiting the computation of Coulomb interaction up to a short distance around an atom. Ignoring long-range (LR)/distance electrostatic interaction affects the ability to describe electrochemistry in large systems. We emphasize evaluating and including long-range effects on partial charge and atom force calculations; and we investigate the long-range Coulomb effects among charged particles. By extending a QEq method to include long-range effects, we anticipated a proper account of Coulomb interactions in reactive molecular dynamics simulations. We validate the approach by computing charges on a series of metal-organic frameworks and some simple systems. Results are compared to regular QEq and quantum mechanics (QM) calculations. The study shows slightly overestimated charge values in regular QEq approach. Moreover, our method was combined with Ewald summation to compute forces and evaluate the long-range effects in simple capacitor configurations. There were noticeable differences between the calculated charges with/without long-range Coulomb interactions. The difference, which may have originated from the long-range influence on the capacitor ions, makes the Ewald method a better descriptor of Coulomb electrostatics for charged electrodes. The approach explored in this study enabled the atomic description of electrochemical systems with realistic electrolyte thickness while accounting for the electrostatic effects of charged electrodes throughout the dielectric layer in devices like batteries and emerging solid-state memory.

List of Publications

Nwankwo, U., Lam, C.-H., Wang Y.-D. & Onofrio, N. (2023). Charge equilibration model with shielded long-range Coulomb for reactive molecular dynamics simulations. *Journal of Chemical Physics. (*Submitted)

Nwankwo, U., Lam, C.-H., & Onofrio, N. (2023). Reactive molecular dynamics simulations of graphene-water capacitor using QEq and ReaxFF with Long-range Coulomb. Journal of Physical Chemistry C. (Submitted).

Acknowledgements

The journey may have been rough and tough, but the experiences and knowledge gained are worthwhile, and would be cherished for life. Measuring from the starting point of this study and in retrospect over the past years, I have overwhelming reasons to be grateful to God almighty and would like to appreciate individuals and bodies who directly or indirectly availed me the opportunity for "a life journey of experience and knowledge" at the Hong Kong Polytechnic University. Among the recipients of my profound gratitude are my supervisors: Dr Nicolas ONOFRIO for introducing me to the field of computational material science and simulations; and Dr Chi-Hang LAM for their unwavering patience and tolerance, criticisms and directives, and overhaul of ideas that helped shape this work to its present status.

I am thankful to the Hong Kong Polytechnic University and the department of Applied Physics for the computing resources, and for the fund provided by the University Grants Committee (UGC) and the Research Grants Council (RGC) of Hong Kong for the smooth running of my PhD program. I, at large, thank the staff of AP and PolyU for their meekness and organizational adequacy in handling issues relating to students' study.

Special thanks to my friend and brother Maduka MADUKA (PhD) for all we toiled together here in Hong Kong and back home. I also take this time to remember and thank ANI Elizabeth Chinonso for trusting me and for the often you called to ask about my welfare and study and give suggestions and words of encouragement. Special and big thank you to Miss Onyinye Joy IKENYIRIMBA for the day-to-day spiritual, emotional, bodily, and soul contributions that incessantly added oil to the finishing of this task. Indeed, you are an exceptional personality, a treasure, an icon to behold and for your humane attributes, dispositions, and composure, I thank God immensely and remain appreciative of you believing and trusting in me, dearly. Lastly, I seize this opportunity to say a "Big Thank You" to friends who have been in touch with me and have contributed via calls and messages.

Finally, I remain loyal and humble to one and only A. O. Nwankwo's family, viz: Papa, Mama, siblings (sister Chinedu, Ukamaka, Oluchi and Chiamaka; brother Solomon, Friday and Okechukwu) and relatives, I doff my cap for you all for the encouragements, prayers, and good wishes during these years of toiling in "a life journey of experience and knowledge". It looked as if everything was in wait; yet no one gave up on me. I remain grateful to God and to you all.

Table of Contents

List of Figures

List of Tables

Chapter 1

Introduction

1.1 Background Overview

Electrochemical processes are ostensibly established technologies based on the relationship between electricity and chemical change, for which either a chemical change is observed as an outcome of an applied electric potential, or an electric power is viewed as a measurable quantitative result of a chemical change. Over the years, electrochemical processes have evolved as an innovative technology for the production and assembly of many electronic components ranging from portable and wearable consumer products to innovative, top-of-the-line microchips and processors. Electrochemical processing technology generically involves the formation and dissolution of conductive paths within a continuous layer (dielectric material), which permits electronic and/or ionic motion(s) from one edge of a metallic contact to the other at the application of a bias. These processes play key decisive roles in the advancement of micro- and nano-electronics industries.

In addition to energy storage application [1], [2], electrochemical processes have tremendous usefulness in nano-electronics [3], [4], neuromorphic and general computing systems [5], [6], biochemical sensors [7], and nano-material processing. In any application, the operations of these electrochemical devices, e.g., batteries [1], [2], electrochemical metallization (ECM) cells [5], [8] (also called conductive bridging random access memory (CBRAM) cells or programmable metallization cells (PMC) in some literature), electric double-layer (EDL) [7], [9], [10] transistors, capacitors and fuel cells are underpinned by phenomena that are originating from interplay reactions between electrodes and electrolyte. At various length and time scales, the interplay reactions are essential for filament formation and dissolution, electronic and ionic motions. Such phenomena include but are not limited to, ion diffusion and nucleation (aggregation), electron and hole transport, trapping, and clustering, electrode-electrolyte phase change, Joule heating, charge diffusion and polarization. In attempts to comprehend these phenomena accompanying electrochemical reaction, many experimental as well theoretical measurements have been done with the goal of optimizing the device performance and widening their potential application. In this regard, electrode porosity [11], [12], electrode thickness [13], and electronic transport in electrodes [10], [14], [15] have

been studied and classified among the rate-limiting factors affecting the performance of electrochemical devices. Cyclic voltammetry experiments [3] have enabled, to a certain extent, the explanation of some underlying principle behind the operation of these electrochemical devices; in particular, the retention and endurance properties of ECM [3], [16] cells; the rate performance, charge storage capacity, charge transport, and densities in batteries [15] and the ion concentration and density, conductivity and capacitance of EDL capacitors and thin-film transistors [17]. Notably, some of these devices especially ECM cells and EDL transistors are scalable down to nanoscale sizes and operate at nanoseconds timescale [18], within which detailed quantitative information that sustains their properties such as ultrafast resistive switching [8], [18], are not fully understood via microscopy, cyclic voltammetric measurement and other experimental techniques based on lack of spatial and temporal resolutions [19], [20]. The most common 3D virtualization is by conductive atomic force microscopy (C-AFM) [21] analysis, which enables filaments to be observed in the single-digit nm range. Yet, it is still very difficult to understand the resistance-switching phenomena in terms of detailed chemical processes; see [22]. A recent review [23] article on the history, status, and future of resistive random-access memories (ReRAM) noted that conductive filament stability depends on the total number of defects in the filament and attains optimum at the maximum current for, which the resistant state of the device switches to low. While it is recorded in the literature [22], [23] that low defect density of the resistive switching filaments poses a significant hurdle to characterizing devices' physical properties, it will be worthwhile to atomistically observe the filament growth at various applied potential and device sizes to monitor how defects in filaments populate.

Interestingly, beyond experiment limits down to the nanoscales, atomistic simulation can help understand certain phenomena that affect the operation and properties of ECM cells and vividly shed light on the intricacies at the atomic level that result in, for instance, the ultrafast resistance switching in ECM [8], [18] cells. Atomic simulation or description of these systems requires reactive interatomic potential or at least the calculation of interatomic interactions [24] to be able to describe the chemistry between atoms and molecules, and the evolving charge distribution and polarization effects. Calculating interatomic interactions, specifically Coulomb electrostatic interaction requires a good estimate of partial atomic charges in a molecular system, at least for the proper prediction of the systems stability, solubility, and free energy [25]. The practice of estimating partial atomic charges starts on non-localized interacting systems, in which the electronic structure of systems is determined using either

Eigen-function-based and electron-density-based approaches or *ab initio* calculations, usually at the level of density functional theory (DFT) approximations. These methods are found accurate, reliable, and applicable to all systems, not just for predicting atomic charges but also in predicting various chemical properties. However, electrochemical systems, in particular, ECM cells are too large for many particles to be investigated with *ab initio* molecular dynamics (MD) simulation; luckily enough, reactive interatomic potential [26], [27] capable of simulating complex chemical reactions have been developed and paved way for classical MD method.

ReaxFF [28] is an example of reactive force fields that is capable of describing dynamical atomic interactions in molecular and atomic systems that encompass covalent and electrostatic (van der Waals and Coulombs) interactions. In most developments and applications of ReaxFF, dynamical partial charge calculation is allowed through an environment-dependent charge equilibration (QEq) [29] technique. ReaxFF, just like any other method for computing interaction potential and forces, gives an approximate description of the interactions. One of the approximations entertained in ReaxFF as well as in QEq is the tactical treatment of electrostatic (Coulomb) interaction. A short distance is applied to the interaction potential for computational speed, thereby limiting its description of electrostatic interactions only to a short-distance order. It is noted that ignoring long-range distance electrostatic interactions (see [30]) affects the ability to describe electrochemistry in large systems such as electrochemical metallization cells [18], [31].

On another hand, the study of electrochemical processes have involved the demonstration of the influence of electrodes [32], [33] and/or electrolyte [34] materials, device geometry [8], electrode porosity [11], [12], electrodes geometric asymmetry [35], electrode thickness [12], [13], [14], among others on the characteristic properties of an electrochemical device. Research on the origin of ultrafast resistive switching [18] of ECM cells traced the ultrafast resistive switching mechanism to have atomic origin in the nanoscale spatial and time limits though stressed that cell geometry as well dielectric structure and its interface with electrodes affects the switching time [36]. In another study [8], the entire device geometry is investigated for the understanding of the ultrafast resistive switching at the nanoscale limit. Effect of geometric asymmetry [35], which results from different sizes of working and counter electrodes or a shift of an electrode from one another on half cell impedance of a cell has been studied with point-like, wire, and mesh reference electrodes. A study on the influence of counter-electrode material [32] on the SET kinetics of resistive switching mechanism of ECM cells shows that

concentration of a metal ion in counter-electrode/electrolyte interface influences both ion nucleation and filament growth. Despite this great deal of investigations and progress towards understanding the mechanism of operation of these devices and improving the device's performance, the knowledge of some factors in the functioning of nanoscale cells is lacking. Presently, there is limited understanding of how electrode separation affects the operation of nanoscale cells of realistic size; knowledge of electrode separation would help further develop the technology. Moreover, to these days, investigating reactive actions in electrochemical devices are impeded by the tacit imposition of short-distance cut-off, which does not guarantee correct description of long-range Coulomb interaction among atoms in a configuration under test. Preliminary investigations on using the hybrid of ReaxFF and long-range (Ewald) Coulomb pair potential in LAMMPS [37] to achieve a full description of Coulomb interaction with/without shielding functions produced results that differ greatly from the long-range Coulomb interactionvia Ewald or analytical counterparts.

Following the above discussions, this thesis gains impetus to present short overviews of the Coulomb interaction forces between atomic or molecular systems, and charge equilibration technique implemented in MD simulator codes such as LAMMPS. We identify limitations, problems and gaps in the current techniques where Coulomb interactions are non-trivial, and areas where further development is required for optimum performance of these models in reactive molecular dynamics simulations. We re-visited split charge equilibration (SQE) method [38] and show that while it solves the key shortfalls of QEq, it is conformation-dependent and strictly applicable to evaluating partial atomic charge in covalently bonded molecular systems. Then after, we include shielded long-range Coulomb effect to electrostatic Coulomb potential for partial atomic charge computation and integrate long-range Coulomb potential function with shielding correction in ReaxFF. This guarantees proper non-bonded electrostatic or shielded electrostatic (for atoms separated at a remarkably close distance of van der Waal's diameter between atom pairs) interactions and enables the atomistic simulation of an electrochemical device without restricting Coulomb interaction within a region. The aim and objectives of the study are summarized in the next sub-section.

1.2 Thesis Aim and Objectives

Following the above discussion, it is a common knowledge that to describe electrostatic interactions according to the simple Coulomb's law, Eq. (1.1) or the electrostatic potential energy between charged bodies separated by a distance r_{ij} (where f_{ij} represents the magnitude

of the force on particle i with charge q_i due to its interaction with particle j having charge q_j and k_C = Coulomb constant) the partial charges of the atomic or molecular systems are needed.

$$f_{ij} = k_C \frac{q_i q_j}{r_{ij}^2} \qquad 1.1$$

For the required charges of the atoms, this study emphasizes evaluating and including long-range effects into partial charge calculations and atomic forces and applying the model to study some capacitive devices. The following highlights the facets of objectives for achieving the aim of the study:

1. Develop a charge estimation method called QEq long-range (QEqLR = LrQEq) for partial atomic charge computation. In QEqLR, we will describe the Coulomb electrostatic interaction between atoms via the Ewald [39] summation technique to include the long-range effects. The derivation of the mathematical equations will follow after the method developed by Rappé and Goddard [29].
2. Implement QEqLR Coulomb in the MD simulator package called LAMMPS [37]. LAMMPS is an open-source package for material modeling and simulation; therefore, we will write an open-source package to distribute freely to the research community. The implementation will involve creating a fix QEqLR source code in our modified version of LAMMPS. These can generate atomic partial charges once LAMMPS is recompiled and necessary subsidiary parameters and input files supplied.
3. Implement long-range Coulomb with shielding function in reactive force fields and shielded long-range Coulomb for general electrostatic Coulomb interactions in LAMMPS. To achieve this objective, we will create a non-bonded electrostatic interaction potential file in the ReaxFF of LAMMPS software to include the long-range Coulomb interaction. And will write a stand-alone shielded long-range Coulomb interaction potential file. The implementations will use the Ewald summation method. The short-range (real space) contribution to the Coulomb energy and force will be according to the mathematical equations (Eqs 4.4 – 4.7) expressed in this work.
4. Combine the long-range Coulomb ReaxFF force field with QEqLR and study graphene-water capacitors to analyze the electrode polarization behavior and other properties and explore the role of electrode separation and applied potential on the capacitive behavior of the device.

1.3 Thesis Organization

Chapter one is an introduction to the background of the work and contains the thesis aim and objectives, outline, or organization.

Chapter two started with a literature review of general concepts like electrified interfaces. Explicitly, it briefly discussed batteries, capacitors, or electric double layers (EDL), and ECM cell memory as areas of significance and applicability of the research. The literature continued in the next chapter.

Chapter three introduces the molecular dynamics methods employed in this thesis and the underlying levels of physical and computational theories and approximations discussed in appropriate textbooks and publications. The simulation methods briefly surveyed are atomic and molecular modeling and quantum molecular mechanics (QM). And those discussed broadly include the classical force field method. Up to this chapter, the thesis design is to build a background that is required to comprehend the essence of the formulation of the long-range charge equilibration method. Therefore, in this chapter and the next, several frameworks may be introduced, mentioned, and briefly explained for brevity, clarity, and understanding of the main concepts.

Chapter four is the model development. It has two broad subsections: the first part treats the force model and the implementations of the shielded long-range Coulomb interaction for reactive force fields. The second section is the charge model, which includes the mathematical derivations of the conventional QEq, SQE, and QEqLR methods, which we implemented in the next chapter. Some concepts introduced in the previous chapter played important roles at this point.

Chapter five includes computer implementations, computations, and validations of the methods and some early applications, results, and discussions.

Chapter six is the application of the models to graphene–water systems and analyzes the device under zero and non-zero applied potentials and at various interelectrode separations.

Chapter seven concludes with the findings of the study.

Chapter 2

Review of Electrified Interfaces

In bulk materials, strong electro-neutrality assumptions may be valid but break down at the surface close to where charges see an uneven environment and experience unequal forces. Within the interfacial surfaces are regions dominated by oppositely charged particles. A localized electric field and a potential difference generated in the interface region of charges are the results of charge separations. These surfaces are called electrified surfaces. Electrochemical systems are composed of charged interfaces between electrodes and electrolytes; examples: solid-liquid boundaries in a battery, metal-insulator-metal interfaces in memory or conducting bridging cells and logic-gate systems, and metal-liquid surfaces in electrochemical double-layer devices. While complex electrochemical reactions such as ionic diffusion, interaction, aggregation, and depletion occur at the interfaces, electronic transport happens within and across the electrolyte, and in some cases, with the formation of microscopically observable conductive paths. These interfacial reactions undergird the importance of electrically charged interfaces in an electrochemical process such as batteries, fuel cells, electrochemical metallization cells (ECMs), and electric double-layer capacitors and transistors (EDLC and EDLT). The discussion in the following section captures brief literature on electrified interfaces of some electrochemical devices.

2.1 Battery

Batteries are in categories of primary cells, secondary cells, and reverse batteries. The primary batteries consist of chemical materials that are not electrically rechargeable once discharged. The secondary batteries are several times electrically rechargeable. The third category is configured for long-term storage in a way that the electrodes are separated from the electrolyte and inserted when needed or the electrolyte is a solid that melts when heated [40]. Rechargeable batteries are electrochemical energy storage devices, which have applications in not only mobile/portable devices such as phones and laptops, but also heavy equipment/machines encouraged nowadays by the advances of Li-ion battery technology [41]. Despite the progress made towards the advancement of this technology, Li-ion batteries still have low resistance (short-circuit) and dendrite formation-related challenges that could lead to thermal runaway failure [42], which raises safety concerns. Atomistic knowledge of the

processes involved in electrochemical energy storage is limited [43] based on the difficulty in observing from point of start of the reactions underpinning the functioning of the devices. A fundamental approach is to use experimental investigation; however, tools such as microscopy often give a poor understanding of the electrodes/electrolyte interfaces due to a lack of spatial and temporal atomic resolution [44]. An alternative method is to revert to the theoretical description, which depends on the experimental result as input [45] before a material's structures and processes going on in the material could be understood from the atomic to the microscopic level. It is on this background of reverting to a theoretical description that [46] benchmarked several semi-empirical models to estimate the formal electrode potential of organic molecules based on the energy differences approach (EDA) and orbital energy shift approach (OESA). The named semi-empirical or DFT models have possible predictive accuracy and could determine the redox potentials of molecules in a solution (due to the correlation between experiment and computation results [47]). But some model developments of electrochemical reactions with the electrode surfaces present involve small molecules such as H_2, OH^-, CO [48], [49], [50]. For performance, the charge density of a battery or the total charge stored in the battery is central to measuring capacity and performance rate [43]. Again, some state-of-the-art advances in electric and hybrid-electric vehicles (EV and HEV) [51] demand improvement in lithium-ion batteries (LIB) for high-rate performance through rapid charging and high-power delivery [15], [52]. But a quantitative experimental measurement of charge accumulation at the electrodes or electrode/electrolyte interface region is not easy to come by and is still desirable [53], [54]. Atomic simulation can lead the way but may require a realistic description of Coulomb interaction for improvement. Among these challenges, atomistic descriptions still have the solution to some important scientific questions about the chemistry and physics of electrified interfaces.

Working Principle of Battery. The diagrammatic description of the principle of operation of a battery looks simple compared to it in actual practice. Batteries, for example, the commercialized and rechargeable Li-ion batteries [55] comprise two electrodes a lithium graphite anode in contact with a copper current collector and a lithium metal oxide cathode in contact with the aluminum current collector, and the electrodes are dipped into a polymer membrane electrolyte Figure 2.1. The polymer electrolyte separates the two electrodes, permits ion diffusion back and forth between the electrodes through the electrolyte, but acts as an insulator for electron transport, thereby forcing electrons to propagate away from the separator

through to an external circuit where they do work [56]. [1] offers a detailed review of these processes in Li-ion batteries.

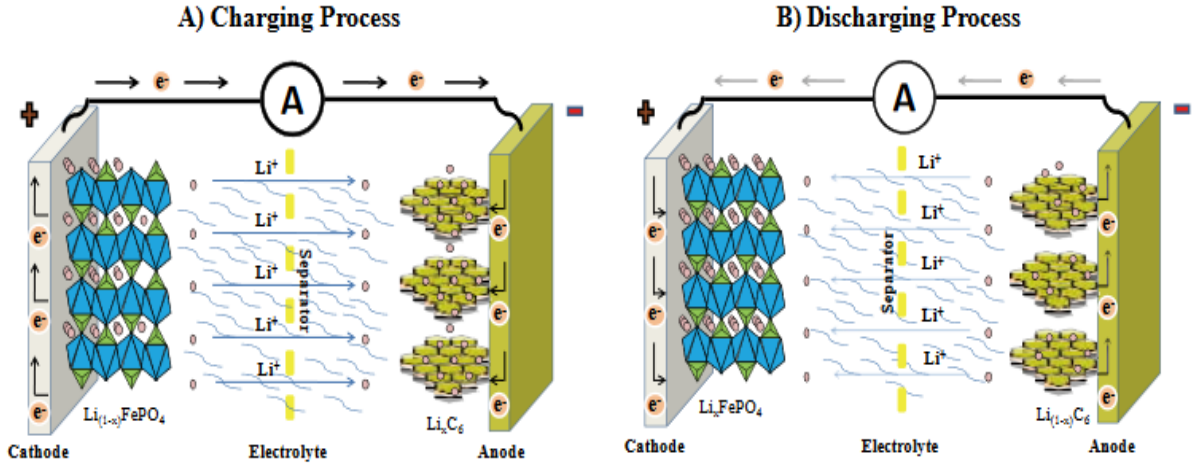

Figure 2. 1: Schematic representation of the configuration of rechargeable Li-ion batteries: (A) Charging and (B) discharging processes [57].

In the bid to achieve optimum performance, various active materials and electrodes thickness, design, and nature (porous or compact) have been considered including electrodes/electrolytes layers to enhance the electrochemical reaction through experimental procedures. Through experiments, factors affecting high-rate capacity are attributed to a decrease in active particle size [58], increase in solid-state diffusivity [58] electrode porosity [11], [12], optimized electrolyte concentration, and viscosity [11]. Several theoretical studies and models to confirm experimental results or suggestive additive factors have been reported [59], including also report of analytical model [15] to quantitatively put all the factors influencing battery performances to fitting expressions. Besides, molecular dynamics simulation study of long-range ion-ordering in salt-concentrated lithium-ion battery [60] has been performed using GROMACS 4.5.5 program [61]; where intermolecular interactions were described with Lennard-Jones and Coulombs; with the conclusion that in highly concentrated electrolyte solutions, long-range ion-ordering results to multiple lithium-ion complexes. It is, however, surprising that in these developments, little or no efforts are in the direction of including the long-range Coulomb effect to determining the charge storage capacity of batteries, even though Coulomb interaction is pertinent to describing electrochemical processes. While the inclusion of long-range Coulomb in the models for charge equilibration will help in mimicking realistic systems, the models can help delineate the charge evolution and interaction in batteries.

2.2 Electric Double Layer Devices

Charge carriers are the hallmarks of the development of electronic devices in the semiconductor device industry; in addition to improving conductivity, increased charge carrier accumulation can help achieve chemical reaction, superconductivity, magnetization or magnetic ordering, phase transition, and even lead to charge separation at the interface between to dissimilar surfaces. The charge separation births electric double layers (EDLs) at the solid-electrolyte interfaces with induced high electric fields. EDLs consist of pairs of opposite charges at the boundary regions of two different interfaces between an electrode and a liquid electrolyte (called ionic liquids). EDLs of ionic liquids (molten salts) are becoming relevant in electronics and optical technologies [62], [63] as EDL field-effect transistor (EDL-FET) [7, 64], for which the ionic liquids particularly take the function of a gate dielectric material. The EDLs attracted interest due to high density-carrier injection, low molecular weight, and high polarizability of the liquids. These properties make them more conductive than the traditional electrolytes [65] such as SiO_2 gate dielectrics. Electric double-layer capacitors (EDLCs) [66], in addition to being used as circuit elements, are energy storage devices that store energy owing to large charge accumulation in the EDL region. Recently, the EDLCs are having applications as batteries in response to the increasing demand for energy storage technologies and novel applications such as electrical and hybrid vehicles [67] and smart grid and smart city management. If the technology of EDLCs is well improved or developed, based on their power density in the order of 15 kW kg^{-1} has the conspicuous feature of ousting batteries with power density of 1 kW kg^{-1} order [68].

Electric Double Layer Formation at Interfaces. An interface may acquire an electric charge by one or a combination of the following methods [69]: (i) preferential (or differential) solution of surface ions, (ii) direct ionization of surface groups, (iii) substitution of surface ions, (iv) specific ion adsorption, and (v) charges deriving from specific crystal structures. These methods describe different situations depending on the materials [70] involved. Extensive research on the electrode-electrolyte interfaces enabled researchers to formulate various approximate models to describe the properties of electrified interfaces for the methods of acquiring charges. The Helmholtz [71] compact layer model assumes that EDLs are formed by the adsorption of a single ion layer in the electrolyte while equal counter charges lay parallel on the electrode interface of the boundary as shown in Figure 2.2(a) such that the arrangement is assumed a double plate parallel capacitor, in which the plates are separated by a dielectric of thickness d.

The Gouy-Chapman (GC) [72], [73] model considered the thermal motion of ions near a charged surface and accounted for the diffusion property of the ions. The latter resulted in an exponential decay of electric potential for a distance away from the interface towards the solution (Figure 2.2(b)). The Gouy-Chapman-Stern (GCS) [74] is a modification of the Gouy-Chapman model, which adopted into the GC model, the Helmholtz compact layer of ions, and considered that ions have finite size, and thus, the closest approach of the outer Helmholtz plane (OHP) to the electrode varies with ionic radius. Figure 2.2 (c) shows the inner Helmholtz plane (IHP) and outer Helmholtz plane (OHP). The IHP refers to the distance of the closest approach of specifically adsorbed ions and OHP refers to that of the non-specifically adsorbed ions [75] and corresponds to the plane where the diffuse layer begins. The double-layer distance described by the Helmholtz model is represented by d, whereas Φ_0 and Φ respectively present the potentials at the electrode surface and the electrode/electrolyte interface.

Though the GCS model (Figure 2.2(c)) could perfectly describe the arrangement of solvent and solute ions in any traditional electrolytic solution [74], it is not adequate for electrolytes (ionic liquids) that have intrinsic molten salts with ionic, solvent-free features at room temperature [65]. Considering such liquids, a multilayer model was developed with an approximation that the Boltzmann distribution of vacancies at the interface results in polarization based on deformation of ionic charges in the multilayer structure [76], [77]. Even though the multilayer model gives an acceptable description of electrode/electrolyte EDL and compares agreeably with experimental results, the models are far from reproducing accurately the features of a molten salt system [78].

Interaction between Electrode and Electrolyte. For solutions having dissolved ions (charge) and surfaces that may have different or similar charges, to apply Coulomb's law for the description of the interactions among ions, it is more realistic to consider the presence of all particles. Therefore, it is pertinent to apply Boltzmann's distribution law, which gives the probability of finding one particle with specific potential energy, ΔG (free energy) at a given point from a reference position. The probability can be specified in terms of average concentration c for a position r to a concentration c_0 for a reference position where ΔG or the potential is assumed to be zero, therefore, at a temperature T the distribution is [69]:

$$c = c_0 \exp\left(-\frac{\Delta \mathrm{G}}{kT}\right) \tag{2.1}$$

Given a distance from r from a region occupied by negative charge, there is an electric potential Φ at point r. The concentration c_+ and c_- of positive and negative ions associated to the potential are respectively given as:

$$c_+ = c_0\, exp\left(\frac{-Z^+ e\Phi}{kT}\right) \tag{2.2}$$

$$c_- = c_0\, exp\left(\frac{Z^- e\Phi}{kT}\right) \tag{2.3}$$

where Z^+ and Z^- are the valency of the ions and $Z = |Z^+| = |Z^-|$.

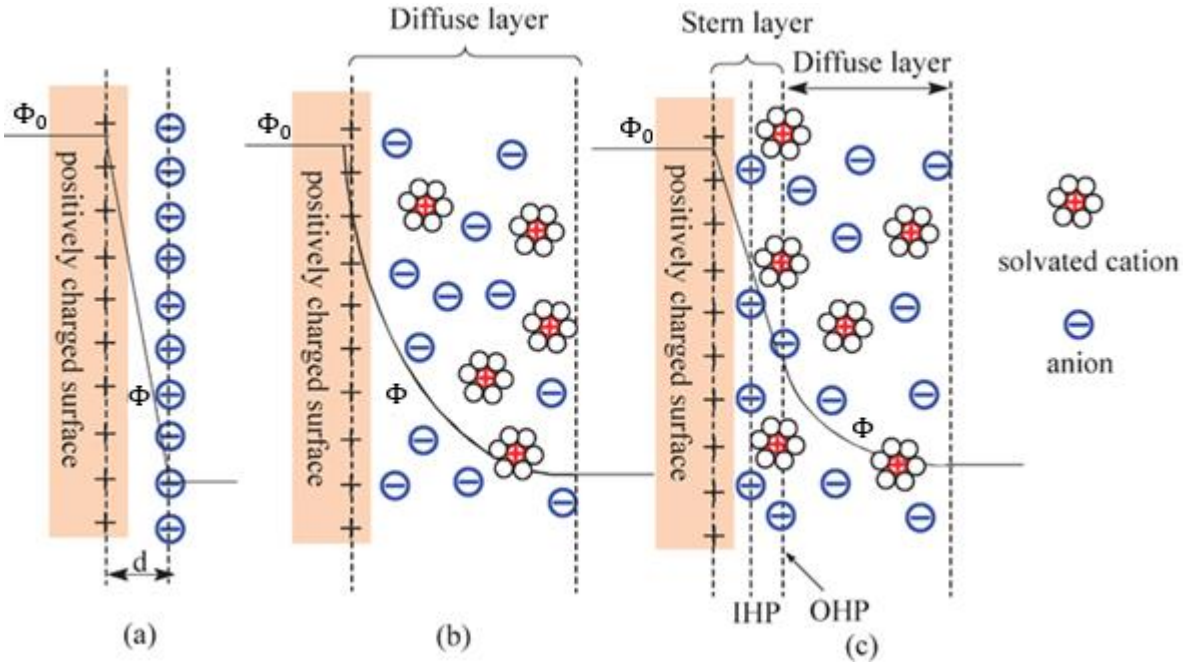

Figure 2. 2: Schematics of EDL models at a positively charged surface: (a) the Helmholtz model, (b) the Gouy-Chapman model, and (c) the Gouy-Chapman-Stern model [75].

By Coulomb's law, there will be excess positive ions than negative ions in the region, the excess is calculated as follows:

$$c_+ - c_- = c_0\left[exp\left(\frac{-Z^+ e\Phi}{kT}\right) - exp\left(\frac{Z^- e\Phi}{kT}\right)\right] \tag{2.4}$$

The region of excess charge associated with the potential is referred to as "ionic atmosphere" or "charge cloud," which is more commonly referred to as the "Electric Double Layer." Thus, it is worthwhile to concisely note that EDL is formed at the interface of charged solid electrode and electrolyte due to Coulomb interaction between surface charges and ions. The interaction results in an exponential decrease in the surface potential from the regions occupied by excess counter ions and deficient in co-ions. The region extends within Debye length. The formation

of EDL attracted attention in atomically 2D materials with great potentials for applications in super capacitors, nano-junction gate devices, bio- and molecular-sensors, energy harvester, and interestingly explains wettability [79] of 2D material surfaces exposed to the ionic liquid environment.

Regardless of the considerable progress recorded, some interesting physics and chemistry are still not well understood concerning EDL. A major problem challenging the EDL technology is optimization because of the complex electrode-electrolyte correlations that affect the energy and power densities. To confront this challenge, researchers have considered various device configurations, electrode designs, and natures [80] with some new postulates and approximations [81] that are built on the existing ones. Several experimental studies [82], [83] have also been done and models put forward to explain these phenomena in EDL capacitors. For instance, effects of specific ion adsorption in the electrode surface, the electro-kinetic and electron-ion transport in nano pores of different geometries and sizes [84]. In the study of microporous carbon electrodes for capacitive deionization, [81] postulates that an attractive chemical potential that is inversely proportional to ion concentration results from fluctuating Coulomb interactions (image forces) between individual ions and the metallic pore surfaces. The authors argued that the forces were not captured by the mean-field theories such as the Poisson-Boltzmann-Stern model or the Donnan model [85] for EDL description. The work, which highlights the importance of electrostatic image forces to porous electrodes produced remarkable results with the experiment. A substantial number of molecular simulations have also been carried out to shed light to various phenomena happening in EDLs; for example, the anomalous capacitive increase in EDLC has been explained to result from a superionic state, in which ions are densely packed [80]. The interfacial orientation ordering of water and its evolution at the application of potential difference was fully observed taking advantage of 3D resolution at equilibrium solvent density via a DFT-based molecular dynamics study [86]. However, while [86] concludes with the need for a functional form that depends on both the solvent density and the electrode charge for accurate description of equilibrium solvent density and equilibrium electrode charge distribution [79], growing the library of 2D materials and their application in liquid phase sensors, actuators, and surface modifiers, calls for the establishment of an understanding of their interfacial interaction with other material and liquids. On concluding a review of molecular modelling of EDL capacitor, [84] suggests that dynamic effects such as focusing on ionic transport and charge-discharge kinetics should be exploited to increase performance. Reactive force fields with QEq describe dynamic conditions

though they are subject to distance cut-off while treating Coulombs interaction, limiting their application to nanoscale devices. This work planned the inclusion of long-range Coulombs interaction in the charge equilibration model, which we hope will help the understanding of electrochemical processes in electric double layer devices especially the interaction of surface charge charges and the ions in the electrolyte.

2.3 Electrochemical Metallization (ECM) Cells

Resistive switching is a reversibility property of nonvolatile electronic elements that change their electrical resistive state between two stable levels upon the application and/or removal of an electrical stress [87]. This property is fascinating because the resistive states can be regarded as on/off or binary logic states of digital circuit elements, which can have tremendous applications in memory devices [88], information storage and computing [89], etc. A category of such elements is resistive random-access memory (ReRAM) [90]. ReRAM materials function based on switching between high-resistance states (HRS) or OFF state and low resistance state (LRS) or ON state. A change from the HRS to LRS is called SET operation and corresponds to the "write operation" of a memory device while the reverse behavior is termed RESET corresponding to "read operation" of a memory [87]. The resistance switching [3, 8] behavior of ReRAM has been widely studied for designing memory devices including electrochemical metallization (ECM) cell [16] or conductive bridging random access memory (CBRAM) sometimes called nanoscale resistance switch [7]. The operation of ECM cells depends on the formation across and dissolution away from the electrolyte towards an electrode of a conductive path (conductive filaments, CF) at biasing and reverse biasing the terminals with an electric potential difference, respectively. The chemical composition, diagrammatic working mechanism, and $I - V$ switching cycle of a typical ECM cell are captured in [3], [87].

Several simulation works have been done and techniques fashioned towards understanding in detail the functionality of the conductive bridging cells; some of these works include: (i) Atomistic origin of ultrafast resistance switching in nanoscale ECM cells [18] in which ultrafast switching ranging from hundreds of picoseconds to a few nanoseconds for Cu active electrode and amorphous silica dielectrics is observed, (ii) Atomistic simulation of electrochemical metallization cells: mechanisms of ultra-fast resistance switching in nanoscale devices [8] in which the effect of device geometry on switching dynamics of Cu active electrode and SiO_2 ECM was studied; the result shows among others that the overall geometry of the device structure leads to either shorter or longer nanoscale switching time (iii) Electrode Kinetics of

Cu–SiO_2–based resistive switching cells [16], in which the kinetic of switching process in Cu–SiO_2-based electrochemical metallization memory cells was studied with the findings that the switching rate depends exponentially on the switching voltage and does not depend on the thickness of the amorphous SiO_2, and (iv) Stability and migration of small copper cluster in amorphous dielectrics [91] was done via density functional theory (DFT) to study the thermodynamic stability and migration of copper ions and clusters in amorphous silicon oxide, the authors find that the formation of metallic clusters does not require overcoming a nucleation barrier giving insight into the stability of nanoscale metallic clusters.

Further reviews, suggestions, and perspectives on the electrical characteristics, physics, and chemistry and laudable applications of these memory devices are available in recent publications [22], [23]. Despite the advances in memory technology, there are still at the present limited understanding of (a) the mechanism of atomic rearrangements producing the transition from the ON state to the OFF state and vice versa, (b) the variability from the device by device operation including the number of cycles per device and variation on switching parameters (set and reset voltages, HRS and LRS currents), (c) how electrodes separations and surface nature would improve the understanding of the operation and properties of ECM cells; the structure and nature of the formed filaments, and (d) investigations on how to improve resistive switching figures of merit relating to endurance and retention [23] limit of ECM cells; though many experimental and theoretical studies only end with prove-of-concept [22]. IT would be interesting to investigate the dynamics and nature of filament formation and dissolution for electrodes separated at various nanometer scales and study the retention and endurance related issues such as density profile of the filament-formed ions, diffusion rate/time of ions to form the conductive bridge and study cell-to-cell and cycle-to-cycle variation of electrical properties of the device.

Chapter 3

Atomic and Molecular modelling

Atomic and molecular modelling and simulation are strong scientific techniques for theoretical and computational prediction of properties of materials, confirmation of experimentally observed properties, and discovery of novel materials. Computer simulation is applied to observe properties and behavior of materials beyond limits impossible for experiment, it does not completely simulate real systems because it models systems in which the number of particles is far less than the order of 10^{23}, simulation time is far less than practical observation time, different approximations are implemented for the interaction potentials, boundaries, etc. Its range of applications covers biological systems to engineering and material science. Guided by the type, purpose, and size of the system to describe, an appropriate computing method depicted in Figure 3.1 can be chosen. Figure 3.1 shows the levels of approximations at the various time- and length scales and the number of particles applied to the various modelling techniques while the green color gradient shows how dense and compact the system could be at each level of approximation.

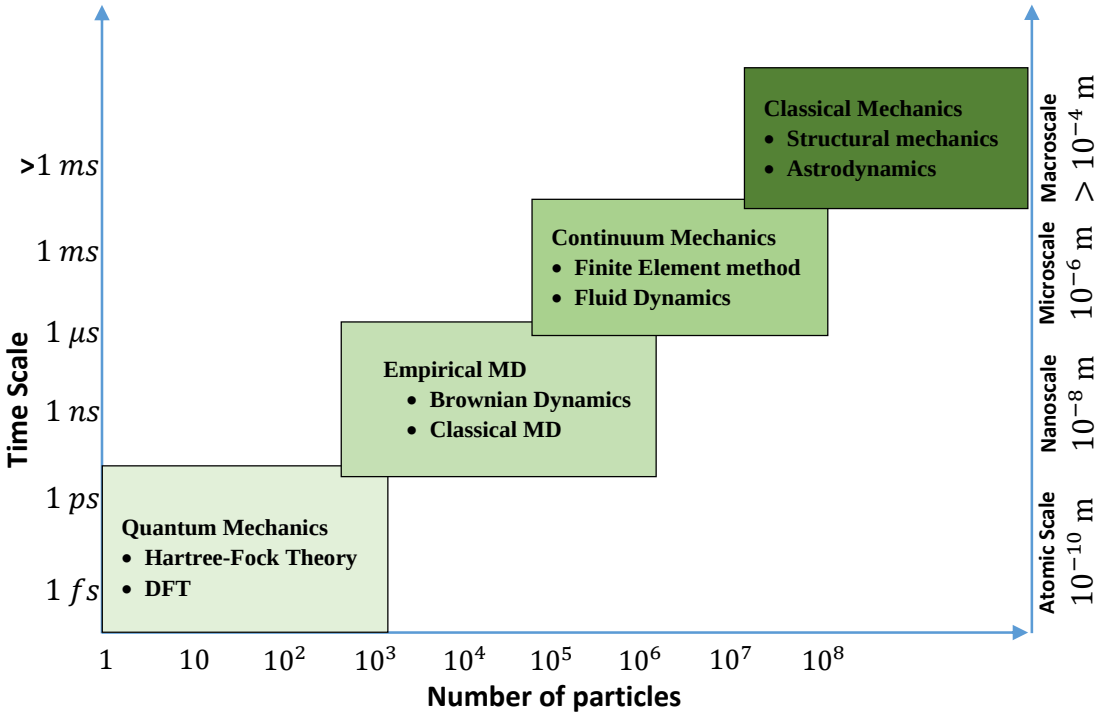

Figure 3. 1: Schematic representation in range of length- and time-scales accessible to a variety of modeling methods, from quantum mechanics for exactly accurate, expensive calculations through to approximate methods such as finite-element modeling.

3.1 Quantum Molecular Mechanics Simulation Approximation

The atomistic simulation starts with electronic-structure calculation of the properties of materials. This calculation relies on the first principal quantum mechanics description of materials, which is based on solving explicitly the electronic Schrödinger equation under a few approximations such as Born-Oppenheimer. Because very few approximations and no parameterizations are made, calculations are completed based on pure quantum mechanics (QM) and physical constants, the method is called the ab initio method. Ab initio calculations are approached either via Eigen-function-based or electron-density-based methods. The wave-function based approaches apply perturbation theory and variation principle in solving the Schrödinger equation for particles of a system with a wave-function that depends on 3N spatial orbital coordinates; where N is the number of electrons in the system; plus, one spin coordinate degrees of freedom and are thus, computationally intensive. These methods include, for example, the complete active space with second-order perturbation theory (CASPT2), the second-order Moller-Plesset perturbation theory (MP2), the coupled-cluster with single, double, and triple perturbative excitations (CCSD (T)).

Density Functional Theory (DFT) approach is a formalism that simplified the many-electron system by considering, instead of the Eigen-function, the electronic charge density as a fundamental variable and finds a direct relationship between the ground state density and the energy of the system [92], [93]. One fundamental goal of DFT is to solve the Schrödinger equation for many-body problems using the electron density as a dynamical variable [93] and reduce the 4N degrees to 3 spatial degrees of freedom thereby reducing the computational cost. This goal has not completely been achieved even with the development of orbital-free density functional theory (OFDFT) [94], [95], in which approximate functional is used for kinetic energy. A pivoting approximation re-introduced orbital dependence in the calculation of the energy. The approximation utilizes the Kohn-Sharm DFT (KS DFT) to reduce the many-body problem of interacting electrons in a non-varying external potential to problems of non-interacting electrons moving in an effective potential [96].

$$\left(-\frac{1}{2}\nabla^2 + \mathrm{v_{eff}}(\mathrm{r})\right)\varphi_\mathrm{i}(\mathrm{r}) = \varepsilon_\mathrm{i}\varphi_\mathrm{i}(\mathrm{r}) \tag{3.1}$$

The first term at the left-hand side of Eq. (3.1) is the kinetic energy and $\mathrm{v_{eff}}(\mathrm{r})$ is the effective potential, ε_i (in Hartree units) is the Kohn-Sham orbital energy corresponding to the Kohn-Sham orbital, $\varphi_\mathrm{i}(\mathrm{r})$. The density is given by:

$$\rho(r) = \sum_{i=1}^{N} |\varphi_i|^2 \tag{3.2}$$

And the total Kohn-Sham energy; in natural units (Hartree atomic unit) is expressed as:

$$E[\rho] = \sum_{i=1}^{N} \int dr\, \varphi_i^*(r) \left(-\frac{1}{2}\nabla^2\right) \varphi_i(r) + \int v_{ex}(r)\rho(r)dr + \frac{1}{2}\int \frac{\rho(r)\rho(r')}{|r-r'|} dr\, dr' + E_{xc}[\rho] \tag{3.3}$$

The effective potential energy consists of the external potential, Coulomb electron-electron interaction, and exchange-correlation energy terms, and the effective potential is given by Eq. (3.4). The last term of Eq. (3.3) is the exchange-correlation potential, which lacks explicit functional form [53].

$$v_{eff}(r) = v_{ex}(r) + \int \frac{\rho(r')}{|r-r'|} dr' + \frac{\delta E_{xc}[\rho]}{\delta\rho(r)} \tag{3.4}$$

Various approximations such as the local density approximation (LDA) and the general gradient approximation (GGA) have been employed to seek the functional form of the exchange-correlation energy [97]. DFT based packages such as Car-Parrinello molecular dynamics (CPMD), commercial (and academic) software package (CASTEP), and Vienna Ab-initio Simulation Package (VASP) are practical methods based on a plane-wave basis set to obtain accurate and reliable performance for large scale systems [49] with the utilization of the various approximation methods developed over the years.

The QM methods are found accurate, reliable, and applicable to all systems. However, in large systems such as biological molecules and liquids where the individuality of atoms is lost but collective effects esteemed to be important, it becomes irrelevant to discuss pure state but paramount to consider an ensemble of states. The ability to describe such a system by ab initio methods is intensive at a tremendous computational cost. This prohibitive cost limits the application of the ab initio methods to systems in the time scale of picoseconds (ps) and hundreds or a few thousands of atoms as shown in Figure 3.1. [98] uses tight-binding (TB) approach to calculate the graphene π and $\pi^\star$ bands and found that although TB could be orders of magnitude faster, less computationally expensive, and accommodate a greater number of atoms than DFT, it is at the expense of accuracy and transferability. Tight Binding (TB) approximation is a semi-empirical (few parameters from experimental or ab initio data are required to calculate energy and other desired properties of any given molecule of known geometry) technique that assume electrons to be tightly bounded to the atom, to which they belong and are limited to interact with surrounding atoms. TB approach [99] determines the

electronic structure of a system using an approximate set of wave functions obtained by a linear combination of atomic orbital (LCAO) of the free atom.

3.2 Classical Molecular Dynamics

Despite the completeness (connectivity, transferability, accuracy, ability to describe reactive and non-reactive systems) of the QM method and the advantages of TB, their computational expense as the system size grows (based on the information to examine or property of interest to extract), opens up the search for alternative methods that could allow modelling of real systems of a larger number of particles and times long enough to observe fully properties of interest at a qualitative accuracy and lesser computation cost. This is the gap classical molecular dynamic stands to fill. Molecular dynamics is an atomistic simulation technique for solving the problem of determining the dynamics or trajectory of a system in real-time. It does this by solving a second-order differential equation (Newton's equation).

3.2.1 Numerical Integration of Equation of Motion

Molecular modeling and simulation are scientific techniques for theoretical and computational prediction of materials, confirmation of experiment, observation of properties, and discovery of novel materials. Classical molecular dynamics does the above particularly by finding the trajectory of atoms at present, future, and even past time memory through solving Newton's equation of motion for the particles.

$$\boldsymbol{F}_i(\boldsymbol{r}_1, \boldsymbol{r}_2, \ldots, \boldsymbol{r}_N) = m_i \frac{d^2 \boldsymbol{r_i}}{dt^2} \tag{3.5}$$

A solution to this equation of motion exists through numerical techniques. But common to classical molecular simulation is the Verlet, velocity-Verlet, and leapfrog algorithms (or integrators) among others listed in [100]. These techniques involve discretizing time and solving the equations of motion at the sequence of time-step Δt. For instance, if a particle i is at a position $\boldsymbol{r_i}$ at time t, the position of the particle at a future time $t + \Delta t$ can be found by Taylor expanding $\boldsymbol{r_i}(t + \Delta t)$. A memory of the position at time $t - \Delta t$ is also obtainable by expanding $\boldsymbol{r}(t - \Delta t)$. From the two expansions of position at $t + \Delta t$ and $t - \Delta t$, the Verlet algorithm [101] is as written below:

$$\boldsymbol{r_i}(t + \Delta t) = -\boldsymbol{r_i}(t - \Delta t) + 2\boldsymbol{r_i}(t) + \boldsymbol{a}_i(t)(\Delta t)^2 + O((\Delta t)^4) \tag{3.6}$$

$$\boldsymbol{V_i}(t) = \frac{\boldsymbol{r_i}(t+\Delta t) - \boldsymbol{r_i}(t-\Delta t)}{2\Delta t} + O((\Delta t)^3) \tag{3.7}$$

The algorithm has an accuracy of fourth order of the time-step; $\boldsymbol{v}_i(t)$ and $\boldsymbol{a}_i(t) = F_i(t)/m_i$ are the velocities and the accelerations of the i^{th} particle at time t.

Solving Eq. (3.5) for the position, velocity or momentum and acceleration of the particles requires that the force be known. Unfortunately, the calculation of forces between interacting particles is the most time-consuming part of any MD simulation. For example, a system of N particles, the pairwise interaction scales to the order of N^2 arising from evaluating $\mathrm{N}(\mathrm{N}-1)/2$ pair distances. However, some techniques such as cell list and Verlet list [102] are available to scale the simulation time to N rather than N^2. An alternative method of obtaining the force on each i^{th} particle is by taking the negative derivative of the (empirical) potential energy function representing the interaction among atoms as a function of position r_i:

$$\boldsymbol{F}_i(\boldsymbol{r}_1, \boldsymbol{r}_2, \dots, \boldsymbol{r}_N) = -\boldsymbol{\nabla}_{r_i} V(\boldsymbol{r}_1, \boldsymbol{r}_2, \dots, \boldsymbol{r}_N) \tag{3.8}$$

For instance, if the shielded Coulomb potential (Eq. (3.9)) without taper function describes interaction, then, Eq. (3.10) specifies the force acting on the i^{th} particle in the system.

$$E(\{r_{ij}\}) = \frac{k_C q_i q_j}{\left[r_{ij}^3 + \gamma_{ij}^{-3}\right]^{1/3}} \tag{3.9}$$

where k_C represents the Coulomb constant, q_i and q_j are charges on particles i and j at a separation r_{ij} and γ_{ij} is a geometric mix of the hardness of the atoms; discussed in the subsequent section.

$$\boldsymbol{F}_i = \pm k_C q_i q_j \frac{r_{ij}}{\left[r_{ij}^3 + \gamma_{ij}^{-3}\right]^{4/3}} \boldsymbol{r}_{ij} \tag{3.10}$$

After initializing positions and velocities, we loop over time and compute the forces. We keep the positions and velocities updated at each time step while equilibrating the system or calculating any physical properties of interest. Figure 3.2 shows a minimalistic classical molecular dynamics process; the process continues if the simulation time has not elapsed. Also, very expedient at each MD time-step is the determination of partial atomic charges q_i that are found to minimize the total electrostatic energy, $E(\{\boldsymbol{r_i}(t)\}, \{q_i\})$ of the system. This minimization is subject to a charge-neutrality constraint $\sum_i q_i = 0$, and is equivalent to electrochemical (or electronegativity) equalization condition of Sanderson [103], which

demands that the chemical potentials $\partial E/\partial q_i$ be equal for all the atoms at chemical equilibrium. This condition results in a system of linear equations, which are solved for the charges. The charge on each atom is obtained and supplied to compute the interaction forces between atom pairs at each MD time-step.

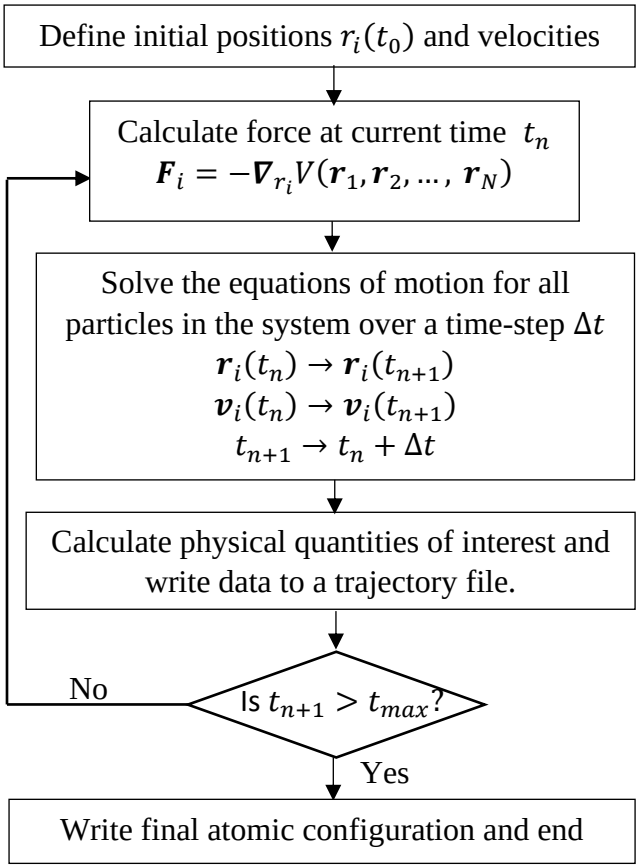

Figure 3. 2: Structure of a minimalistic MD process [116].

The MD integration of Newton's equation of motion applies the fundamental postulate of statistical averaging over time (the so-called ergodic hypothesis) to output results after visiting the various parts of the prescribed volume, energy, and number of particles in the case of a micro-canonical simulation.

3.2.2 Classical Force Field Models

Classical MD uses force fields to describe systems of interest. Force fields are expressions that represent the total potential energy function of a set of atoms to mimic the energy obtainable from an electronic structure calculation given the initial atomic positions and velocities. Force fields have different mathematical expressions. These expressions represent simple interaction potential energy functions (section 3.2.2.1) that can exist in any atomic

configuration or the interaction force between atoms in a system under description. [104] – [106] reveal that computer calculation of energy and detailed geometry of large molecules are possible. Such possibilities are achievable by first predicting in a series of iteration the properties of a selected series of well-known small molecules using interaction potential briefly discussed in section 3.3.1 and a training set of parameters, then, match the calculated properties with experimental or *ab initio* ones until the best representation (match) is obtained, then transfer the optimized (best) force field parameters to the large family of molecules. This approach is depicted in Figure 3.3, which shows the hierarchy of advancement on a method using the result from the predecessor method. This practice relies tremendously on many tunable experimental or *ab initio* data called the set of training parameters available for describing the atomic environment of a system. More information on energy minimization, parametrization, and optimization of force fields are recorded in [108].

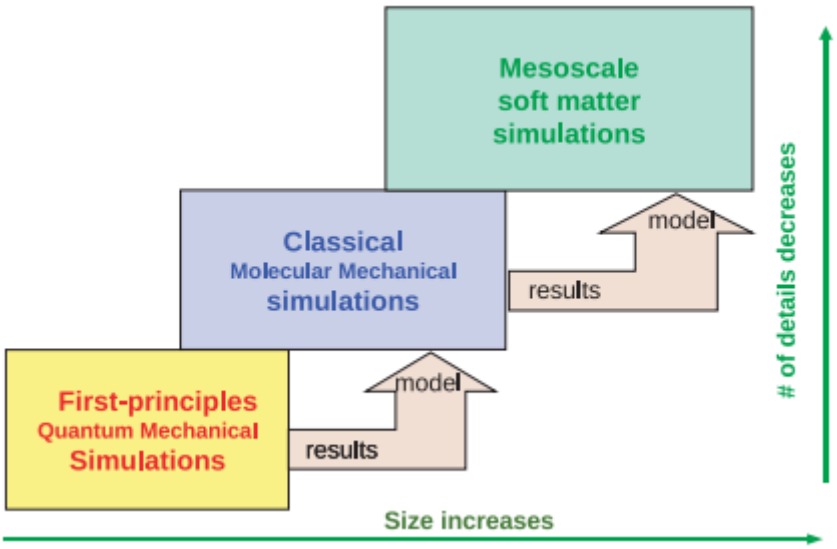

Figure 3. 3: Hierarchy of multiscale approach [107]: Results of simulations of a more detailed model are used to build a model for simulation on a larger scale. Within the process, the size of the system increases while the level of details decreases.

3.2.2.1 Basic Empirical Force Field (Atomic Interaction) Functions

Atomic and molecular interactions are responsible for the unique structural, dynamical, thermodynamic, magnetic, and electrical properties of polymeric [109], biological [110], solid-state (metals, ceramics, oxides) [111], and electrochemical device [112] systems. In the characterization of atomic interactions [113], often, pairwise configurations are considered; because it takes a pair of atoms or charges to bring about repulsion, attraction, neutrality or to form a bond and because any imbalance in charge distribution among atoms or molecules

allows them to interact with one another. Along the line of classifying atomic interactions, they are broadly categorized into bonded and non-bonded and divided into covalent, Van der Waals (vdW), and Coulomb. Covalent interaction represents chemical bonds in atomic systems and manifests in two body (e.g., dimers), three body (e.g., water), and four body (e.g., ethylene) interactions. vdW is a non-bonded but weak form of interaction existing in systems with dipole moments and Coulombs are non-bonded interaction between charged atoms. The interatomic potential is an expression that gives the total potential energy of a set of atoms that classically mimic the energy that would be obtained from an electronic structure calculation given the initial atomic positions. Some interaction potentials describe interaction in terms of bond length and angles, examples:

1) 2-body interaction (bond stretching): This interaction is mostly described with harmonic bond potential between a pair of atoms i and j vibrating like a spring under a harmonic vibrational motion. The potential is represented by [114], [115] as:

$$V_{bond}(r_{ij}) = \frac{1}{2} k_{ij} (r_{ij} - r_0)^2 \tag{3.11}$$

where r_0 is the reference equilibrium bond length, k_{ij} is the force constant describing bond stiffness/softness, $r_{ij} = \|r_i - r_j\|$ is the magnitude of the vector $\boldsymbol{r}_{ij}$ between atoms i and j.

2) 3-body interaction: This interaction has a bond angle ϕ at the central particle of three atoms i, j and k, on which the other extreme two atoms are bonded to. The interaction potential depends on the bond angle, ϕ between the vector positions from the central atom to the other particles. The harmonic angle potential is given by [114], [115] as:

$$V_{angle}(\phi_{ijk}) = \frac{1}{2} k_{ijk} (\phi_{ijk} - \phi_0)^2 \tag{3.12}$$

where k_{ijk} is the bonding constant and ϕ_0 is the equilibrium bond angle in radian and ranges from 0 to π. The three-body interaction potential is also described by cosine angle and harmonic cosine potentials stated respectively as:

$$V_{angle}(\phi_{ijk}) = k_{ijk}[1 - \cos(\phi_{ijk} - \phi_0)] \tag{3.13}$$

$$V_{angle}(\phi_{ijk}) = \frac{1}{2} k_{ijk}[\cos(\phi_{ijk}) - \cos(\phi_0)]^2 \tag{3.14}$$

The terms have their usual meaning, and these potentials behave like the harmonic angle potential given by Eq. (3.12), except that the cosine angle potential is periodic and smooth

for all angles, ϕ and the harmonic cosine potential has flatter bottom curvature than the harmonic angle and the cosine angle potentials.

3) 4-body interaction (torsion or dihedral angle) potential: This describes the dihedral angle interaction between the planes formed by the first three and the last three particles of a four consecutively bonded particles i, j, k and l. This situation occurs when there are three atoms i, j and k that are non-collinear but form a plane, if atom k is bonded to another atom l, then atoms j, k and l form a plane. The angle between these planes is the dihedral angle. The dihedral potential gives the energy of tensioning around the central bond. The central two atoms dominate the torsion about the bond, and the potential is given by [116]:

$$V_{torsion}(\phi_{ijkl}) = k_{ijkl}\left[1 - \cos\left(n_{ijkl}(\phi_{ijkl} - \phi_0)\right)\right] \tag{3.15}$$

where n is a non-negative multiplicity of the potential, it indicates the periodicity of the potential, k_{ijkl} represents the stiffness of the torsional potential around the central atoms, and ϕ_0 equals a phase shift torsional angle parameter. The dihedral potential has a form called improper potential. It is the potential that describes the interaction in a four atoms system, in which the one central atom is bonded to the other three atoms that are not bonded to one another. The improper dihedral potential is given by:

$$V_{improper}(\phi_{ijkl}) = k_{ijkl}(\phi_{ijkl} - \phi_0)^2 \tag{3.16}$$

Many other interaction potentials describe atomic interactions in terms of repulsive and attractive terms. The repulsive term is short-ranged while the attractive is a bit long-ranged when compared with the former [116]. A combination of the two gives the potential energy. Three of these potentials are given below and they can describe both the 2-body bond and the weak form of non-bonded interactions in molecular systems.

4) Lenard-Jones (6 -12) potential [117]: The potential is used to describe weak interaction between neutral atomic and molecular systems. It expresses the repulsion between atoms with r_{ij}^{-12} and the attraction with negative r_{ij}^{-6} as given below:

$$V_{LJ}(r_{ij}) = 4\varepsilon\left[\left(\frac{\sigma}{r_{ij}}\right)^{12} - \left(\frac{\sigma}{r_{ij}}\right)^{6}\right] \tag{3.17}$$

where ε is the depth of the potential well or the minimum of the potential between atoms, σ is the distance for which the energy is zero, and r_{ij} is the distance between molecules or

atoms i and j. The LJ potential is a two-body short-range interaction that describes the interaction of mostly neighbouring particles. In application, the potential is truncated at some cut-off distance r_c

5) Morse potential [117]: This potential is used to approximate the vibrational motion between a pair of atoms that are chemically bonded together. The repulsive and the attractive parts of the interaction are represented by exponential terms. The potential can be expressed as:

$$V_{Morse}(r_{ij}) = \varepsilon\left[\exp\left(\gamma\left(1-\frac{r_{ij}}{r_0}\right)\right) - 2\exp\left(\frac{\gamma}{2}\left(1-\frac{r_{ij}}{r_0}\right)\right)\right] \tag{3.16}$$

where $\gamma = 2\alpha r_0$ and $\alpha = \sqrt{\frac{k}{2\varepsilon}}$ are as defined in [42]. The potential is like LJ's and can be used for bond and weak electrostatic interaction. Here, k represents the force constant, r_{ij} is the distance between a pair of bonded atoms, r_0 is the equilibrium bond distance, ε is the depth of the potential well, and γ or α specifies the dispersion (width) of the potential well.

6) Coulomb Potential: This describes electrostatic interaction between charged atomic or molecular bodies. The direct Coulomb potential in its simplest and purest form is given as:

$$V_{Coul} = k_C \sum_{i<j} \frac{q_i q_j}{r_{ij}} \tag{3.17}$$

The potential is naturally known to be long-range interaction and can be represented in some other forms as captured under *orbital interaction* in this work. Where k_C represent a physical constant, r_{ij} is the separation between particles i and j having charges q_i and q_j respective, i is less than j is to avoid self-interaction counting.

3.2.2.2 Non-Reactive Force Field Models

Conventional empirical pair potential models consist of combinations of a few interactions potential functions depending on the interactions of interest to be described. An example is the embedded atom model (EAM) [118] developed for many-body MD simulation of metals; it allows the description of physics of vacancies, elastic constants, etc. and is expressed as:

$$V(r_{ij}) = \sum_i F_i(\rho_{h,i}) + \sum_{i<j} \phi_{ij}(r_{ij}) \tag{3.18}$$

In this potential function, $\rho_{h,i}$ represent the host electron density at atom i due to every other atom in the system, $F_i(\rho_{h,i})$ is the energy gained by embedding atom i into the electron density

that is contributed by surrounding atoms, and $\phi_{ij}(r_{ij})$ represents the pair potential between atoms i and j separated by the distance r_{ij}. Another example is the Stillinger-Weber potential [119] that contains 2-body and 3-body interaction terms. The potential is most importantly used for the description of covalent interaction in semiconductor materials. The Stillinger-Weber potential is expressed as,

$$V(r_{ij}) = \sum_{i<j} V_2(r_{ij}) + \sum_{i<j<k} V_3(\boldsymbol{r}_i, \boldsymbol{r}_j, \boldsymbol{r}_k) \tag{3.19}$$

Then, the DREIDING potential [115] that have been found useful for the dynamics of molecular systems. The potential can be expressed as:

$$V(r_{ij}) = \sum_{i,j} V_{bond}(r_{ij}) + \sum_{i,j,k} V_{angle}(\theta_{ijk}) + \sum_{i,j,k,l} V_{tors}(\theta_{ijkl}) + \sum_{i<j} V_{vdw}(r_{ij}) + \sum_{i<j} V_{Coul}(r_{ij}) \tag{3.20}$$

These terms take their forms and definition from section 3.2.2.1, the first three summation terms are covalent, V_{vdw} represents the van der Waal interaction expressed by Lenard-Jones potential and the last is Coulomb potential. Here, exclusions are made so that atoms that are bonded should not be described as non-bonded interactions (van der Waals and Coulomb).

Despite a great deal of progress [115] recorded in using the many-body potential to predict the structure and dynamics of large-scale molecular systems, these potentials are limited by the number of factors [120], for example, they assume static bonds all through the simulation process. The implications of this limitation are: (i) they cannot be used to model reactive systems where bond reformation is tenable, (ii) they cannot simulate the change of connectivity or coordination or the environment since they model fixed bond, fixed angles between atoms, which are specified before the simulation starts, and (iii) it will be difficult to do the simulation that involves different classes of materials, e.g., interface between a soft material with a metal or ceramic material with a metal. In view to surmount these limitations, reactive force fields were first proposed by [28].

3.2.2.3 Reactive Force Field Models

Generically, reactive force fields are dependent on the concept of partial bond order, bond energy relationship [97], [103], [121] – [123]. The force field of interest in this thesis is the reactive force field models with a focus on ReaxFF [28], [120]. ReaxFF is a bond-order-dependent classical interaction potential, for which the total energy (Eq. 3.21) is defined as the sum of partial energy contributions from terms that represent bonded (covalent) and non-

bonded (Van der Waals and Coulombs) interactions. Unlike other reactive force field models, ReaxFF allows the molecular dynamics simulation of processes that involve bond breaking and formation and does not necessarily allow fixed atomic connectivity to be predetermined before starting a simulation. Very importantly, it integrates dynamical charge calculation scheme to calculate atomic partial charges while structural information of the system is updated at every MD time-step. Among the methods for treating polarization [124] in molecular systems and fluctuating charges are the Split Charge Equilibration (SQE) [38], which depends on the charge transfer between bonded atoms, and the atom-condensed Kohn-Sham density functional theory approximation of second order (ACKS2) [125], which is an extension of SQE. However, in the development and application of ReaxFF, dynamical partial charge calculation is attainable by coupling it with the charge equilibration (QEq) technique developed by Rappë and Goddard [29]. In brevity, ReaxFF allows chemical reaction and interaction based on element, environment, and geometry. Interestingly, this model makes it possible to simulate devices that are composed of dissimilar materials. In other words, it allows the description of interface reactions. Thus, it has some advantage of bridging the gap between quantum mechanics techniques and classical molecular mechanics techniques. A specific example is the application of ReaxFF to describe interaction in glass-water [126] system.

$$V_{system} = V_{bond} + V_{over} + V_{under} + V_{lone\,pair} + V_{val} + V_{pen} + V_{conj} + V_{tor} + V_{vdW} + V_{Coul} \quad (3.21)$$

These energy terms are defined in [28], [120]. The covalent contributions have partial energy inclusions not accounted for in previous reactive force field models including bond-order terms that determine the chemical environment of atoms and control the bond strength of materials. The bond parameters are bond-distance dependent and change as the local environment surrounding atoms are continually updated at each MD step. Also, the bond parameters are smoothened out to zero at increased separation between atoms. The non-bond interactions are distance-corrected using a potential function called shielding interaction function [127]. For the Coulomb interactions, shielding becomes expedient at short separations between two atoms; at these distances, orbitals of the two atoms overlap and interactions are strong that the energy becomes unphysically high and blows up to infinity at zero separation.

3.3 Some other Forms of Coulomb Interaction Function

3.3.1 Coulomb Orbital Interaction

The direct application of Eq. (3.17) in the description of Coulomb interaction between a pair of atoms has been found problematic [29]; especially when dealing with non-bonded interactions, in which atomic separations can scale up to or become smaller than the vdW diameter of a given atom pair. The Coulomb interaction kernel ($1/r_{ij}$) between a unit charge on an atom at center i and another at centre j is emphatically accurate only at large separations between the atoms but results in a strong interaction at a short separation and becomes unphysically bounded at zero separation. Close distance or short separation is defined as the Van der Waals (vdW) diameter of the atoms involved. This catastrophic repulsion at zero separation between charged atomic particles is inaccurate. Evaluation of the Coulomb interaction potential from accurate Hartree-Fock (HF) [127] or local-density calculations in quantum mechanics and density functional theory (DFT) [92] should give a finite energy. The interpretation is analogous to an example recorded with a helium [129] atom where two electrons sharing the same atomic centre have finite repulsive energy. The Coulomb potential was evaluated from the two-centre Coulomb integral [130]; where the atomic orbitals or electronic wave-functions $\phi(r_i)$ and $\phi(r_j)$ of particles (electrons) i and j respectively, and their conjugates ($\star$) replaced the electronic charge densities.

$$J_{ij} = \int\int \phi_i^{\star}(r_i)\phi_i(r_i)\frac{1}{r_{ij}}\phi_j^{\star}(r_j)\phi_j(r_j)dr_i dr_j = \int dr_i \int dr_j |\phi_i(r_i)|^2 \frac{1}{r_{ij}}|\phi_j(r_j)|^2 \quad (3.22)$$

The Coulomb orbital interaction expressed in terms of two-center Coulomb integral permits a finite value, J_{ii}^0 as r_{ij} tends to zero and contributes significantly to bonded atoms. Such permit implies that Coulomb interaction does not strictly represent a pure $1/r_{ij}$ Coulomb potential but a shielded Coulomb potential with a finite value J_{ii}^0 at $r_{ij} = 0$. This states that at very close separation, two electrons are permitted to seat on the same atomic orbital with high but finite energy value in relation to J_{ii} and J_{jj} provided the Pauli exclusion principle (PEP) is obeyed. An illustrative application of the shielding correction (for overlapping of orbitals) is described by Rappë and Goddard [29]. They recognized the limitation in using the direct Coulomb interaction potential while establishing the charge equilibration (QEq) method. Valence atomic orbitals ϕ, and charge density distribution $\phi\phi^{\star} = |\phi|^2$ were utilized in handling situations of

orbital overlap. In this correction, they found the two-center Coulomb integral (Eq. (3.22)) applicable and proposed a normalized single Slater-type orbital function for the atomic density.

$$\phi_i = N_i r_i^{n_i-1} e^{-\zeta_i r_i} \tag{3.23}$$

where r_i, ζ_i, n_i and N_i are the distance between an electron and its parent nucleus, the slater orbital exponent (coefficient), the principal quantum number (valence state), and the normalization constant in relation to atom i. The orbital exponent determines the spatial charge diffusion and/or spread and it is related to the average size of the molecule, which is calculated as the average covalent radius R_i (in atomic units) of an atom in a molecule.

3.3.2 Empirical Coulomb Interaction Function in ReaxFF and QEq Models

The evaluation of Eq. (3.22) even for the simplest molecule with two nuclei and an electron is always a challenging task, see [131]. So, over the years, scientists have engaged in the development of an empirical approximation that will retain the behavior of Eq. (3.22) for $r_{ij} \rightarrow \infty$ and $r_{ij} = 0$ at less the computer time needed to compute all pair interactions in a system. Consequently, there are dozens of empirical Coulomb interaction functions called orbital overlap or shielding correction (function) in literature [127], [132]. The shielding functions are parameterized to exhibit the same descriptions and behavior. However, some perform better than others in conformity of their plots with the plot of the solution to Eq. (3.22) evaluated using Slater-type orbitals, see refs. [127], [132]. With the striking similarity (Figure 3.4, also shown in [132]) between the solutions from Slater-type integral function and the empirical shielding function proposed by Louwen and Vogt [132], Eq. (3.24) was adopted for non-bonded Coulomb electrostatic interactions in ReaxFF and QEq implementations in LAMMPS for molecular dynamics simulation.

The right-hand side of Eq. (3.24) may be multiplied by a seventh-order Taper function [28] to avoid a discontinuity at the cut-off point; depending on if the Coulomb interaction is treated with short-distance cut-off. The shielded Coulomb function is simple and easier to implement. Assuming unit charges for atoms i and j, then shielded Coulomb interaction potential at a non-bonded cut-off is:

$$J_{ij} = k_C \,.\, Tap(r_{ij}) \,.\, \frac{1}{\left[r_{ij}^3 + \gamma_{ij}^{-3}\right]^{1/3}} \tag{3.24}$$

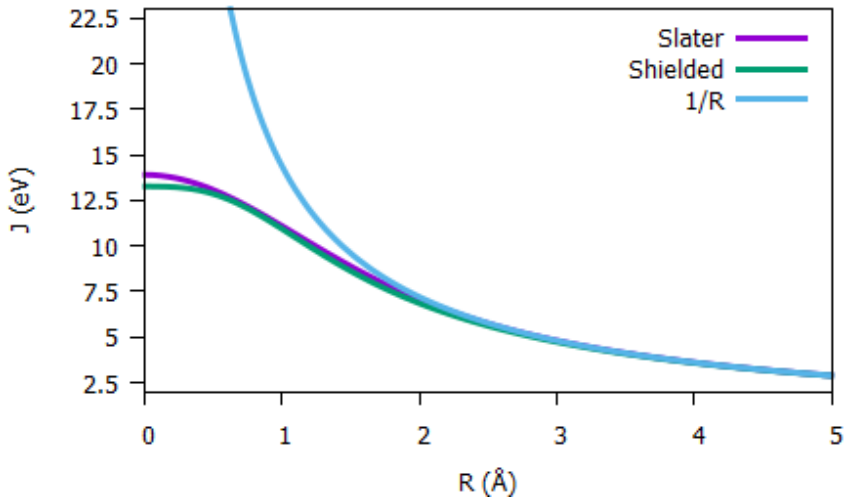

Figure 3. 4: A comparison of Coulomb interaction that consider orbital interactions between a C and an O atom as a function of interatomic distance against $1/\mathrm{R}$ of the Coulomb interaction with no orbital interactions.

These authors specify the separation between a pair of an atom to return $1/\gamma_{ij}$ at $r_{ij} = 0$. Where γ_{ij} is the geometric mix of the atomic hardness J_{ii}^0 and J_{jj}^0 of two atoms centered at i and j respectively; and is analogous to Lorentz-Berthelot mixing rules as $\gamma_{ij} = \left(J_{ii}^0 J_{jj}^0\right)^{1/2}$. The shielding correction removes the catastrophically infinite repulsion as $r_{ij} \to 0$ and permits two electrons to seat on or share the same atomic orbital with finite energy in relation to J_{ii} and J_{jj}.

3.3.3 Ewald Summation of the Coulomb Interaction Potential

In molecular dynamics simulation of bulk or large systems, which requires the boundaries surrounding the simulation cell to be specified, particles either interact at short- or long-range order. For short-range, particles interact only with neighbors up to certain cut-off distances r_c imposed through a straightforward spherical truncation of the interaction potential. Beyond r_c, interactions between particles are considered to have negligible effect, and are then, smoothened off at cut-off with some Taper function to avoid discontinuity as illustrated with the dashed yellow curve in Figure 3.5. In place of a Taper function, a long-range tail correction approximation is sometimes introduced to mimic the actual potential leading to

$$V_{total}(r_{ij}) = \sum_{i<j}^{N} V_{cut}\left(r_{ij}|_{r_{ij} \le r_c}\right) + V_{lrc}\left(r_{ij}|_{r_{ij} > r_c}\right) \tag{3.25}$$

The first term at the right-hand side represents the potential up to the cut-off distance. An alternative method contained in [120] for handling such correction is by cubical truncation,

also known as minimum image convention (MIC). For example, if a periodic boundary condition, in which $r_c \leq l/2$ is considered; l being the length of the simulation box, particle i interacts with only the nearest periodic images of other particles j in the system of N particles, then, the long-range correction potential V_{lrc} is defined by Eq. (3.26) with the assumption that the radial distribution function $g(r) = 1$ for $r_{ij} > r_c$. $V(r_{ij})$ equals the interaction potential, which could be a Lennard-Jones, Morse, or Buckingham and ρ is the average number density.

$$V_{lrc}\left(r_{ij}\big|_{r_{ij}>r_c}\right) = \frac{N\rho}{2}\int_{r_c}^{\infty} 4\pi r^2 V(r_{ij})dr \tag{3.26}$$

The correction is valid for the cases, in which the tail correction potential decays rapidly [120] than r^{-3} in 3 dimensions. The condition that the potential must decay rapidly than r^{-3} makes the use of truncated potential plus tail correction inadequate for Coulomb interactions, which is inherently and naturally a long-range interaction. This is because even with the tail corrections, the potential fails to converge instead, it diverges as the system size increases when more cells or bigger concentric shells are considered. In such situations, the interaction of a particle with all periodic images [133] including one's own images are required for adequate description of the interaction. This becomes the case for a slowly varying potential such as Coulomb. Long-range interaction is then defined as one, in which the interaction between particles decays slower than r^{-d}, where d is less than or equal the dimensionality of the system. For Coulomb interaction between a pair of charged bodies, the potential is proportional to r^{-1}. Figure 3.5 illustrates typical r^{-1} of Coulomb (blue curve), r^{-6} of the repulsive part of Lennard-Jones (LJ) (green curve) and the full LJ potentials containing bonding interaction (purple curve). The plot shows that $1/r$ decays very slowly with increased separation; an indication that truncating the interaction potential between atoms that are further apart does not adequately describe long-range Coulomb electrostatics. The interaction energy, though decays, $1/r$ does not die off as quickly as volume grows. Beyond the cut-off (see [102]), as more shells or atoms are considered the volume grows with $4\pi r^2$ (area of sphere) such that $\int_{r_c}^{\infty} (1/r)\, 4\pi r^2 dr = \infty$.

Inclusion of more than nearest neighbors is always handled by some special techniques developed over the years, here, Ewald method is considered. The Ewald technique allows part of the sums to be done in real space while the remaining part is done in reciprocal space. While elaborate discussions of the Ewald technique including its derivations and periodic boundary conditions (PBC) can be found in refs. [102], [133] – [136], an application of the technique, in which expression for pressure tensor [64] at bulk and surface geometry of systems interacting

electrostatically is developed using Ewald method. The application of the Ewald summation technique to the Coulomb electrostatic interaction potential yields the total potential energy in the form of "Ewald-modified-Coulomb potential energy" given in [102], [133] as:

$$V_{Coul} = \frac{1}{2V}\sum_{k\neq 0}^{N}\frac{4\pi}{k^2}|\rho(h)|^2 \exp\left(-\frac{k^2}{4\zeta^2}\right) - \left(\frac{\zeta}{\sqrt{\pi}}\right)\sum_{i=1}^{N} q_i^2 + \frac{1}{2}\sum_{i\neq j}^{N}\frac{q_i q_j erfc(\zeta\, \boldsymbol{r_{ij}})}{\boldsymbol{r_{ij}}} \quad (3.27)$$

$$\rho(k) = \sum_{i=1}^{N} q_i \exp(i\boldsymbol{k}\,.\boldsymbol{r_i}) \quad (3.28)$$

The last term at the right-hand side of Eq. (3.27) is the real space contribution to the potential energy function. Zeta (ζ) is an arbitrary constant called Ewald [137] splitting term. The second term is a spurious self-interaction term and is independent of particle's positions. The first term is the Fourier space contribution to the electrostatic energy while $\rho(k)$ is the charge density in reciprocal space. V, r and k are the volume of the unit cell considered, the real- and reciprocal -space vectors, respectively.

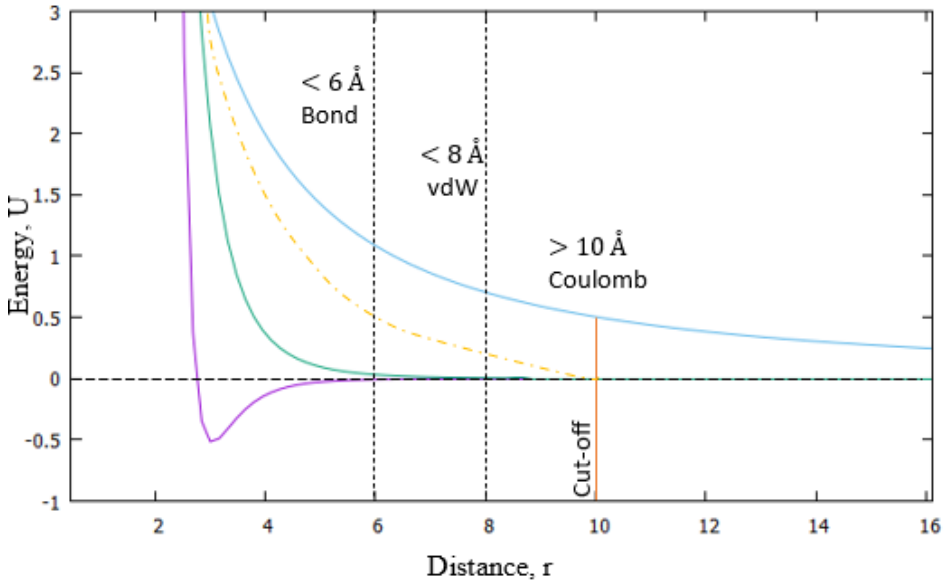

Figure 3. 5; Illustrative comparison of the r^{-6} of Lenard-Jones (green) interaction against r^{-1} of Coulomb (blue) potentials with impact of cut-off distance (yellow); purple depicts bond distance interaction.

Chapter 4

Model Development

4.1 Force Models

4.1.1 Short- and Long-range Coulomb Forces

The electrostatic interactions (Coulomb energy and forces) between charged particles are described by established theories taught even in college physics. Despite the simplicity of the interaction law, its application and numerical implementation in molecular dynamics simulations are at a computational cost of $\mathcal{O}(N^2)$ (N equals the number of atoms) arising from the number of pairwise interactions to be computed. These interactions grow as the system size grows and require simulation time proportional to N^2 or l^6 (l being the box length) in 3D [133]. Different approximations and/or methods have been used to compute Coulomb interaction forces from the potential energy function in MD simulation of bulk and large systems; to reduce the cost and enhance speed and/or accuracy. In MD treatment of bulk or large systems, which requires boundary conditions to be specified, particles interact either at short- or long-range distances. Short-distance computation treats the Coulomb interaction as short-ranged non-bonded potential. This only allows particles to interact with only neighbors up to a certain truncation imposed via a short-distance cut-off radius r_c. The cut-off sets the pair potential to zero for pair separations greater than the cut-off distance. In some approximations, a tapper function is used to smoothen the potential at the cut-off point to avoid a discontinuous jump. Alternatively, a long-range tail correction is introduced to account for the neglected interactions. A neighbor list for each particle is efficiently generated and managed within the cut-off through a Verlet list algorithm [101] or linked cell list method [133,138]. On the contrary, long-range computation recognizes the slowly varying nature of the Coulomb potential function where atomic interactions decay slower than r^{-d}, d equals the dimensionality of the system, and r is the separation between two particles. Inclusion of further neighbors is always handled through some special techniques developed over the years. In particular, the Ewald technique allows part of the sum, truncated at a certain cut-off, to be done in real space while the other remaining part is done in reciprocal space. Alternative methods such as particle-particle particle-mesh (P3M) [138] and fast multipole method (FMM) [139] could be employed depending on the desired accuracy. Numerous documents [102], [133] –

[136] have elaborate and detailed discussions of the Ewald summation method for long-range interaction of electrostatic systems using periodic boundary conditions. The periodic boundary treatment of Coulomb interactions via Ewald summation is a conditionally convergent series, which means it depends on the order in which the summation is done.

Arguably, molecules, specifically, dimers having $\pm 1e$ formal or valence charges or small atomic systems are the best and simplest examples to study these interaction forces. For this reason, comparisons of the short-range and long-range (Ewald) Coulomb forces against the results attainable analytically through the basic Coulomb formula are presented using a linear triatomic molecule, e.g., $MgCl_2$ unless otherwise stated. The atomic configuration is linearly placed along a fixed z direction at the center of a large simulation box with sides of about 100Å, which is periodic in x and y directions. We compute the Coulomb force analytically along the z direction using the basic Coulomb formula. The analytical result is compared with the z-component of the short- and long-range Coulomb forces obtained in the simulations. With the size of the simulation box, large distance cut-off can be specified while the problem of minimum image convention (which may arise from the cut-off value being greater than one-half of the size of the box) is avoided. The 3-atom system is useful in understanding the effect of including long-range effects to electrostatic Coulomb between two atoms in the presence of a third atom. This effect is observed by monitoring the variation of the forces with increasing cut-off distances as the separation between Mg and Cl atoms increases or reduces at the speed of 1.0 Å/fs. Therefore, single-point calculations were performed with Coulomb pair potentials (force fields) in LAMMPS. One calculation uses the "coul/cut" interaction potential file, which describes "direct" short-range Coulomb interaction at a given cut-off distance and the other "coul/long" with Ewald style describes long-range Coulomb interaction. In every calculation, the atoms on the two sides were maintained at $-1e$ charge value, while the middle atom was charged $+2e$. Otherwise, the charges were determined by QEq technique.

The forces on one of the sides and the middle atoms are reported in Figure 4.1. The analytical result is reproduced via Ewald, whereas increasing the short-distance cut-off yields results approaching the analytically computed forces. Figures 4c and d show the results for cluster investigations (more atoms of $MgCl_2$), which returned results that are consistent with the 3-atom system. The only difference is the magnitude of the force (which is extremely high compared with the 3-atom calculations) acting on the focused particles, which have more neighbors than the atoms in the 3-atom case. Suggestively, short-distance approximation

should be adequate for systems with few atoms. The atomic spread or positions in the systems are within the cut-off distance, are not a few Angstroms above the cut-off, or are a hundred of the cut-offs far away so that the long-range effect would attenuate. Otherwise, energy contributions to an atom from other parts of the system are neglected. This may lead to the

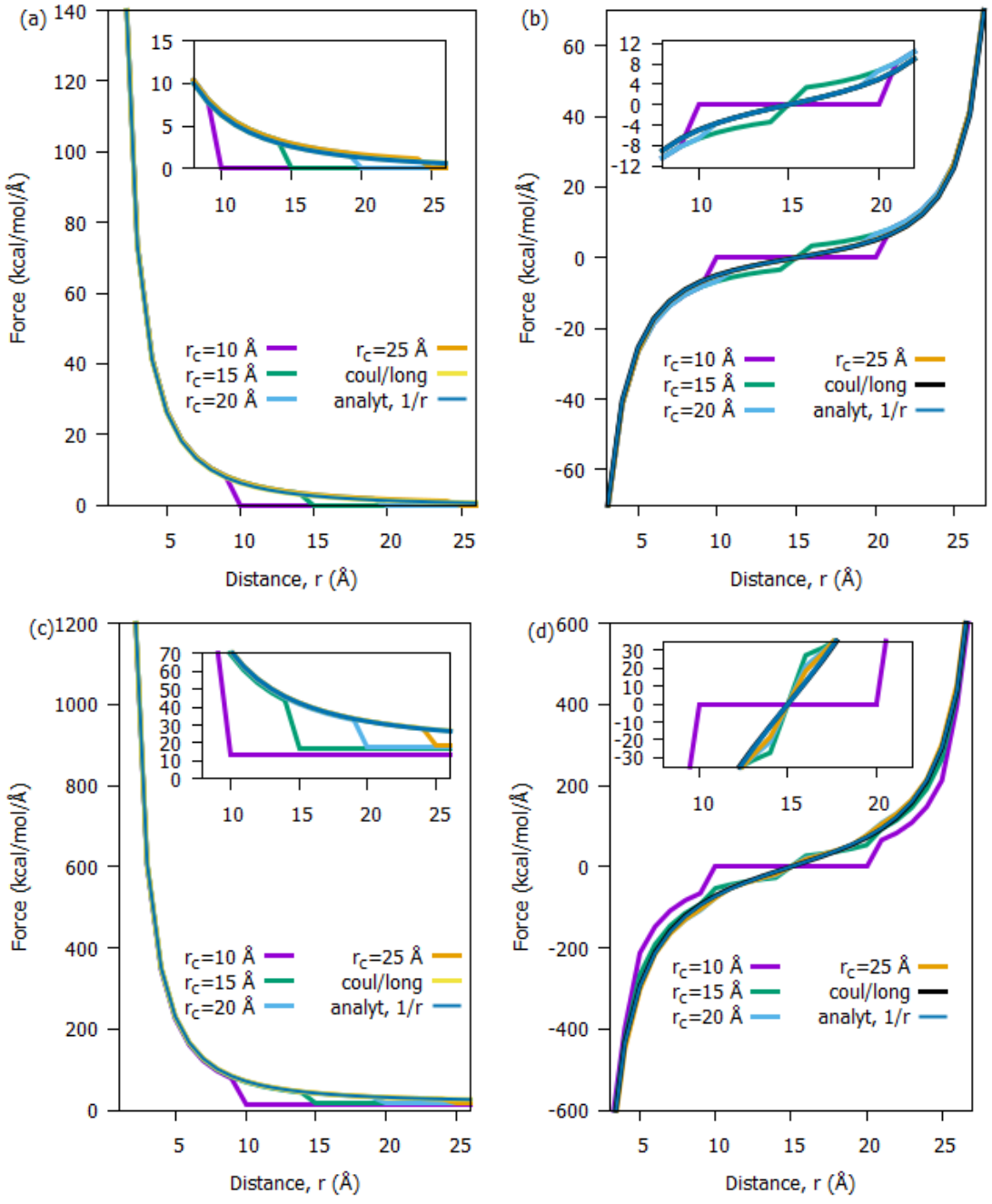

Figure 4. 1: Analytical results, Short-, and long-distances Coulomb forces on Cl (left column) and Mg (right column) atoms. Upper and Lower rows are for simple triatomic and crystalline cluster of $MgCl_2$ systems, respectively. The in-set plots zoom into the dense areas around the cut-off points. Analytical results are based on Ewald sum while the short-distance Coulomb results approach that from Ewald (analytical result) as the cut-off distance is increased.

system possessing entirely wrong energy and structure due to imbalance in ions and counter-ions [140]. Figure 4.1 shows the high magnitude of the computed forces for close separations between atoms. These forces tend to be infinite if the separations between atoms tend to be zero. This indicates that neither coul/cut nor coul/long force fields describe Coulomb interaction with shielded function. These results are contrary to the result obtainable by solving two-center Coulomb integral with normalized Slater-type orbitals in Figure 3.4.

4.1.2 Shielded Long-range Coulomb for MD Simulation

The interesting idea about the Ewald technique is the decomposition of the slowly decaying Coulomb potential function into a short-range component, which is rapidly convergent (rapidly goes to zero at large distances) in real space and a long-range component, which decays quickly in reciprocal space [102], [133]. Assuming unit point charges, the kernel of the Coulomb interaction potential is decomposed as given by Eq. (4.1). The second term at the right side of Eq. (4.1) is a smoothly varying long-range function conveniently solvable in Fourier space. The function f must result in two fast decaying parts. In real space, f is often chosen to be the error function $\mathrm{erf}\,(x)$. However, in the reciprocal space, it is commonly retained as the Gaussian distribution function because it is smooth, periodic, and representable by a rapidly convergent Fourier series.

$$J_{ij}(r_{ij}) = k_C \frac{1}{r_{ij}} = k_C \frac{1 - f(\zeta r_{ij})}{r_{ij}} + k_C \frac{f(\zeta r_{ij})}{r_{ij}} \tag{4.1}$$

The parameter $\zeta > 0$ is the Ewald splitting parameter. It determines the spread or width of the decomposition. We focus on real-space short-range component, i.e., the first term at the right side of Eq. (4.1), which is a complementary error function $\mathrm{erfc}(x) = 1 - \mathrm{erf}\,(x)$. Then, the total real-space contribution to the Ewald-modified Coulomb potential energy of a N particles system and L periodic boxes is written as

$$V_{sre}(r_{ij}) = \frac{1}{2} k_C \sum_{i=1}^{\mathrm{N}} \sum_{j=1}^{\mathrm{N}} {\sum_{m_\wedge=-\mathrm{L}}^{\mathrm{L}}}' J_{ij}^{sre}(r_{ij}) = \frac{1}{2} k_C \sum_{i=1}^{\mathrm{N}} \sum_{j=1}^{\mathrm{N}} {\sum_{m_\wedge=-\mathrm{L}}^{\mathrm{L}}}' \frac{\mathrm{erfc}\left(\zeta \left|\vec{r}_{ij} + \vec{\mathrm{R}}\right|\right)}{\left|\vec{r}_{ij} + \vec{\mathrm{R}}\right|} \tag{4.2}$$

While $\vec{\mathrm{R}} = \sum_{\wedge=x,y,z} m_\wedge \vec{a}_\wedge$ is the position of each periodic unit box, $\vec{a}_\wedge$ is the box vector in each direction with $|\vec{a}_\wedge| = l$ implying a cubic box, $m_\wedge = (m_x, m_y, m_z) \in [-\mathrm{L}, \mathrm{L}] \subseteq (-\infty, \infty)$ are integer values, and $\vec{r}_{ij}$ equals the displacement vector between particles i and j in the central

box. The prime on the summation over periodic boxes is to indicate summation over all particle images (including self-images) in all periodic boxes with the exclusion of $i = j$ for $m = 0$.

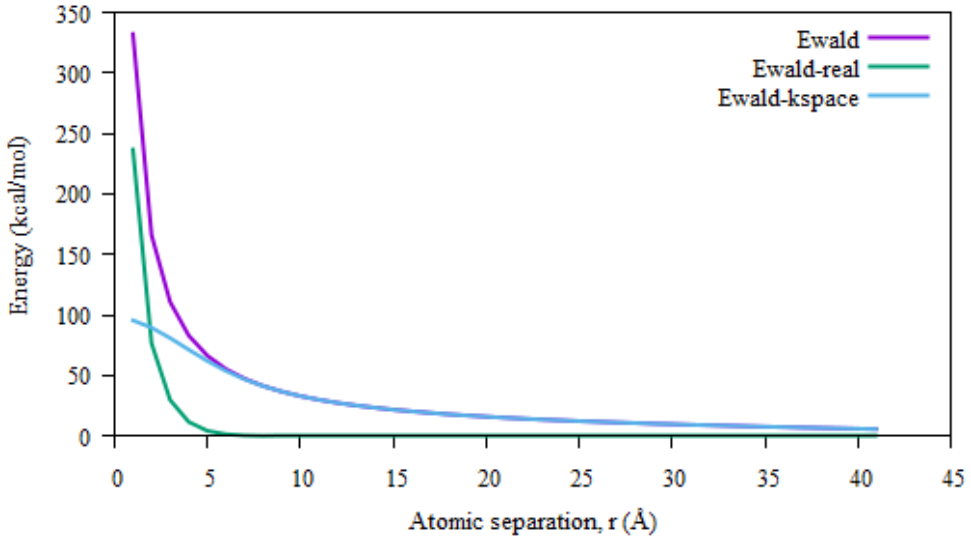

Figure 4. 2: Decomposition of the Ewald-modified Coulomb potential energy for NaCl. The energy value is inverted by -1 factor. The K-space contribution depicts the behavior of the Slater-type orbital evaluation of the Coulomb energy while the real-space component needs to be shielded.

In the numerical implementation, ζ is chosen so that the contribution to the sum of the real-space (short-range) energy is restricted to particles in the box for $m = 0$. This reduces the calculation of the real-space part to a normal minimum image convention (MIC) problem, which entails specifying a real-space short-distance cut-off $r_c \leq l/2$. This approach is widely adopted and implemented across MD simulators such as LAMMPS, GROMACS [61], and NAMD [141]. However, for a sharp distribution of charges, the approach requires a large value of ζ and the inclusion of a sufficient number of reciprocal vectors (k-vectors) in the Fourier-space summation part of the potential energy. The optimum ζ is chosen by balancing the error in (or the time needed to evaluate) the real- and reciprocal-space parts of the potential. Details of expressions for the choice of ζ, k-vectors and r_c are derived in [102], [142] – [144]. Therefore, letting $|\vec{r}_{ij}| = r_{ij}$ be the separation between two atoms in the central box, the short-range energy can be written as

$$V_{sre}(r_{ij} \leq r_c) = \frac{1}{2} k_C \sum_{i=1, j \neq i}^{\mathrm{N}} \frac{erfc(\zeta r_{ij})}{r_{ij}} \tag{4.3}$$

The origin of the high repulsive behavior of the Coulomb interaction potential at close separations between atoms is probed under the Ewald summation technique. The box

description is same as the previous ones except that we considered a dimer, NaCl, and computed the real- and Fourier-space contribution to the Ewald sum. From Figure 4.2, the Fourier-space component of the Ewald sum depicts the trend of the results from the shielded correction shown in Figure 3.4 from the empirical shielded function and the solution based on the Slater-type orbitals. However, the overall repulsive behavior of the Coulomb interaction potential is observed to originate from the inverse distance in V_{sre}, which results in unphysical energy contribution to the potential, especially at close atomic separations. Therefore, we modified the real-space contribution to account for short-range orbital overlap interaction. Thus, V_{sre} is expressed as:

$$V_{sre}(r_{ij} \le r_c) = \frac{1}{2} k_C \sum_{i,j}^{\mathrm{N}} \frac{erfc(\zeta r_{ij}^{shd})}{r_{ij}^{shd}} \tag{4.4}$$

$$r_{ij}^{shd} = \left(r_{ij}^3 + \gamma_{ij}^{-3}\right)^{1/3} \tag{4.5}$$

The force on the i^{th} particle is calculated as follows:

$$\vec{F}_i = -\frac{\partial V_{sre}}{\partial r_i} = -\frac{\partial V_{sre}}{\partial r_{ij}} \frac{\boldsymbol{\partial} r_{ij}}{\boldsymbol{\partial} \vec{r}_i} = -\frac{\partial V_{sre}}{\partial r_{ij}} \Delta_{r_i} r_{ij} \tag{4.6}$$

$$\vec{F}_i = \frac{r_{ij}}{\left(r_{ij}^3 + \gamma_{ij}^{-3}\right)^{4/3}} \left(erfc\left(\zeta \left(r_{ij}^3 + \gamma_{ij}^{-3}\right)^{1/3}\right) + \frac{2\zeta}{\sqrt{\pi}} \left(r_{ij}^3 + \gamma_{ij}^{-3}\right)^{1/3} e^{-\zeta^2 \left(r_{ij}^3 + \gamma_{ij}^{-3}\right)^{2/3}} \right) \vec{r}_{ij} \tag{4.7}$$

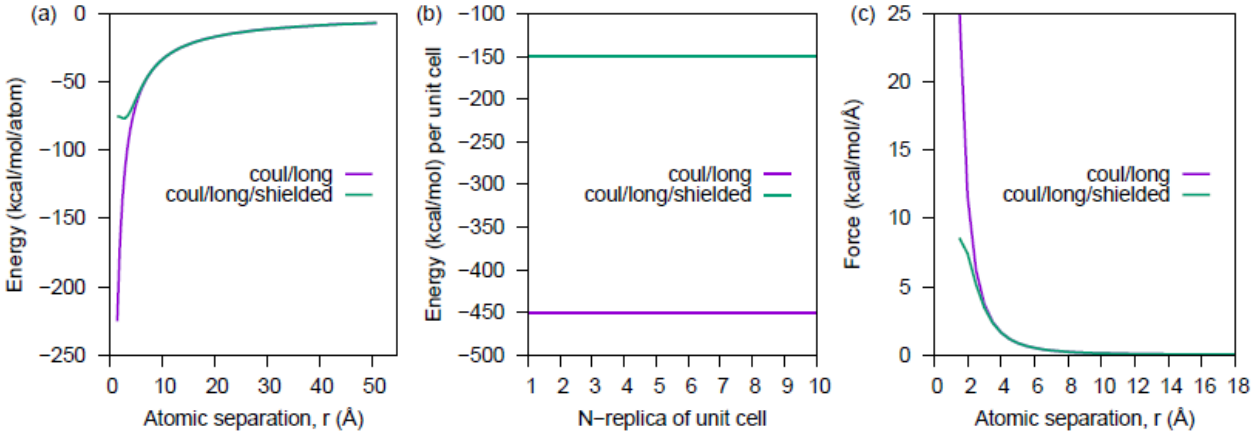

Figure 4. 3: Effect of shielding inclusion to long-range Coulomb with NaCl crystal (a) energy per atom, (c) force on an atom against atomic separation, and (b) energy per unit cell volume as a function of replicated unit cell with(without) shielded correction.

The shielded correction is implemented in LAMMPS as a standalone pair-interaction style called “coul/long/shielded”. The effect of including the shielded correction is tested on a NaCl crystal with the shielded coefficients (gamma parameters) of 0.40 and 0.35 Å^{-1} for Na and Cl

taken from [145]. Figure 4.3 shows the plot of the energy against the interatomic separation and the energy per unit cell volume against supercell size with/without using the shielded function. The results depict the expected effect when compared with the plot in Figure 3.4 for the solution (via Slater integral) and the empirical functions. Also, the energy per unit volume as a function of the increased size of the supercell is constant as expected. Concisely, we see that the interaction energy as well as the forces (Figure 4.3c) are consistently shielded at short interatomic distances, which is an improvement to unphysically repulsive energy and forces recorded when atoms are at a small separation of the order of the vdW diameter or less.

4.1.3 Long-range Coulomb Force with ReaxFF

A reactive MD simulation requires a reactive force field to model the bond activities and chemical reactions. In addition to highlights in section 3.2.2.3, irrespective of atomic connectivity, ReaxFF includes the Taper correction functions and the shielded electrostatic interaction (Eq. (3.24) explained in section 3.3.2) between atomic pairs within a short-range distance cut-off for computational speed. However, opportunities to include the long-range Coulomb in ReaxFF MD simulation is available in LAMMPS via a hybridization command of two or more pair potentials. Preliminary investigation of ReaxFF to compute Coulomb forces on atom i at various separations from atom j shows an inability of ReaxFF with/without (blue/purple curves of Figure 4.4) long-range Coulomb to reproduce Ewald results (green curve in Figure 4.4). To understand the origin of this discrepancy, we examined the use of "hybrid" and "hybrid/overlay" styles commands with "reaxff" and any "coul/long" pair interaction potentials in LAMMPS. The discrepancy in the Coulomb forces comes from the inability of the shielded direct Coulomb potential to account for the real-space short-range part of the Ewald sum. Thus, the shielded Coulomb potential given in Eq. (3.24) is incompatible with the long-range part of Ewald sum. We corrected this anomaly by implementing a shielded long-range Coulomb function for ReaxFF in LAMMPS that is triggered whenever ReaxFF is hybridized with Ewald or P3M method. The implementation (Eqs. 4.4 – 4.7) accounts for the real-space short-range part of the Ewald sum. Figure 4.4 (orange curve) shows an improvement on accounting for the real-space short-distance part of long-range Coulomb. We could see a striking agreement between the Ewald (green curve) and ReaxFF plus shielded long-range correction within the 10 Å cut-off. Without the shielded correction at short distances, our long-range extension to ReaxFF matches exactly the Ewald (green curve). We expect that with this correction, a proper description of the slowly decaying Coulomb interaction with the shielded

function in the reactive MD simulation of electrochemical processes of atoms within a dielectric layer in a large system.

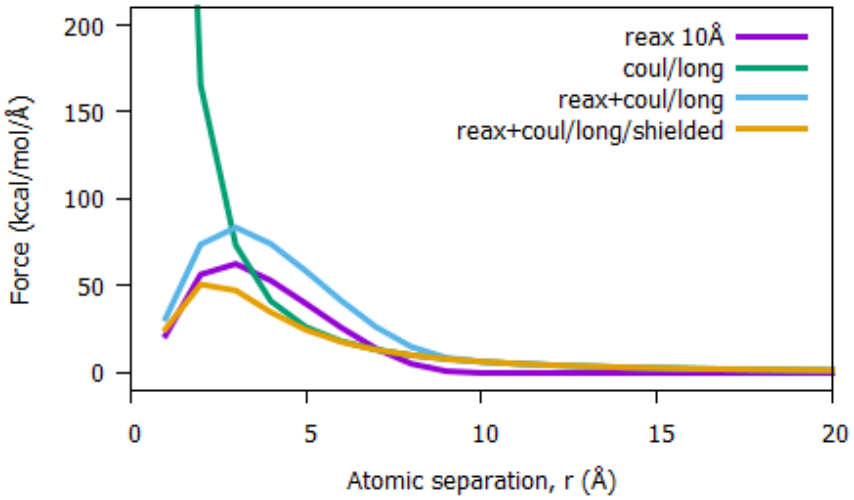

Figure 4. 4: Comparison of ReaxFF Coulomb forces on one of the Cl atoms in $MgCl_2$ molecule with and without long-range effect and shielded correction against coul/long (green curve) force.

Moreover, one should choose an appropriate model that will effectively handle the Coulomb interaction based on the size of the system. For instance, ReaxFF or short-range Coulomb may suffice for describing Coulomb interaction in small molecular systems in which atomic separations do not go farther than 10 Å. ReaxFF with shielded long-range Coulomb should give a good description of the Coulomb interaction for large systems.

4.2 Partial Charge Estimation Models

4.2.1 QEq (Charge Equilibration) Model

Rappé and Goddard's [29] development of QEq applied the most fundamental properties (the ionization energies, the electron affinities, and the atomic radii) of atoms to describe the energy cost of changing the charge state of an isolated atom by ± 1. The atomic electronegativity and hardness were represented in terms of the ionization energy and electron affinity (detailed relation among these quantities is contained in the original paper [29] and are summarized in appendix A.1.), while the total electrostatic energy of a molecular system was expressed as the sum of the individual atomic energy contributions from the constituent atoms, as presented:

$$E_{sys}(Q_1, \dots, Q_N) = \sum_{i=1}^{N} \left(E_i^0 + Q_i \chi_i^0 + \frac{1}{2} Q_i^2 J_{ii}^0 \right) + \sum_{i<j}^{N} Q_i Q_j J_{ij} \qquad (4.8)$$

where i and j run over N atoms, E_i^0 is the energy of an atom in its reference charge state usually taken to be neutral, χ_i^0 and J_{ii}^0 are the Mulliken [146]–Pauling [147] atomic electronegativity and Parr–Pearson [148] atomic hardness, respectively. The last term in Eq. (4.8) is the Coulomb interaction energy between atoms with charges Q_i and Q_j separated by r_{ij}. The kernel J_{ij} of the Coulomb interaction is explained in section 3.3 and it is given by Eq. (3.24) in ReaxFF and QEq with a seventh – order Taper correction function [120]. The Taper correction function is a polynomial function that reduces the non-bonded interaction to zero at a finite cutoff distance by ensuring that the first, second and third derivatives of the potential continuous at cutoff point.

The atomic chemical potential μ and/or the electronegativity χ of the atoms represents the derivative of the energy with respect to the number of electronic charges, N (see [150]). In terms of charge, χ_i is obtained by taking the partial derivative of the energy of the molecular system with respect to the atomic charges associated to each atom, i.e., $\partial E_{sys}/\partial Q_i$, which is in accordance with Politzer and Weinstein [149]. Therefore, derivative of Eq. (1) with respect to Q_i leads to the following QEq equation in the form of atomic-chemical potential.

$$\chi_i(Q_1, \cdots, Q_N) = \frac{\partial E_{sys}}{\partial Q_i} = \chi_i^0 + Q_i J_{ii}^0 + \sum_{j \neq i}^{N} Q_j J_{ij} \tag{4.9}$$

At chemical equilibrium, every pair of atoms sees the same chemical potential and has the same electronegativity. At this point, the system is in a chemical equilibrium state. Any further changes in the system configuration result in the re-adjustment of the atomic charges until they possess the same electronegativity or chemical potential. The condition of chemical equilibrium allows us to equate electronegativity to one another. Thus,

$$\frac{\partial E_{sys}}{\partial Q_i} = \frac{\partial E_{sys}}{\partial Q_j} = \cdots = \frac{\partial E_{sys}}{\partial Q_N} \Longrightarrow \chi_1 = \chi_2 = \cdots = \chi_N \tag{4.10}$$

Eq. (4.10) results in $N - 1$ equations, and the condition that the sum of the individual atomic charges in the system equals the total charge of the system, i.e., $\sum_{i=1}^{N} Q_i = Q_T$. This leads to N linear equations, which can be formulated in a matrix format (see appendix A.1). One can then solve for the atomic charges Q_i.

4.2.1.1 Computation of Charge with QEq and Limitations

At this point, we apply the LAMMPS software package to compute charges using the implemented QEq to analyze the effects of short- and long-range Coulomb interaction pair potentials. For simplicity, we consider a NaCl dimer instead of a triatomic molecule. Like the previous calculation, we compared the charges as a function of separation with and without the short-distance cut-off. From Figure 4.5, charges computed with and without long-range inclusion have converged as the distance cut-off increases to 10 Å. The calculation provides an understanding about the application of Ewald technique from the force computation perspective for charge determination. Summarily, the results show no difference between charges computed with and without long-range Coulomb, which supports the claim that the long-range calculation implemented (via Ewald or PPPM method) in LAMMPS is specialized for force computation and does not apply in charge calculations. Evidently, charge equalization techniques and force computations are independent calculations. Computation of forces both at short- and long-range Coulomb interactions in LAMMPS is done using the geometry-dependent charge distributions determined only based on short-range Coulomb interaction within the conventional charge equalization method. The calculation of the Coulomb forces using a short distance determined charges arises from the irrelevance of whatever manner the charges are determined. Once the charge is calculated and supplied to compute the forces, the job is done. However, from the analyses of the non-bond forces, while atoms beyond the short-distance Coulomb interactions are not accounted for, their contributions appear too significant to be neglected. It would be desirable to explore and include the effect of long-distance interactions in computation of charges for applications in electrochemical processes.

An additional indication from the calculations is the violation of chemical charge neutrality. The neutrality implies that each of the two molecules or atoms at a large separation in vacuum must be neutral [151] – [154]. Mathematical evidence of the limitation of QEq regarding unreasonable charge neutrality at large separations can be deduced for a dimer using Eq. (4.9) and $\sum_{i=1}^{N} Q_i = Q_T$. The charges of the atoms in a dimer are given as:

$$Q_1 = -Q_2 = \frac{\chi_1^0 - \chi_2^0}{J_{11}^0 + J_{22}^0 - 2J_{12}} \tag{4.11}$$

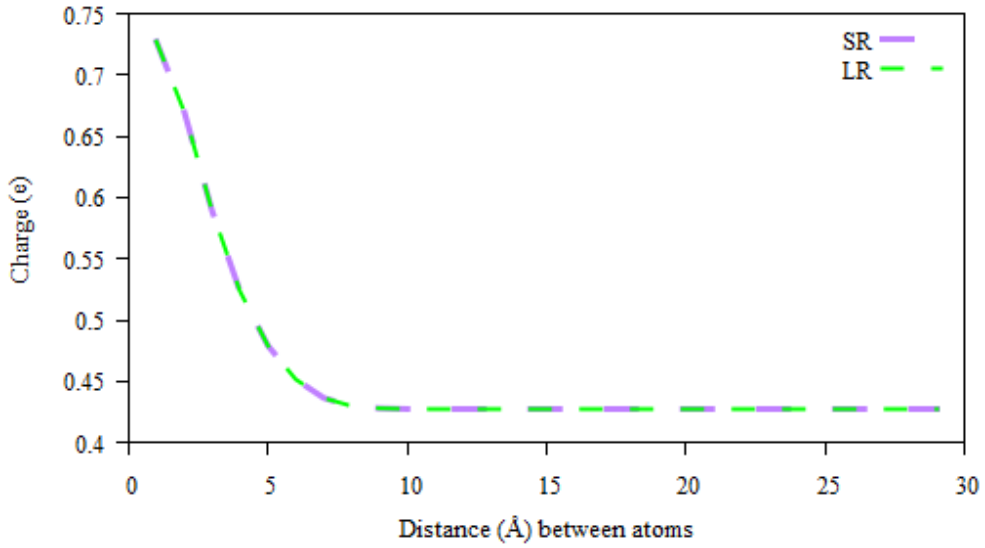

Figure 4. 5: QEq charges for Na in NaCl computed without (SR) and with (LR (Long Range)) long-range Coulomb interaction potential implemented in LAMMPS. There is no difference between the charges computed with the two models.

The coulomb pair interaction term, J_{12} is a function of the separation r_{12} between the atoms. Therefore, the charges vary as long as J_{12} varies within specified cut-off distance. Beyond the cut-off at a large separation, J_{12} diminishes to zero and the denominator becomes a constant. Therefore,

$$\lim_{r_{12}\to\infty} Q_1 = \lim_{r_{12}\to\infty} \frac{\chi_1^0 - \chi_2^0}{J_{11}^0 + J_{22}^0 - 2J_{12}} = \frac{\chi_1^0 - \chi_1^0}{J_{11}^0 + J_{22}^0} \neq 0 \text{ but a constant value} \qquad (4.12)$$

Intuitively, Eq. (4.12) based on QEq is problematic and the charge evaluation schemes have been reformulated to account for dissociation of atoms and properly include polarization effects [125], [152] – [154]. Otherwise, even at infinite separation, charge distribution would continue to show impractical long-distance constant charge transfer, and thus, incorrectly addresses the dissociation and polarization problems. Several techniques have been put forward toward resolving the shortfalls with QEq. While a few techniques focused on imposing either molecular charge constraints [155], harmonic molecular dipole restraints [156] or long-distance restraints on the electronegativity differences [153], [154], the most successful approaches utilized concepts from valence bond theory [152] – [154] with a distance-dependent electronegativity [125], [152] to achieve the correct dissociation limit. Despite QEq's shortfall and recent advancements in the methods, QEq remained the most-sort-after environment-dependent charge estimation technique widely implemented and applied in reactive molecular dynamics simulations. This could be related to lack of parameters across a broad class of

molecular systems and the enormous number of fitting parameters in the more advanced methods.

4.2.2 Split Charge Equilibration (SQE)

In recognition of the drawbacks with QEq and in attempts to proffer solutions with transferability of parameters to a broader class of molecules, SQE model [38] simultaneously utilized bond- and atom-based descriptions to include chemical bonding effects not originally contained in QEq. The earlier concept of split charge was based purely on bond-space [157], which was introduced in the induced dipole moment and energy (IDME) [158] method for calculating dipole moment and charge distribution; an example is the atom-atom charge transfer (AACT) [156] scheme. In SQE, charges are only allowed to flow between covalently bonded atoms; this corrects the unrealistic constant charge transfer in QEq and makes possible further generalizations that are absent in the original QEq; however, the application of split charges is restricted to bonded atoms. The use of the notion of split charges to reflect the bond-dependent property of charges results in rewriting the potential energy in terms of bond parameters rather than atomic parameters. In rewriting Eq. (4.7), the SQE developers introducted an additional isotropic simple harminic-like energy [159] term $\frac{1}{2}\kappa_{ij}^{(s)}q_{ij}^2$; where the displacement variable is replaced with the so-called "split charge" q_{ij} and the force constant is characterized as the "bond hardness" κ_{ij}; leading to:

$$E(\{r_i\}\{Q_i\}) = \sum_i \left(E_i^0 + \chi_i Q_i + \frac{1}{2}\kappa_i Q_i^2\right) + \sum_{i<j}\left(\frac{1}{2}\kappa_{ij}^{(s)}q_{ij}^2 + Q_i Q_j J_{ij}(r_{ij})\right) \tag{4.13}$$

where κ_i and χ_i represent the atomic hardness and atomic electronegativity, respectively. The split charge represents the charge flown from a covalently bonded neighbor atom j to atom i while the net charge, Q_i of an atom is related to the split charge q_{ij} by:

$$Q_i = \sum_j^N q_{ij} \tag{4.14}$$

Eq. (4.14) is the sum of the split charges debited and credited to an atom by the covalently bonded neighbors. Based on bond connection, the electronegativity differences between two atoms are represented by an arbitrary value $\bar{\chi}_{ij}$. So, with the SQE net charge (Eq. (4.14)), the potential energy (Eq. (4.13)) of a system of N atoms; where $J_{ij}^{i'j'}$ is Coulomb interaction kernel; is written as

$$E_{SQE}(\{r_i\}\{Q_i\}) = \frac{1}{2}\sum_{i,j}\left(\kappa_i \sum_j q_{ij} + \bar{\chi}_{ij} + \kappa_{ij}^{(s)} q_{ij}\right) q_{ij} + \frac{1}{2}\sum_{i<j,i',j'} q_{ij} J_{ij}^{i'j'} q_{i'j'} \qquad (4.15)$$

The one-half factor in the last term of Eq. (4.15) accounts for double counting over summation on i' and j'. The reference energy, E_i^0 is not considered because it neither contributes to the charge distribution nor to partial charge of the atoms. The atomic hardness κ_i is influenced by the chemical nature of the atoms, to which it is bonded to, therefore, in relation to the atomic hardness of a connected neighbor atom j, some authors replaced κ_i with κ_{ij}^0, which is an intrinsic or irreducible two-body parameter [155], [156]. However, Nistor and Müser [38] defined κ_i in relation to the entire product $\kappa_i \sum_j q_{ij}$ as a linear average of the difference between the product of κ_i and its Q_i and the product of κ_j and it is Q_j of covalently bonded neighbor atom j, i.e.

$$\kappa_i \sum_j q_{ij} = \frac{1}{2}(\kappa_i Q_i - \kappa_j Q_j) \qquad (4.16a)$$

Additionally, the singly indexed atomic parameters were transformed into doubly indexed linear combination of atomic and bond parameters, which are expressed as linear average of sums or differences of the atomic quantities.

$$\kappa_i \sum_j q_{ij} = \kappa_{ij}\bar{Q}_{ij} + \bar{\kappa}_{ij} Q_{ij} \qquad (4.16b)$$

$$Q_{ij} = \frac{(Q_i + Q_j)}{2} \text{ and } \bar{Q}_{ij} = \frac{(Q_i - Q_j)}{2} \qquad (4.17a)$$

$$\kappa_{ij} = \frac{(\kappa_i + \kappa_j)}{2}, \qquad \bar{\kappa}_{ij} = \frac{(\kappa_i - \kappa_j)}{2} \text{ and } \bar{\chi}_{ij} = \chi_i - \chi_j \qquad (4.17b)$$

Eq. (4.17b) are the so-called "charge equilibration rules," which make Eq. (4.19) similar in form and relation to Eq. (4.8). It is important to note that the following relations hold true in the SQE scheme:

$$i.\ q_{ij} = -q_{ji} \quad \text{ii. } \bar{\chi}_{ij} = -\bar{\chi}_{ji} \quad \text{iii. } \kappa_{ij} = \kappa_{ji} \quad \text{iv. } \bar{\kappa}_{ij} = -\bar{\kappa}_{ji} \quad \text{v. } \kappa_{ij}^{(s)} = \kappa_{ji}^{(s)} \qquad (4.18)$$

The introduction of the two-body parameters in the QEq technique makes the parametrization of several other schemes [38] possible through setting one or two parameters to zero in the

general SQE potential energy equation. Thus, we re-express Eq. (4.15) using Eq. (4.16b) in a mixed atomic and split charge forms as:

$$E_{SQE}(\{r_i\}\{Q_i\}) = \frac{1}{2}\sum_{i,j}\left(\kappa_{ij}^{(s)} q_{ij} + \kappa_{ij}\bar{Q}_{ij} + \bar{\kappa}_{ij}Q_{ij} + \bar{\chi}_{ij}\right)q_{ij} + V_C \tag{4.19}$$

$$V_C = \frac{1}{2}\sum_{i<j,i',j'} q_{ij}J_{ij}^{i'j'}q_{i'j'} \quad and \quad J_{ij}^{i'j'} = J_{ii'} - J_{ij'} - J_{ji'} + J_{jj'} \tag{4.20}$$

where each term in $J_{ij}^{i'j'}$ is a Coulomb interaction kernel and they are evaluated with Slater integral function; thus, orbital overlap of electronic wave function of two interacting atoms is accounted for. The SQE equivalence of the QEq electrochemical and/or chemical potential equilibration condition requires that.

$$\frac{\partial E_{SQE}}{\partial q_{ij}} = 0 \quad \text{and} \quad \frac{\partial Q_i}{\partial q_{jk}} = \delta_{ij} - \delta_{ik} \tag{4.21}$$

provided the E_{QEq} and E_{SQE} correspond in form and relation while also abiding by the charge equilibration rules, Eqs. (4.17b). Applying Eq. (4.21) on Eq. (4.19) with respect to a generic split charge indexed $q_{kk'}$ leads to a system of $N-1$ independent linear equations in $N-1$ unknowns.

$$-\bar{\chi}_{kk'} = 2\kappa_{kk'}^{(s)}q_{kk'} + \frac{1}{2}\sum_{i}^{N}(L_i q_{ki} - M_i q_{k'i}) + J_{kk'} \tag{4.22}$$

$$L_i = (\kappa_{kk'} + \bar{\kappa}_{kk'} + \kappa_{ki} + \bar{\kappa}_{ki})$$

$$M_i = (\kappa_{k'k} + \bar{\kappa}_{k'k} + \kappa_{k'i} + \bar{\kappa}_{k'i})$$

$$J_{kk'} = \sum_{i}^{N}\sum_{j=i+1}^{N}\left(J_{ik} - J_{ik'} - J_{jk} + J_{jk'}\right)q_{ij}$$

For details of SQE differentiation with respect to generic charge $q_{kk'}$, see appendix A.2. Though Eq. (4.22) can be formulated in similar compact matrix form $\boldsymbol{A}\cdot\boldsymbol{q} = -\boldsymbol{b}$ as the QEq equation, it differs from QEq in order and element compositions. Here, $\boldsymbol{A}$ is a matrix of $m \times m$ order ($m = N-1 =$ the number of split charges nsq or the number of bonds in a molecule) whose elements are sums of $\kappa_{kk'}^{(s)}$, L_i, M_i, and $J_{kk'}$ terms ($\kappa_{kk'}^{(s)}$ is actually a diagonal matrix). $\boldsymbol{q}$ and $\boldsymbol{b}$ are each a m column vector respectively for the split charges and the differences in

atomic electronegativity formed explicitly from covalently connected atoms. Appendix A.2 contains illustrative expansion of Eq. (4.22) for methanol.

In this scheme, in which the QEq rules are obeyed, there are two parameters (χ_i and κ_i) per atom type and one parameter $\kappa_{ij}^{(s)}$ per bond. The bond is also assumed to be well defined, i.e., only covalently bonded atoms are considered in determining the doubly indexed parameters. In this work, we did not seek to fit the input parameters but utilized the provisions made in [38] for the computational implementation of the SQE model; however, except for the bond hardness, the per atom parameters could be obtained from any reactive force field file that contains the interaction parameter of the atoms of the molecules under study. The test systems for SQE in this study are subsets containing Carbon (C), Hydrogen (H) and Oxygen (O).

Table 4. 1: Comparison of atomic partial charges on propane-2,2-diol with molecular formula $(CH_3)_2C(OH)_2$ and structure shown in Figure 4.6. Ab initio ESP charge are from [38].

Atom	*Ab initio*	QEq	SQE
C 1	0.6707	0.7894	0.6283
O 2	-0.6334	-0.5363	-0.6150
O 3	-0.6338	-0.5363	-0.6151
C 4	-0.4230	-0.3110	-0.3482
C 5	-0.4237	-0.3113	-0.3491
H 6	0.3800	0.2211	0.4153
H 7	0.3802	0.2211	0.4153
H 8	0.1280	0.0792	0.0917
H 9	0.1138	0.0857	0.0684
H 10	0.0994	0.0667	0.0739
H 11	0.1139	0.0857	0.0686
H 12	0.0996	0.0667	0.0740
H 13	0.1283	0.0794	0.0920

Table 4.1 shows that SQE predicted partial charges improved over QEq. It shows that SQE is more accurate at a root mean square error (rmse) of 11.05% compared with the *ab initio* electrostatic potential (ESP) fitted charges against 24.34% of the QEq. The improved accuracy of SQE over QEq is reportedly attainable because of the perturbative additions to the atomic hardness and electronegativity, which are $\Delta\kappa_{ij}$ and $\Delta\chi_{ij}$ respectively. The additions were added over all covalently bonded atoms j to atom i so that $\kappa_i = \kappa_i^0 + \sum_j \Delta\kappa_{ij}$ and $\chi_i = \chi_i^0 + \sum_j \Delta\chi_{ij}$. The superscripted terms are the original atomic hardness and electronegativity of atom i and the perturbative additions depends on the type of bonds existing between atoms i and j. Such additions come at the expense of additional fit parameters [130] and deviation from the symmetry relationships given in Eq. (4.18), i.e., $\Delta\kappa_{ij} \neq \Delta\kappa_{ji}$ and $\Delta\chi_{ij} \neq \Delta\chi_{ji}$. The perturbative

additions provide better background to account for the effect of chemical environment on the atomic hardness and electronegativity. We investigate the ability of SQE to address the charge neutrality drawback recorded with QEq by comparing the behavior of charge computed with QEq and SQE against increasing separation between atoms in a water molecule. The H – O – H bond angle was set $104.5°$ and one of the O – H bonds was maintained at 0.97 Å while the other O – H bond length was varied at 0.1 Å$/fs$. Figure 4.7 shows that translating the atomic parameters into bond (two-body) parameters resolved the charge neutrality artifact originally predicted by QEq. Such a milestone could not be possible in SQE without the incorporation of a threshold cut-off value, which is about 0.2 Å higher than the chemical bond length of any two atoms concerned.

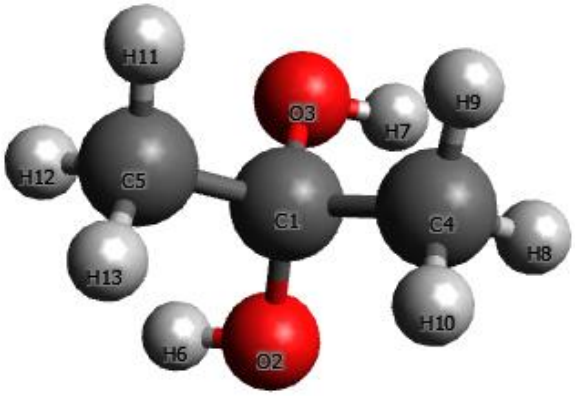

Figure 4. 6: Atoms in the $(CH_3)_2C(OH)_2$ molecules with charges specified in Table 4.1 as calculated by QEq and SQE, then compared with *ab initio* ESP from [130].

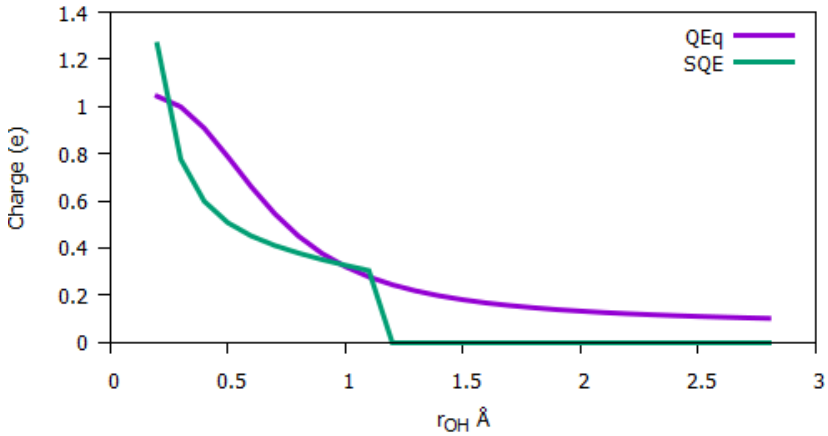

Figure 4. 7: Comparison of charge on H atom as a function of bond distance in dissociating H_2O molecule. QEq (purple curve) predicts resultant net charge even at large separation between molecules. SQE (green curve) resolved the problem but raised discontinuity issues.

Our expectation of dissociated molecules or atoms isolated from their parent molecules to be electrically neutral is fulfilled with SQE. However, its application in MD simulations

reintroduces the need for *ab initio* assignment of cut-off distances for every pair of atom types in the molecular system. Applying a global cut-off to accommodate every covalent bond is permissible though would entail over- and/or under-coordination for some atoms, which would result in the estimation of split charges for unwarranted over- and/or under-coordination bonds. Since SQE is restricted to covalently bonded atoms, it deprecates intermolecular interaction, which would be allowed by using larger global cut-off or when two molecules are close enough that the distance between atoms from each molecule are within the specified cut-off; again, one must decipher means to handle over- or under-coordination in such cases. Also, only covalently bonded occasions are allowed implies SQE would fail in MD simulations when bonds are allowed to break. Suggestively, this could be remedied if the method is extended to include bond breaking and hybridization effects; this direction would be accessible via empirical reactive bond-length and bond-order potentials [121], [122], which is lacking in the present SQE. Another observation from Figure 4.7 is the cut-off has no effect on the final charge provided the atoms are chemically bonded, otherwise, there is a sharp drop in charge at cut-off point indicating a deviation from continuous charge distribution predicted in atom-condensed Kohn-Sham DFT approximated to second order (ACKS2) method [125] and in charge transfer with polarization current equalization [152] around dissociation limit. Although this could be less a fundamental problem than the earlier stated issues, it does result in undesirable discontinuous charge change during bond breaking.

4.2.3 LrQEq ≡ QEqLR (Long-range Charge Equilibration) Model

The Coulomb electrostatic energy can be written in terms of two contributions: long-range, V_{lr} and short-range, V_{sr} terms, plus a spurious self-interaction energy term. Modifying the Coulomb interaction energy by splitting it into long- and short-range terms has been used to represent the Coulomb interaction potential. In the decomposition scheme, the Coulomb electrostatic energy is replaced with the Ewald [136] summations such that the real alongside the self-interaction terms consist of the short-range term, while the reciprocal part that has no singularity is the long-range term. In similar spirits and as exemplified in [160], the Ewald-modified-Coulomb electrostatic energy of particle i in a unit cell of lengths lx, ly and lz interacting with particle j in N particles system, and with the periodic images of the particles (including particle i's images) over the L number of translated unit cells except for cases where $i = j$, can be expressed from Eq. (3.27 & 3.28) as:

$$V_{Coul} = \frac{k_C}{2} \sum_{\substack{i,j \\ j \neq i^*}}^{N} Q_i Q_j \sum_{u,v,w=-L}^{L} \left(\frac{erfc(\zeta r_{ij})}{r_{ij}} + \left(\frac{4\pi}{\mathrm{V}}\right) \frac{\cos(\vec{k} \cdot \vec{r}_{ij})}{k^2} \exp\left(-\frac{k^2}{4\zeta^2}\right) \right) - \frac{k_C \zeta}{\sqrt{\pi}} \sum_{i=1}^{N} Q_i^2 \quad (4.23)$$

where $r_{ij} = \left|\vec{r}_{ij} + u\vec{a}_1 + v\vec{a}_2 + w\vec{a}_3\right|$ equals the radial distances (in Å) between two atoms in real space and $\vec{k} = u\vec{b}_1 + v\vec{b}_2 + w\vec{b}_3$ are the reciprocal vectors in inverse Å. $(\vec{a}_1, \vec{a}_2, \vec{a}_3)$ and $(\vec{b}_1, \vec{b}_2, \vec{b}_3)$ are the translational real-space and reciprocal unit cells, respectively and $(u, v, w) \in [-\mathrm{L}, \mathrm{L}] \subseteq (-\infty, \infty)$ are integer vectors describing the repeated unit cells. Notice that the long-rang part is represented as a trigonometric function. That was obtained after substituting Eq. (3.28) into Eq. (3.27) and using the trigonometric expansion of the exponential function with complex identity; but, because partial charges represent a real physical property of an atom, the concept of imaginary or complex values does not apply to charges, thus, the imaginary part (sine part) of the expansion is dropped. We recall that while both equations represent Ewald-modified-Coulomb interaction energy, Eq. (3.27) represents real and imaginary (complex) components of the energy, and Eq. (4.23) gives only the real part of the energy. For the QEqLR ≡ $LrQEq$ model, we replace the Coulomb interaction energy function in Eq. (4.8) with Eq. (4.23) to obtain the total energy of a system. See appendix A.3 for information on the contributions to the Coulomb energy.

$$E(Q_1, \ldots, Q_N) = \sum_{i=1}^{N} \left(E_i^0 + Q_i \chi_i^0 + \frac{1}{2} Q_i^2 J_{ii}^0 + V_{Coul} \right) \quad (4.24)$$

Comparison of the plots of the real- and Fourier-space (Figure 4.2) components of the Ewald summation of the Coulomb potential with the solution (via Slater-type orbital, Figure 3.4) of the Coulomb interaction potential shows that the real-space short-range part (i.e., the kernel of the first term at the right of Eq. (4.23)) results in unphysical energy contributions. The high energy value is an attribute of the singular point presence or the inverse distance factor; the reciprocal space part (i.e., the kernel of the second term at the right of Eq. (4.23)) has no singularity. The high energy contribution from the real-space part manifests, especially when two atoms are at a close distance of the order of vdW diameter between them or simply when the atomic orbitals overlap in the central box, which in some other developments [161] are called buried atoms. Of course, two particles or orbitals can overlap with high but finite energy value provided PEP (Pauli Exclusion Principle) holds. Therefore, we remedied this by modifying the real space contribution with an incorporation of a shielding correction function

when the interaction between atoms is in the central box and we denote this modified function as V_{sr}, and the counterpart (the kernel of the second term at the right of Eq. (4.23)) as V_{lr}.

$$V_{sr}(r_{ij}) = \begin{cases} \dfrac{erfc(\zeta r_{ij}^{sc})}{r_{ij}^{sc}};\ v = u = w = 0;\ r_{ij}^{sc} = \left(r_{ij}^{3} + \gamma_{ij}^{-3}\right)^{1/3} \\ \dfrac{erfc(\zeta r_{ij})}{r_{ij}};\qquad otherwise \end{cases} \tag{4.25}$$

The shielding correction function has wide application in QEq and reactive force field (ReaxFF) [28] for MD simulations in LAMMPS and does not require additional fitting parameter/s. While ζ represents the Ewald splitting term in inverse distance unit, V is the real-space unit cell volume in distance units, i.e., $\mathrm{V} = |\vec{a}_1 \cdot (\vec{a}_2 \times \vec{a}_3)| = lx * ly * lz$. The factor of one-half in Eq. (4.23) takes care of double counting and k_C is the Coulomb constant. The contraction, $j \neq i^{\star}$ is used to denote two aspects of the sum:

(1) When- and where-ever '$\star$' is retained implies that $j = i$. This corresponds to a situation where $u = v = w = 0$ is skipped, which is an indication that atoms in the fundamental unit cell interact with their periodic images in the translated unit cells; and
(2) When- and where-ever '$\star$' is dropped indicates that $j \neq i$ and terms are maintained the way they are. This includes cases where $u = v = w = 0$ and all possible sets of u, v, w. Here, atom i interacts with atoms j and with the periodic images of atoms in the translated unit cells but not own selves and their own images.

Like in QEq, the total energy (Eq. 4.24) is differentiated as a function Q_i following Eq. (4.10) and the decomposition of $j \neq i^{\star}$ explained in items 1 & 2 above. The introduction of long-range Coulomb to the QEq led to the modification of the J terms in Eq. (4.9). The derivatives yield the chemical potentials Eq. (4.26) of the systems, which is rewritten for the QEqLR as Eq. (4.27).

$$\chi_i(Q_1, \cdots, Q_N) = \chi_i^0 + Q_i J_{ii}^0 + \frac{k_C}{2}\left(\sum_{j\neq i}^{N} Q_j \sum_{u,v,w=-L}^{L} V_{sr}(r_{ij}) + 2Q_i \sum_{\substack{u,v,w=-L \\ u=v=w\neq 0}}^{L} V_{sr}(r_{ii}^{\star})\right)$$
$$+ \frac{k_C}{2}\left(\sum_{j\neq i}^{N} Q_j \sum_{u,v,w=-L}^{L} V_{lr}(k) + 2Q_i \sum_{\substack{u,v,w=-L \\ u=v=w\neq 0}}^{L} V_{lr}(k^{*})\right) - 2\frac{k_C \zeta}{\sqrt{\pi}} Q_i \tag{4.26}$$

$$\chi_i(Q_1,\cdots,Q_N) = \chi_i^0 + Q_i J_{ii}^0 + \left(Q_i J_{ii}^{EC} + \sum_{j\neq i}^{N} J_{ij}^{EC} Q_j \right) \tag{4.27}$$

where J_{ij}^{EC} is the Ewald-modified-two-center-Coulomb terms with shielding correction on the real-space part. J_{ii}^{EC} can be interpreted as the chemical hardness of atom i due to long-range inclusion via Ewald sum. It is a constant value for a given system and adds to the atomic chemical hardness of each atom (see Eq. (4.29)) or to the net Ewald-modified Coulomb interaction term of each particle, as depicted in Eq. (4.27). The terms in Eq. (4.27) are defined as given in Eq. (4.28). They are results of implementing the contraction $j \neq i^{\star}$ (see items 1 and 2).

$$\begin{cases} J_{ij}^{EC} = \dfrac{k_C}{2}\left(\displaystyle\sum_{u,v,w=-L}^{L} \left(\begin{cases} \dfrac{erfc(\zeta r_{ij}^{sc})}{r_{ij}^{sc}}; u=v=w=0; \\ \dfrac{erfc(\zeta r_{ij})}{r_{ij}}; \quad otherwise \end{cases} + \left(\dfrac{4\pi}{\mathrm{V}}\right)\dfrac{cos(\vec{k}\cdot\vec{r}_{ij})}{k^2}\exp\left(-\dfrac{k^2}{4\zeta^2}\right) \right) \right); j \neq i \\ J_{ii}^{EC} = k_C \left(\displaystyle\sum_{\substack{u,v,w=-L \\ u=v=w\neq 0}}^{L} \left(\dfrac{erfc(\zeta r_{ii})}{r_{ii}} + \left(\dfrac{4\pi}{\mathrm{V}}\right)\dfrac{cos(\vec{k}\cdot\vec{r}_{ii})}{k^2}\exp\left(-\dfrac{k^2}{4\zeta^2}\right) \right) - 2\dfrac{\zeta}{\sqrt{\pi}} \right); \quad j = i \end{cases} \tag{4.28}$$

Note that L is the number of unit cells considered in real- and reciprocal-spaces (L may not be equal in the two spaces). Optimum L is determined via a convergence test of charge or energy against increasing L. The QEqLR equation Eq. (4.27) was written to keep the Coulomb interaction terms from the atomic energy cost of changing the charge state of an atom by $\pm$ 1. The Eq. (4.27) can also be cast after QEq equation as Eq. (4.29), and $J_{ii}^{0EC} = J_{ii}^0 + J_{ii}^{EC}$ serves as the Ewald-modified chemical hardness of atom i.

$$\chi_i(Q_1,\cdots,Q_N) = \chi_i^0 + Q_i J_{ii}^{0EC} + \sum_{j\neq i}^{N} J_{ij}^{EC} Q_j \tag{4.29}$$

The QEqLR equation is linear and can be solved in analogous way as QEq (appendix A.1) in cognition of the condition that the sum of the charge on individual atoms equals the total charge of the system, zero if the system is neutral.

$$\sum_{i=1}^{N} Q_i = Q_{TOT} \tag{4.30}$$

QEqLR retained the atomic electronegativity and hardness of the original QEq work by Rappé and Goddard with an additional constant term J_{ii}^{EC} arising from atomic interaction with self-

images, which resists charge separation alongside J_{ii}^{0} while χ_i^0 and J_{ij}^{EC} favor charge separation. Eq. (4.29) leads to a $N \times N$ set of linear equations on the conditions of Eqs. (4.10 & 4.30) and are written in a matrix form as $\boldsymbol{C}_{ij}\boldsymbol{Q}_i = -\boldsymbol{D}_i$. The $\boldsymbol{D}_i$ is a column matrix whose elements are given by $D_i = \chi_i^0 - \chi_1^0; \quad i \neq 1$ and $D_1 = 0$ assuming that at equilibrium, Eq. (14) is zero; else, $D_1 = -Q_{TOT}$. The $\boldsymbol{Q}_i = \{Q_i\}$ is a column matrix charge values to be determined. The $\boldsymbol{C}_{ij}$ is a $N \times N$ matrix with elements as $C_{ij} = J_{ij} - J_{1j}; \quad i \neq 1$ and $C_{1j} = 1$; $J_{ij} = J_{ij}^{EC}\left(\{r_{ij}\},\{k\}\right); i \neq j$, else $J_{ij} = J_{ii}^{0EC} = j_{ii}^{0} + J_{ii}^{EC}(\{r_{ii}\},\{k\})$.

Chapter 5

Model Implementation and Validation

5.1 Computer Implementation and Validation

First, partial atomic charges on different metal-organic framework compounds were computed through a Python-based program in Python, v.3.6. The calculations were based on the EQeq developed by Snurr and co-workers [162]. Input parameters in the Python source codes include the Ewald splitting parameter (zeta) in inverse Angstrom, atomic electronegativity (Chi) in eV, atomic chemical hardness (eta) in eV, and the global dielectric constant ϵ_r. Figure 5.1 shows the partial charges on atoms of the MOF (Metal Organic Frameworks) compounds computed with our Python program compared to EQEq [162] results. The diagonal line shows the bisector (charge from our Python program = EQeq charge). The average absolute difference ($AAD = \sum_i \left|Q_i^{predicted} - Q_i^{ref}\right|/N$) between our prediction and the EQeq results shows a similar accuracy as listed in Table B.1 of appendix B. The results, which are in good agreement with Snurr and co-workers demonstrate the validity of our Python program.

QEqLR is carefully implemented by editing the validated source code based on the model development equations and expressions contained in this work. Translated unit cells with a maximum of $L = 2$; implying $-2 \leq u = v = w \leq 2$; corresponding to $5 \times 5 \times 5$ periodic unit cells in the real and Fourier spaces were maintained as the charges were already converged for all tested systems. An example plot of the charge versus number of periodic unit cells is presented in appendix B.1. Traditional QEq employed an iterative technique to evaluate the dielectric constant ε_r. In this work, we maintained in all calculations a single global empirical dielectric parameter $\varepsilon_r = 1.67$, which was proposed in [162] and was verified in [163]. We set the Ewald splitting parameter to $\zeta = 0.15$ Å$^{-1} \approx \sqrt{\pi}/r_{cut}$ as defined in [161]. Using the same input geometries and charge equilibrium parameters to ensure easy comparison with QEq, we implemented a serial version of QEqLR in the 31Aug2021 version of LAMMPS. It was executed in the cluster of The Hong Kong Polytechnic University. We have ensured that the charges computed in the LAMMPS, and the Python implementations are in agreement. A R-squared (R^2) coefficient value of 1.0 was recorded between charges calculated with the two QEqLR implementations. The inset *b* in Figure 5.1 compares the charge values on MOF

compounds computed via Python and LAMMPS QEqLR implementations. QEqLR is more expensive than simple QEq, but the advantage is that it does respect the long-range character of the interactions between particles. Runtimes to obtain charges is shown in Figure B.2 of appendix B.

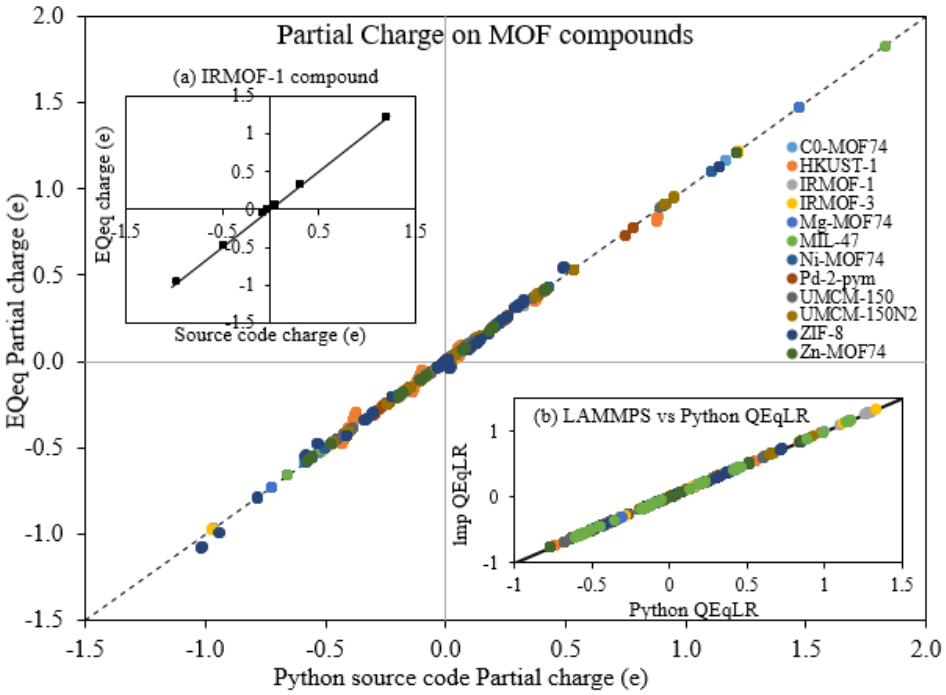

Figure 5. 1: Partial charge on metal-organic frameworks (MOF) computed with our source code compared against Wilmer *et al* [162]. The insets: (a) IRMOF-1 compound indicating source code perfect agreement with Wilmer. (b) Charge by LAMMPS versus Python QEqLR implementations.

How good is the choice of the Ewald parameter? It is good enough to produce reasonable and similar charges as QEq for all tested systems shown in Table 5.1 with a slight improvement. However, this setting does not guarantee that it is a universal parameter for the reproduction of QM charges for all materials because the Ewald splitting parameter is system dependent and characterizes the shape of the Gaussian charge distribution around the core of an atom. Therefore, we set the Ewald splitting parameter by trial-and-error to produce charges in an improved agreement with grid-based Bader charges than QEq. The choice of the Ewald parameter is further discussed in appendix B.2.

5.2 Charges with and without Long-range inclusion

We investigate the effect of the inclusion of long-range effect in the calculation of partial charges by comparing charges estimated with and without QEqLR against the *ab initio* method. On this note, we run a single-point molecular dynamics calculation for different molecules with

the conventional QEq as implemented for ReaxFF force field models in LAMMPS. We chose these molecules based on the availability of input data and quantum mechanical (QM) or experimentally (expt.) derived charges so we could benchmark the results. The boundaries of the simulation cells were periodic for all the geometrical structures, and the electronegativity, hardness, and shielding parameters were from various ReaxFF pair interaction potential files (refs in Table 5.1). Table 5.1 shows atomic partial charges for the molecules computed with and without long-range effects compared against those of *ab initio* methods. Neither QEq nor QEqLR predicted charges as the QM or experiment. However, they have a strong correlation with results from the *ab initio* methods as indicated in the R-squared (R^2) correlation value of QEq (QEqLR) = 0.9694 (0.9792) for hydroperoxyl-methanol (CH4O3). Also, a closer look at the results shows QEqLR performs much better than the QEq.

Table 5. 1: Comparison of *ab initio*, QEq, and QEQLR charges, and average of the absolute difference between QEq and QEqLR charges, and between each of QEq and QEQLR with *ab initio*.

Molecule	atom	*ab initio* method	QEq	QEqLR	$AAD_{QEqLR-QEq}$	AAD_{QEq}	AAD_{QEqLR}	QEq Parameter
SiO_2	Si	1.355[a]	1.259	1.301	0.028	0.063	0.035	[164]
	O	-0.677	-0.630	-0.651				
NaCl	Na	0.792[b]	0.812	0.811	0.001	0.020	0.019	[145]
	Cl	-0.792	-0.812	-0.811				
NH_3	N	-0.801[b]	-0.858	-0.838	0.010	0.029	0.012	[165]
	H	0.267	0.286	0.279				
CH_4O_3	C	0.170[c]	0.189	0.169	0.011	0.048	0.039	[166]
	O	-0.230	-0.204	-0.219				
	O	-0.380	-0.420	-0.416				
	O	-0.290	-0.326	-0.331				
	H	0.100	0.021	0.042				
	H	0.120	0.082	0.099				
	H	0.270	0.334	0.329				
	H	0.240	0.324	0.326				
H_2O	H	0.325[b]	0.301	0.326	0.033	0.032	0.001	[167]
	O	-0.650	-0.602	-0.652				
CH_4	C	-0.600[b]	-0.483	-0.561	0.031	0.047	0.016	[165]
	H	0.150	0.121	0.140				
HF	H	0.415[b]	0.405	0.421	0.016	0.010	0.006	[168]
	F	-0.415	-0.405	-0.421				
LiH	Li	0.768[b]	0.719	0.787	0.068	0.049	0.019	[168]
	H	-0.768	-0.719	-0.787				

DFT determined charge from [161] [a], experimentally determined charges taken from [29] [b], and Mullikan charge through quantum mechanical (6-31G**/B3LYP) method from [169] [c].

Column 6 of Table 5.1 shows the average absolute difference (AAD) between QEqLR and QEq results. The small difference is accredited to the deployment of the Ewald summation for

long-range Coulomb description of the atomic interactions. The observations from these test systems are that charges with and without long-range inclusion in the Coulombs interaction compare very well with the experiment. Comparison of Columns 7 and 8 of Table 5.1, which are the corresponding average absolute difference between QEq and QEqLR with *ab initio* charges, shows a slight improvement of QEqLR in the description of atomic interaction for charge equilibration. From the AADs (Average of the Absolute Difference) against QM/expt, the two methods gave almost equal charge values except for small improvements by QEqLR. This agreement is not surprising because the atoms are within the short-distance cut-off and all Coulomb electrostatic interactions between the particles are well accounted for in both methods. We anticipate more significant improvements in large systems.

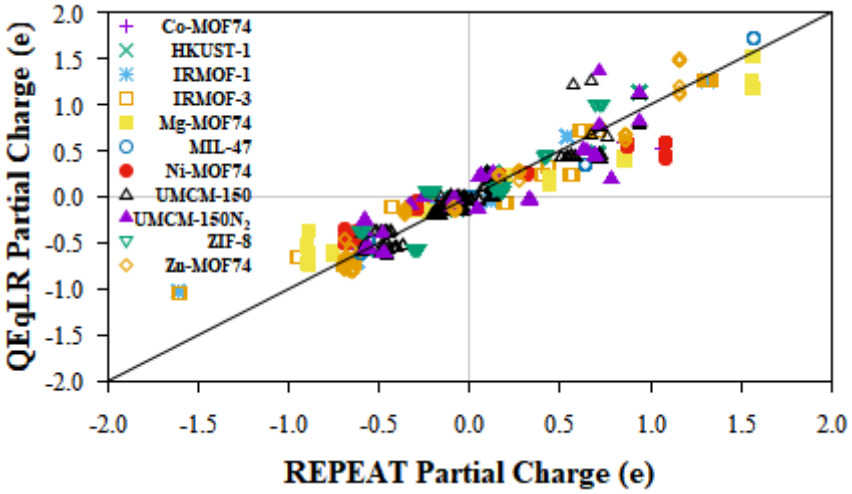

Figure 5. 2: QEqLR partial charges evaluated using $\zeta = 0.15$ Å^{-1} versus REPEAT (repeating electrostatic potential extracted atomic) charges on MOFs (Metal Organic Frameworks). REPEAT charges are taken from [162] supplementary information.

We applied the QEqLR method to compute charges for a diverse set of complex structures. We take atomic geometry data for 11 MOFs compounds with the associated REPEAT [161] charges made available in the Supporting Information of [21]. Figure 5.2 compares the QEqLR atomic partial charges with the REPEAT charges. Figure 5.3 shows identified atoms of IRMOF-1 MOF compound containing C, H, O, and Zn atoms with charge evaluated with QEq, QEqLR, and REPEAT methods labeled next to the elements. In Table 5.2, we show the performance of QEqLR and QEq as implemented in the LAMMPS simulator package with REPEAT charges. Then with the significant difference of the QEq charges from the reference charges, we conclude that the QEq implemented in LAMMPS is inadequate in predicting the partial atomic charge in these MOF compounds. The R-squared coefficient in Table 5.2 shows that it poorly reproduced the REPEAT charges. These coefficients being far from unity indicate

that the agreement between QEq and REPEAT is not as good as those for QEqLR. In fact, QEqLR performed well for the MOF compounds. It is not surprising that QEq failed since these materials are complex and periodic so that short-range Coulomb could not represent the electrostatic potential of the interacting atoms. This indicates that without long-range Coulomb interaction in the charge equilibration model, the atom charges are estimated poorly for some sets of complex systems. More surprisingly, we observe a large discrepancy in the polarity of the charge values with some being unphysical.

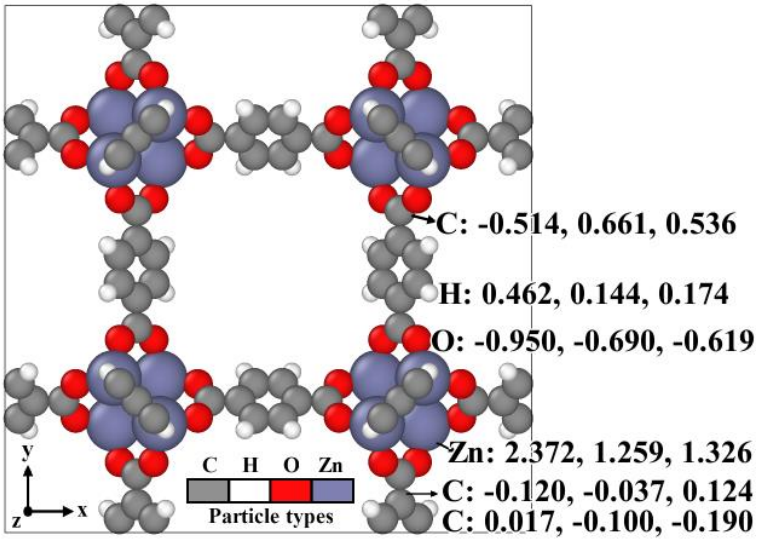

Figure 5. 3: Top view of IRMOF-1 metal-organic framework showing unique atomic charges with QEq, QEqLR, and REPEAT methods, respectively. The grey outline marks out a unit cell.

The QEq and QEqLR charge values for MIL-74 compound are available in Table B.4 of appendix B, alongside the REPEAT charge from [162]. The difference in the results confirms that short-distance treatment of Coulomb electrostatic potential in the QEq method does not agree with the long-range behavior of Coulomb interaction. Therefore, these results affirm that the addition of long-range Coulomb electrostatics interaction could better account for the Coulomb influence of nearest-neighbor atoms and suppress cut-off effects. We study in subsection 5.4 the long-range Coulomb under external potential difference. The outcome shows that the long-range interaction permits particles to experience forces from other particles at larger separations beyond a small cut-off.

Table 5. 2: Average of the Absolute Difference (AAD) of the QEqLR and QEq from the REPEAT charges provided in the Supporting Information of [162] for the MOFs.

Compound	Metal	Atoms/ unit cell	R^2 coefficient		AAD (e)		QEq parameter
			QEqLR	QEq	QEqLR	QEq	
Co-MOF74	Co	162	0.946	0.154	0.199	0.473	[164]
HKUST-1	Cu	624	0.941	0.549	0.088	0.284	[170]
IRMOF-1	Zn	424	0.954	0.647	0.091	0.391	[171]
IRMOF-3	Zn	472	0.929	0.040	0.125	2.059	[172]
Mg-MOF74	Mg	162	0.956	0.056	0.172	0.908	[170]
MIL-47	V	72	0.958	0.524	0.078	0.311	[166]
Ni-MOF74	Ni	162	0.964	0.002	0.194	1.021	[172]
UMCM-150	Cu	354	0.913	0.214	0.089	0.467	[170]
UMCM-150N_2	Cu	330	0.765	0.177	0.180	0.510	[170]
ZIF-8	Zn	276	0.720	0.161	0.165	0.801	[171]
Zn-MOF74	Zn	162	0.961	0.190	0.119	0.862	[171]

5.3 Application to Solid-State Materials

In this section, we applied the present method for partial atomic charges on some solid electrolyte materials used often in memory and energy storage applications. The materials were selected based on the availability of ReaxFF force-field files, and the optimized QEq parameters (refs in Table 5.3) for the constituent atoms of each material were from those force-field files. We did not combine these parameter sets for a given system from different ReaxFF force field files. The structures studied and the associated Ewald splitting parameter $zeta$ (ζ) are given in Table 5.3. We used a plane wave basis set expanded within a $500\ eV$ kinetic energy cut-off; and a Monkhorst-Pack k-point mesh method alongside a projector-augmented wave pseudopotential for electron-ion-core interaction and a generalized gradient approximation of Perdew, Burke, and Ernzerhof (PBE) [173] for electron exchange-correlation energy and run DFT calculations with Vienna ab initio simulation package (VASP) [174]. Then, compute the partial charges according to a grid-based Bader [175], [176] charge method since it is the most widely used charge assigning method for dense solid materials.

Like in Table 5.1, the results (though not plotted) are roughly equal with or without long-range Coulomb, but none of the methods predict charges as the DFT. That perhaps means that Eq. (3.24) or the parameterization therein could not represent the charge distribution of the Bader charge method. And may need to be reparametrized to benchmark against Bader charges. With the long-range Coulomb, the Ewald splitting parameter controls the spread of the charge

distribution. So, no need for rigorous optimization; adjusting only the Ewald parameter creates a good matching of the Bader charge distribution. Such a setting was done on the exponent of the Slater-type [177] orbital in the past to obtain improved charges in quantum mechanical *ab initio* calculations. As Figure 5.4 summarizes the charge results with/without long-range Coulomb for the various materials against the Bader charge values, Table 5.3 presents the performance similarity between QEq and QEqLR charges as the average absolute difference (AAD) from the Bader charges. The yellow diagonal line indicates the bisector $Q^{Predicted} = Q^{Bader}$, which shows that QEqLR is in better agreement than the LAMMPS' implemented QEq. It shows the flexibility in the Ewald splitting parameter, which we scanned through trial and error to obtain reasonable charges in best agreement with the Bader charge. We are unfamiliar with any existing functional estimator of the Ewald splitting parameter that focuses on charge accuracy**.** It is good to note that the default setting $\sqrt{\boldsymbol{\pi}}/\boldsymbol{r}_{\mathbf{cut}}$ yields roughly the same results as QEq on these systems. See additional notes in section appendix B.2**.**

Table 5. 3: Average absolute difference of QEq and QEqLR method charges (e) based on Bader charge calculations and the Ewald splitting parameter set for various solid-state material with the Material Project IDs given**.**

Material	Materials structure ID	Atoms per unit cell	Zeta, ζ ($Å^{-1}$)	AAD (e)		QEq parameters
				QEq	QEqLR	
$Ca_3Al_2O_6$	mp-640266	33	0.241	0.596	0.136	[178]
Cu_2S	mp-618991	12	0.470	0.449	0.046	[164]
CuO	mp-510752	16	0.320	0.501	0.057	[164]
$CuSiO_3$	mp-16053	10	0.300	1.045	0.179	[164]
GeS_2	mp-1071032	6	0.420	0.529	0.099	[170]
Li_3ClO	mp-985585	5	0.150	0.281	0.276	[179]
Li_3PS_4	mp-985583	32	0.410	0.456	0.052	[179]
$LiAlH_4$	mp-1192061	24	0.400	0.674	0.052	[180]
$LiAlO_2$	mp-3427	16	0.250	0.638	0.097	[180]
$LiBH_4$	mp-1192133	24	0.300	0.862	0.108	[181]
$LiTi_2(PO_4)_3$	mp-773843	72	0.213	0.831	0.086	[182]
$LiTiPO_5$	mp-6668	32	0.218	0.684	0.063	[182]
Na_3AlH_6	mp-568950	80	0.400	0.587	0.057	[178]
Na_3PS_4	mp-28782	16	0.150	0.217	0.217	[183]
NiO_2	mvc-12901	24	0.050	0.399	0.033	[184]
SiO_2	mp-554089	12	0.297	1.297	0.005	[164]
SiO_2	mp-558947	144	0.297	1.327	0.042	[164]
$SrAlO_3$	mp-978862	5	0.150	0.284	0.157	[178]
TiO_2	mp-2657	6	0.215	0.405	0.006	[145]
VO_2	mp-19094	6	0.188	0.398	0.020	[166]
ZnO	mp-1093993	8	0.170	0.226	0.007	[171]
ZrO_2	mp-776404	24	0.350	1.110	0.081	[164]

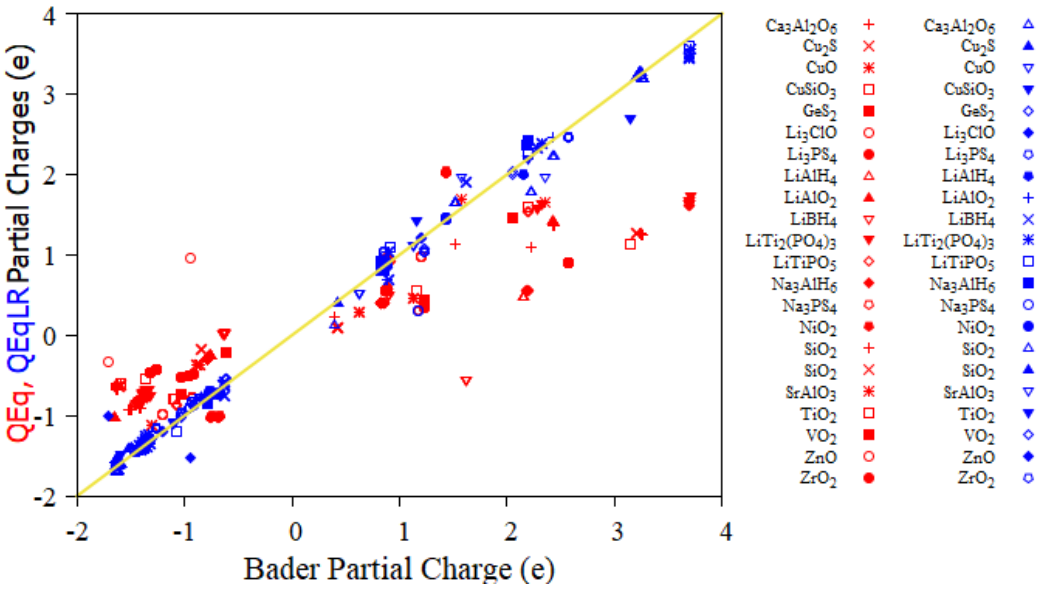

Figure 5. 4: Comparison of QEq (red) and QEqLR (blue) partial charges with Bader charges for the solid-electrolyte materials contained in Table 5.3.

5.4 Model Parallel Plates Capacitor Configuration under Applied Potential.

How much effect does the long-range inclusion of the Coulomb interaction potential have on partial atomic charge distribution? We illustrate the amount of the influence by carrying out simulations under an applied electrostatic potential difference Φ_0. The potential difference is applied by perturbing the atomic electronegativity χ_0 of the atoms in one of the neutral electrodes by changing the electrode potential [8], [152] from χ_0 to $\chi_0 + \Phi_0$ and the other electrode to $\chi_0 - \Phi_0$. That led to a net electrochemical potential difference of $2\Phi_0$ across the electrodes. Figure 5a is a snapshot of the system configuration, a $21.6 \times 21.6 \times 43.2$ Å^3 orthogonal box periodic in the x and y directions but fixed in z. We used a large box with empty spaces above and below the top and bottom electrodes in the z-direction. The dimension of the vacant spaces is greater than or equal to the x and y dimensions. Putting vacuums at the ends of the electrodes permits the application of the 3D Ewald sum to the slab conditions [102]. An alternative approach would be to employ the full two-dimensional (2D [185]) Ewald sum. The thickness of each electrode along z is 10.8 Å, while the gap or vacuum (dielectric thickness) between the inner surfaces of the top electrode (TE) and the bottom electrode (BE (Bottom Electrode)) equals $(3.6 + 2i)$ Å; $i \in [0,18]$ equals the simulation step. Each electrode consists of six tightly packed atomic layers of Cu atoms with the [111] crystallographic face exposed to each other along the z-axis. The distance between two consecutive layers in the bottom or top electrode is 1.8 Å. BL{j} and TL{j} are corresponding sets of layers in the bottom

and top electrodes, while j counts the layers in each electrode from the outer end towards the innermost surface. The electrodes together contain 436 atoms. Overall, the atoms on each layer for every separation (dielectric thickness) between BE and TE, we obtained the net charge distribution and the total charge on each electrode as tabulated in Table B.2 (a & b) of appendix B. Then, analyze (focusing on one of the electrodes since the other produces reverse results) the charge evolution across the layers for the two models as the vacuum gap between the electrodes increases.

At first, we checked how the initial charge state (neutral or charged) of the electrodes affected the charge distributions and observed it has no effects provided the sum of the starting charges is zero. That was as expected since the matrix is a set of linear equations; it also shows the correctness of our implementation.

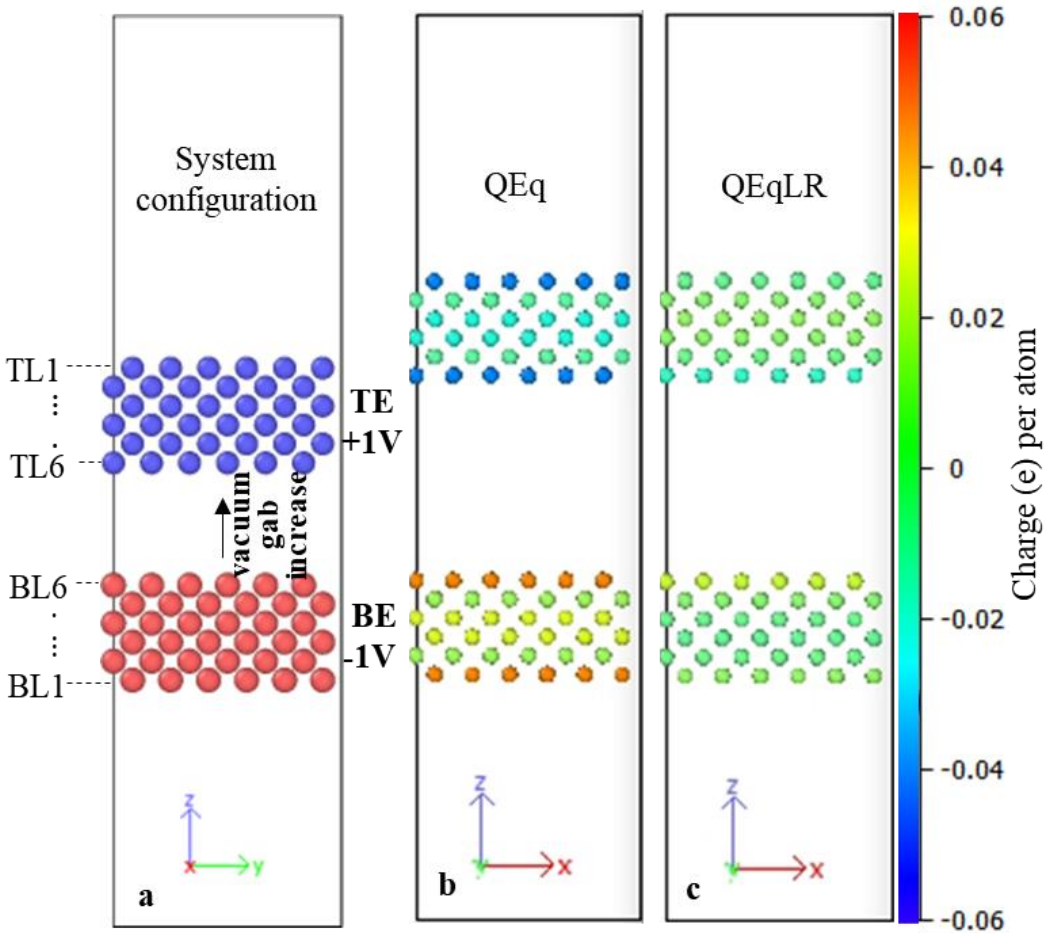

Figure 5. 5: Illustrative diagram of (a) the parallel plate capacitor configuration with top electrode (TE) at $+1\ V$ and the bottom electrode (BE) at $-1\ V$; and the charge distribution on the atomic layers over separation between electrodes for (b) QEq and (c) QEQLR.

On the QEq, Figure 5.6 (reds) are the net charges on each layer of the electrodes against the separation (dielectric thickness) between the inner surfaces of the bottom and top

electrodes. The plot shows the charge distributions only fluctuate below the 10 Å cut-offs, above which the charge distribution becomes uniform (constant). As expected, charge distributions are higher on the closest layers (BL6 and TL6) to the vacuum than on any other layer. Observing Figure 5b clearly, we could see the existence of pairwise charge parity within each electrode and of opposite polarity with corresponding layers of the opposite electrode. For example, around 9.6 Å separation, each of the pairs (BL1, BL6), (BL2, BL5), and (BL3, BL4) converged to equal positive charges in corresponding absolute value parity with the negative charge distributions on (TL1, TL6), (TL2, TL5) and (TL3, TL4) of the positive electrode. With LR Coulomb, we recorded charge absolute value parity among corresponding layers of the electrodes but not convergence to equal charge values among layers of an electrode. These data are available in Tables B.2 & B.3 of appendix B.

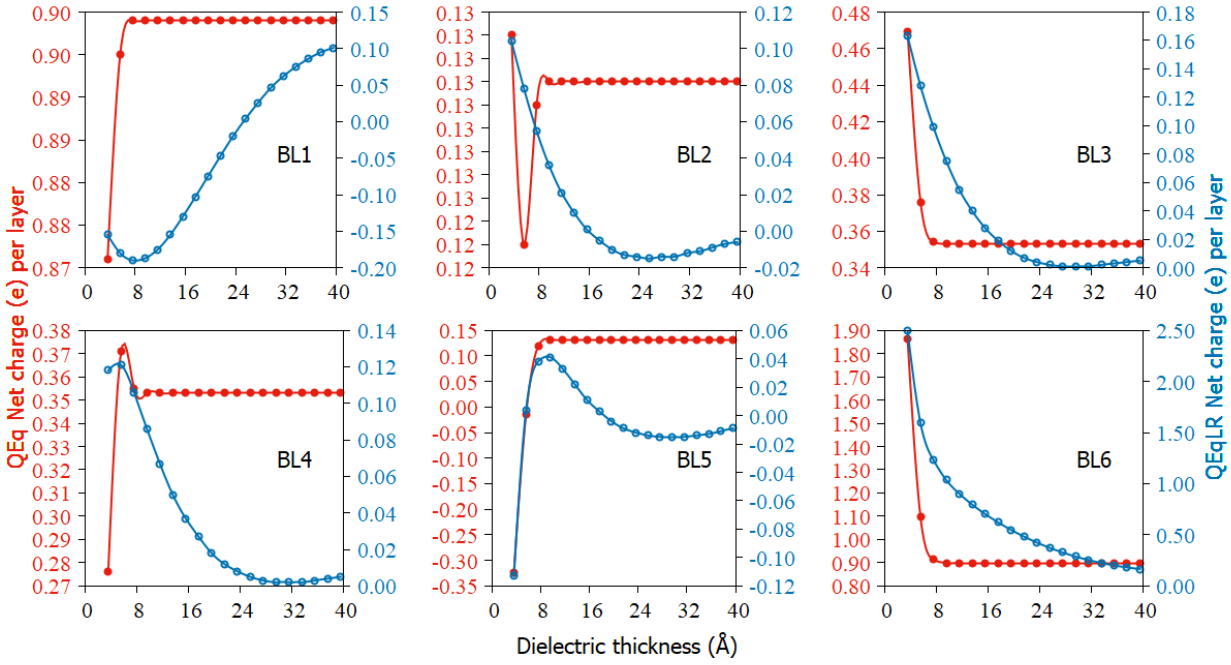

Figure 5. 6: Comparison of QEq (red) and QEqLR (blue) net charge distributions on the layers of the bottom electrode versus the dielectric thickness. The top electrode is vertically opposite of these plots.

With the QEqLR, Figure 5.6 (blue) shows pronounced and continuous charge fluctuations from layer to layer as the separation increased. Like in QEq and as expected, the most charged are the innermost layers. The charge distributions on the innermost layer and on each electrode decay exponentially as separation between the electrodes is increased. The fluctuation of charges on the innermost layer extends to other layers but diminished remarkably as the separation between electrodes increases. On the contrary, QEq did not show these significant charge fluctuations, instead has a constant (uniform) charge distribution after the cutoff. While

visualizing the atomic trajectory in OVITO [186] and evident in Figure 5.6, QEqLR shows clearer charge fluctuations on individual layers against increasing gaps than the short-range model. Figure 5.7 (blue & red) captures the net charge distribution on the electrodes with and without long-range Coulomb; the blue curve exhibits the long-range Coulomb effects on the net charge distributions than the red curves. Unfortunately, based on novelty of research investigations, coupled with differing system configurations, and various conditions and factors of interest for carrying out research, there is no matching data in the literature to quantitatively compare these results with; however, we qualitatively compared the decay pattern of the total surface charge as a function of increasing separation between the electrodes with those given in [187] – [189]. The pattern of the surface charge distributions as a function separation between the electrodes in QEqLR model toke after the trends observed on an electrode in a triboelectric nanogenerator [187], near the cathode surface in surface flashover model [188], and on the electrodes in an integral equation theory of an electric double layer device [189]. On the contrary, without the long-range Coulomb inclusion (i.e., with QEq model), the surface charge distribution drops sharply around the cutoff and beyond the cutoff, the charge distribution remains a constant; suggesting that the electrodes even when they are well separated will feel a force (Figure 5.8) from each other due to the charges they possess. Also, Figure 5.7 displays the total charge evolution on the bottom electrode under the applied field for QEqLR and QEq at default and increased QEq cutoff distance. We record some findings; firstly, increasing the cutoff to $\leq 0.5 * \min(lx, ly)$ (avoiding the minimum image problem) of the periodic directions does not guarantee the charge distribution to decay with increasing separation; it maintains a constant charge from around the cutoff and reduces the charge magnitude. It also does not display the decaying pattern shown in the theoretical and experimental surface charge density data of [187] – [189]. The overall net electrode charge obtained from the test of increasing the QEq cutoff may mean that nearest neighbor non-bonded atoms have an excessively influential contribution to the energy of a particle, for which interactions are computed. Such influence could lead to instability and poor description of molecular structures [190].

Figure 5.8 compares the Coulomb forces on the negative electrode as calculated using the charges from QEq and QEqLR models. CS and CL denote that the Coulomb force functions were subjected to short- and long-distance interactions, respectively. The orange curve exhibits the behavior of the Coulomb force between two charge bodes with respect to increased separation. While the purple as well the blue curve indicates the force goes to zero at the 10 Å

cutoff, a bigger problem is witnessed on the QEq CL model (green curve), which shows that high and constant force is experienced by the electrode even at larger separation between them. Conclusively, the forces do not remain constant as the separation between the electrodes is increased, and the long-range Coulomb approach (QEqLR CL) gives better estimate of the charges and forces on the electrodes.

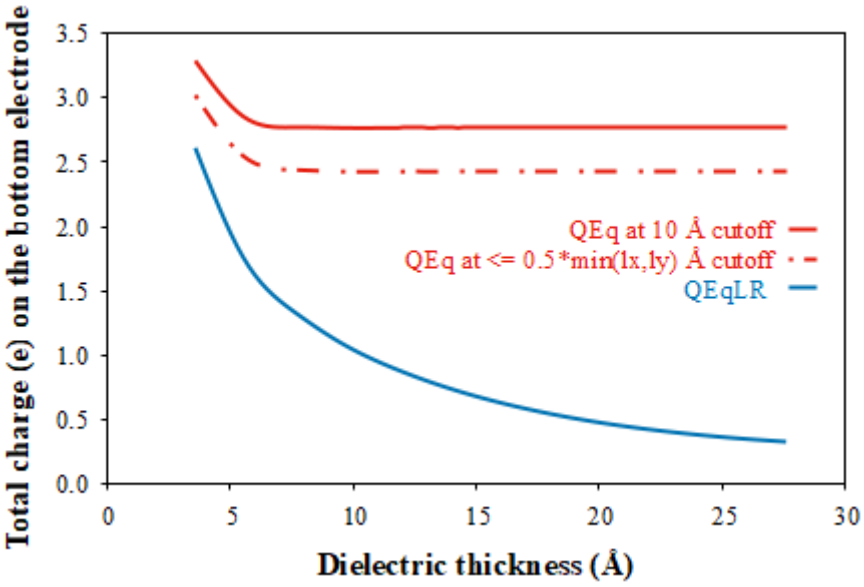

Figure 5. 7: Comparison of the QEq (red) and QEqLR (blue) total charge on the negative electrode. Their decaying pattern is compared against those of [187] – [189].

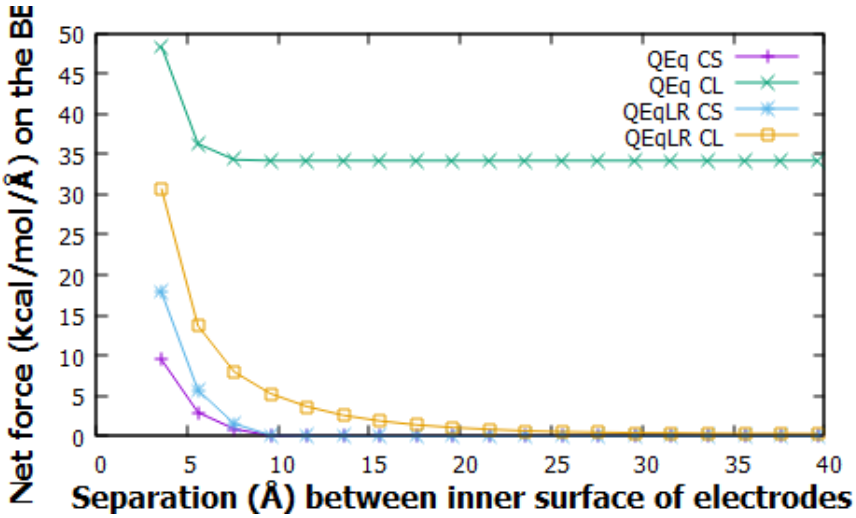

Figure 5. 8: Comparison of Coulomb forces on the negative electrode as computed using the charges from QEq and QEqLR models and Coulomb potentials at 10 Å cutoff (CS) and long-range order (CL).

Concisely, including long-range Coulomb confirms the Ewald sum is key to describing Coulomb electrostatic interaction. We could assert that the long-range inclusion eliminates

some imbalances (such as an atom not seeing compensating charge distribution) and surface artifacts imposed by a cutoff in charge distribution on the layers of the electrodes.

We have looked at the charge evolution with the inclusion of LR and applied electric field on a parallel plate capacitor of the bulk electrode and recorded some interesting effects. These effects also reflect on the forces on each layer of the electrodes. The electrode forces and charges decay towards zero with the long-range inclusion, without which we recorded constant non-zero and high force values in Figure5. 8.

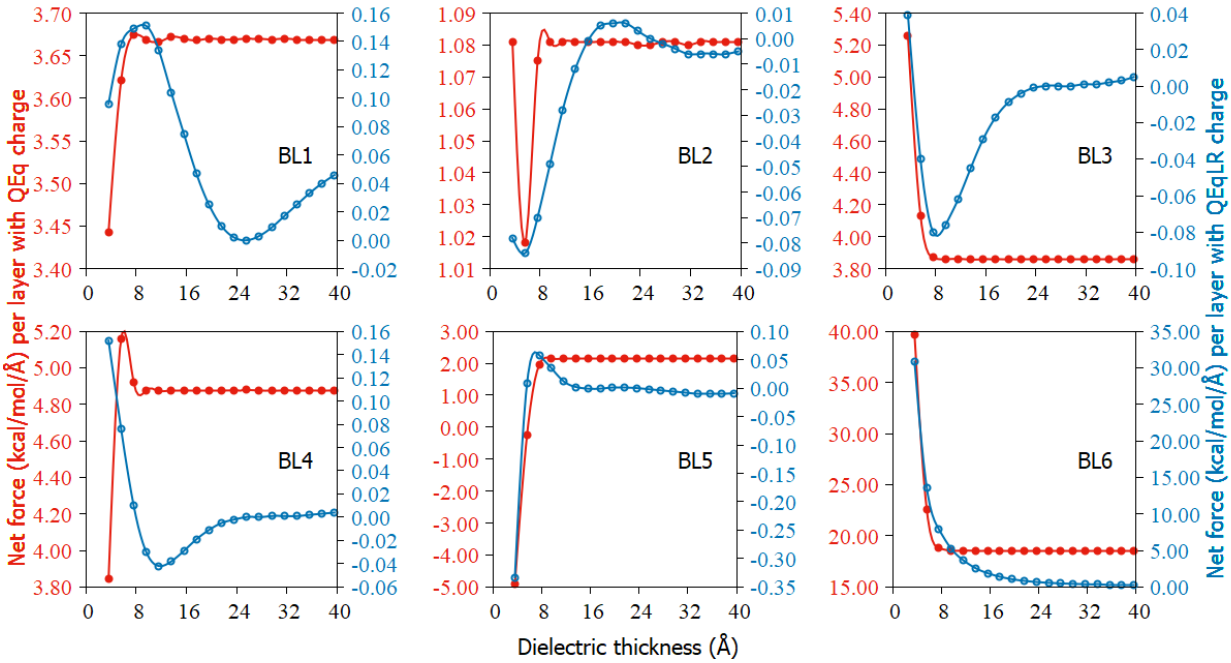

Figure 5. 9: Net forces resulting from QEq (red) and QEqLR (blue) charges on the layers of the bottom electrode as a function of the dielectric thickness. The top electrode is vertically opposite of these plots.

Chapter 6

Water in between Graphene Electrodes

6.1 Introduction

In this section, we apply the QEqLR method to describe and evaluate dynamical partial atomic charges in our molecular dynamics (MD) simulations of graphene-water electrochemical systems at different graphene electrode separations and applied potentials. Graphene-water systems have received tremendous attention in recent years owing to the tunable electrical properties [191] of graphene coupled with its sensitivity to the surrounding environment, dynamical wettability [192], and the relevance of water to everyday natural life, including cases in ionic media and protein cavities [193], fuel-cell membranes [194], etc. The unique properties [195] of graphene and the polarizability of water under applied electrical stress render these electrochemical systems important for scientific, industrial, and technological applications. Examples of applications include seawater desalination [196], electric double-layer devices (EDL) [7], and supercapacitors [197].

Interfacial water/electrode studies started in a drastically unrealistic form that models electrodes as smooth-hard walls with fixed uniform charge distributions without direct simulation of water molecules [198], [199]. Other setbacks witnessed in the past despite significant efforts occurred in modelling the bulk electrolyte and interfacial boundaries between liquid electrolyte/electrodes is the experimental and voltammetry [200] difficulty in taking measurements about interfacial changes at the atomic level. This problem was improved with the advent of atomistic MD simulation. However, the challenge of accounting for a uniform external potential difference across the electrodes in an electrochemical system persists; then forced researchers to maintain the old approach of enforcing constant charge densities of opposite polarities on the electrodes. A practice that failed due to unphysical surges in temperature and efforts toward resolving the problem led to the introduction of fluctuating charge methods [29], [130], [150] – [153], which, researchers applied in studying graphene/water [86], copper/water [201], platinum/water [202] systems, among others. Toward improving the approach, Siepmann and Sprik [203] proposed using a Gaussian charge function to determine the charge values that will fix the potential difference to a desired value. A more recent practice [8], [201], [202], [204] in MD simulation involves perturbing the atomic

electronegativity χ_0 by changing the electrode potential of the atoms in one of the electrodes from χ_0 to $\chi_0 + \Phi_0/2$ and the other from χ_0 to $\chi_0 - \Phi_0/2$. That would lead to a net electrochemical potential difference of Φ_0 volt across the electrodes and makes it easier to fix the external potential to desired values.

The functioning of electrochemical devices (especially capacitors, EDLs, and supercapacitors) is rooted in anions and cations adsorption in solvated media during the interfacial chemical interaction between electrodes/electrolyte and controlled by the nano-porosity/pore-size (see [82]) of the electrode and the local interfacial structure of the liquid electrolyte [205], [206]. In addition to the positive influence of fixing the potential based on the electrodes' nano-porosity/pore size, Li, and co-workers [207] attributed structural changes to the application of an external potential to originate from the substantial difference in interfacial charge distribution leading to differential capacitance. Two independent authors (Limmer [208] and Ma and co-workers [209]) respectively linked differential capacitance in EDL capacitors to charge density ordering and charge-driven lateral structural evolution. These suggest that charge evaluation and the methods employed for the charge computation may influence/affect the characteristics of these devices under MD simulation. Among several molecular dynamics studies reported on metal/graphene and water interface reactions, the foci were on capacitance measurement [86], [210], interfacial structure organization and orientation of the electrolyte near the electrodes [192], [211] – [214], and capacitive behavior of the device [207]. However, the charge computation at the interface and bulk regions of the electrodes/electrolytes and the charge effect, if any, on the properties and behaviors of these devices received little/no attention.

In this MD simulation, we used a reactive force field (ReaxFF) [215] to describe the interaction between atoms. ReaxFF applies a bond-order-dependent classical interaction potential, in which the total energy is the sum of partial energy contributions from bonded (covalent) and non-bonded (Van der Waals and Coulombs) interaction terms. The non-bond interactions are distance-corrected using a potential function called the shielding interaction function [127], [132]. For the covalent counterpart, the bond order determines the chemical environment of the atoms and controls the bond strength of the materials. Therefore, the bond order is a function of the bond distance between two particles, which changes as the local environment surrounding the atoms is continually updated at each MD step and this smoothly decays to zero as the separations between atoms increase. Details on ReaxFF are in [120]. In most development and application of ReaxFF, changing the local atomic environment also

requires an environment-dependent partial charge. The evaluation of the environment-dependent atom charges is attainable by coupling ReaxFF with the charge equilibration (QEq) technique developed by Goddard and Rappë [29]. These models (ReaxFF and QEq) enable applications to simulate devices composed of dissimilar materials [126], and they allow the description of interfaces and chemical reactions. However, the numerical implementation of QEq and ReaxFF models includes Coulomb interaction only up to a short-distance cutoff for computational speed. Ignoring long-range Coulomb interaction affects the ability to describe charge distribution and polarization effects and distorts the system structure and energy [30]. This is evident in solvated biological and biomolecular systems. For example, the cutoff sizes used in the Coulomb interactions strongly influence MD results on solvated polypeptides [190], in which the stability of the α-helix configuration of peptide conformation is a function of cutoff size. On the contrary, the application of the Ewald technique in describing Coulomb interactions conserved the helical character of the peptide conformation.

Based on the above backgrounds, we will attempt to gain insight into the charge evolution as a function of the separation between electrodes and applied potential on the electrodes using an environment-dependent charge model that includes long-range Coulomb interaction. We discuss the effect of long-range inclusion in partial atomic charge computation on the structural and electrostatic properties of the graphene/water capacitors at various separations and different applied potentials.

6.2 System Configuration and Computational Details

Structural configurations consisting of two parallel graphene layers (electrodes), each containing 28 fixed carbon atoms and a surface area of $7.77 \times 8.04\ \text{Å}^2$, were modeled in orthogonal supercells, which are periodic in x and y but fixed in z-directions with dimensions given as $7.77 \times 8.04 \times \left(17 + d_{sep}\right)\ \text{Å}^3$. The inter-electrode space is intercalated with water molecules to preserve the density of homogenous water fluid in each channel. Table 6.1 summarizes the size of the model configurations, which includes the separation d_{sep} (inter-electrode spacing) between electrodes and the number of water molecules in each set-up. Figure 6.1 shows a snapshot of the configuration at $d_{sep} = 25.00\ \text{Å}$ and with 8.5 Å vacuum space added above and below the positive and negative electrodes along the direction normal to the electrodes' surfaces. The vacuum spaces were to suppress periodicity along the z-direction so that the 3D Ewald technique could apply to the slab geometry or equivalently to the 2D periodic boundary condition. We run two similar MD simulations on each system at 0.0

volts with the large-scale atomic/molecular massively parallel simulator (LAMMPS) [37] at a time-step of 0.5 fs. Constant NVT conditions are maintained using a Nose-Hoover thermostat with a damping factor of 100 fs and a temperature of 300 K for a total of 250ps for accumulating statistics. Reactive force field (ReaxFF) [215] model was used to describe the interactions among atoms in the system configurations in which QEq evaluates the atomic charges. Our modified ReaxFF was hybridized with Ewald sum and used to describe the interactions among the atoms in the systems in which QEqLR computes the atomic charges. QEq and SRC interchangeably denote the former models (short-range Coulomb) in the plots while QEqLR and LRC identically stand for the latter models (long-range Coulomb). The simulations were repeated only for $d_{sep} = 25.00$ Å and at various potential differences: $\Phi_0 = 1.0$, 1.6, 2.0, 2.2 and 3.0 V applied following the earlier description.

Table 6. 1: Supercell parameters of model configuration and the number of water molecules in each cell. The model systems are tagged extra-small (XS), small (S), medium (M), extra-medium (XM), large (L), and extra-large (XL)

System tag	d_{sep} (Å)	nH_2O	Lz (Å)
XS	4.78	10	21.78
S	9.58	20	26.58
M	14.37	30	31.37
XM	20.12	42	37.12
L	25.00	52	42.00
XL	30.17	63	47.17

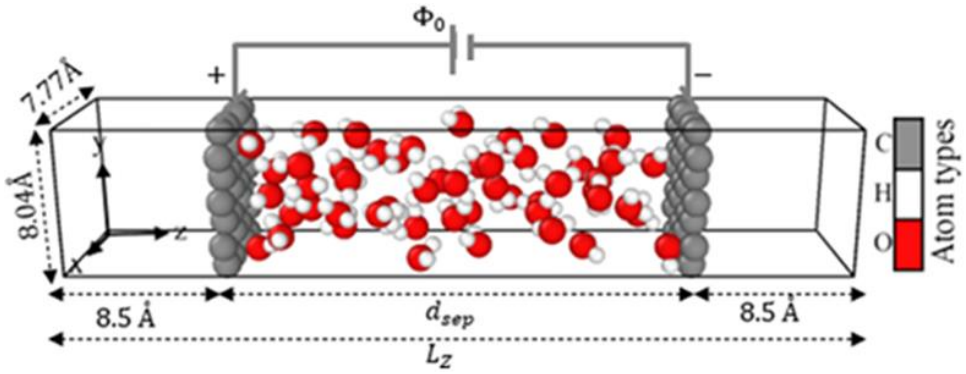

Figure 6. 1: Snapshot of the simulation cell with water intercalated between the graphene electrodes and vacuums left below and above the positive and negative electrodes to suppress periodicity in z-direction.

6.3 Density Distribution of Water in the electrodes channel

We computed the densities by binning the positions of the particles into rectangular slabs along the z-direction. Figure 6.2 compares the computed water densities from QEq and QEqLR based calculations. In all cases, water formed sharply defined peaks at the immediate interfacial

regions close to the graphene electrodes. The density modulations become narrower with the formation of more intermediate but diminishing strata as inter-electrode separation increases. The density modulations defined the interfacial layers or water stratifications. Those density strata are not only typical to graphene/water ([86], [216], [217]) systems, but also water intercalated between hard surfaces ([213], [218]). The intermediate peak formations at increasing separation indicate the water density oscillations, while the high interfacial densities suggest the preferential organization of water molecules near the graphene walls. The water oscillations are amplified at small (systems XS, S & M) separations (strong confinement) between electrodes and suppressed in the bulk region at large inter-electrode distances (systems (XM, L & XL) corresponding to weak confinement. We observe about a 2.5 Å exclusion gap from the surface of the electrodes in agreement with *ab* initio [216], [219] prediction on water behavior in contact with hydrophobic surfaces.

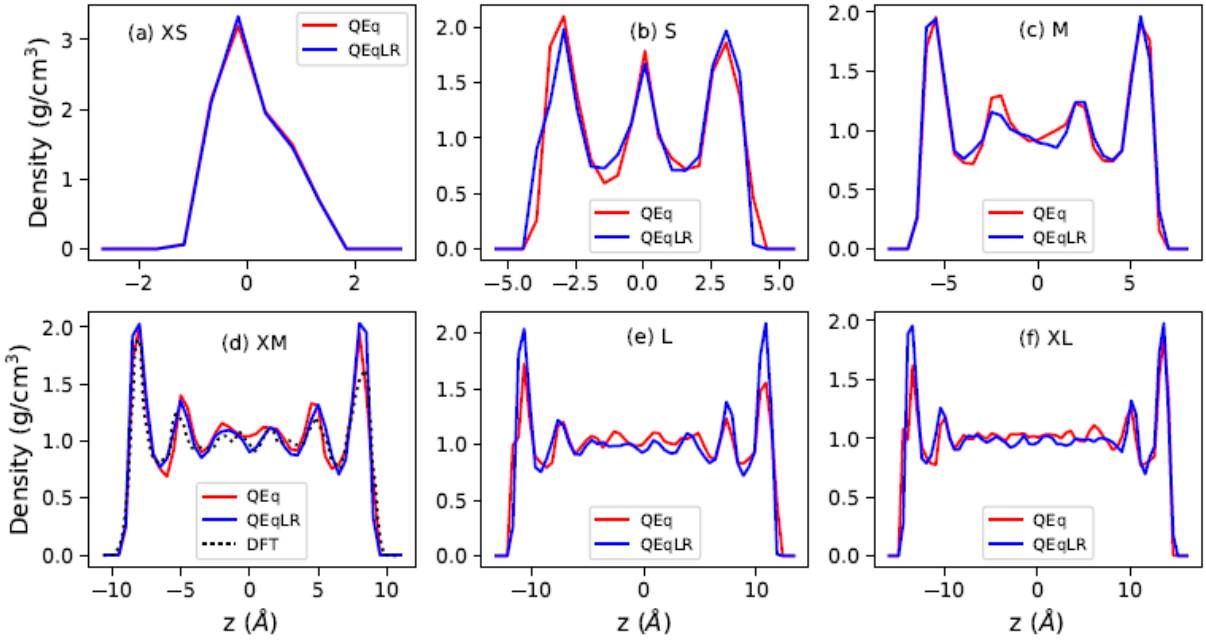

Figure 6. 2: Densities of water for MD results with QEq (red) and QEqLR (blue) at 0.0 V for all systems and symmetrized about $z = 0$ Å. MD results are compared with DFT (dotted black) [219] at XM.

With increased d_{sep} (Figure 6.2 d, e, & f) and beyond about 5 Å from the end of the exclusion thicknesses, the densities are more constant and is close to the bulk water density (1.0 g/cm3) in both models. These density plots are qualitatively similar and show symmetry along the normal to the electrode surfaces and relative to the center of the simulation box. However, a closer look and comparison with the DFT result (Figure 6.2d) and equivalent system in [219] reveals slight discrepancies. The QEq shows a performance lesser in agreement

with the DFT result than QEqLR. Although not too apparent, the amplitude of the water densities at the interfacial regions is higher with QEqLR than QEq and becomes more vivid at increasing separation between electrodes. Whereas at the intermediate lamella, the amplitudes of the QEq are a bit higher than those of QEqLR. Perhaps, these differences result from the interaction between the partial charge of the hydrogen and oxygen atoms of the water molecules and the fluctuating charges on the electrodes. We attribute these slight differences to the charge estimation method employed in each simulation since the two MD simulations are similar in all aspects apart from the QEqLR inclusion of long-range effect to the Coulomb atomic interaction description and QEq subjected the interactions to short-distance cutoff. Figure 6.3 compares the densities of the O and H atoms from the two models with *ab initio* MD results [216] for system L and at zero applied potential. With the long-range inclusion, the amplitudes of the density profiles are higher at the interface layers than without the long-range effects, whereas, at the intermediate layers, QEq shows a little higher density profile amplitude than QEqLR. This result suggests that water molecules are more pulled or oriented toward the graphene surfaces when LRC, which is a better match to the DFT, calculates the atomic charges

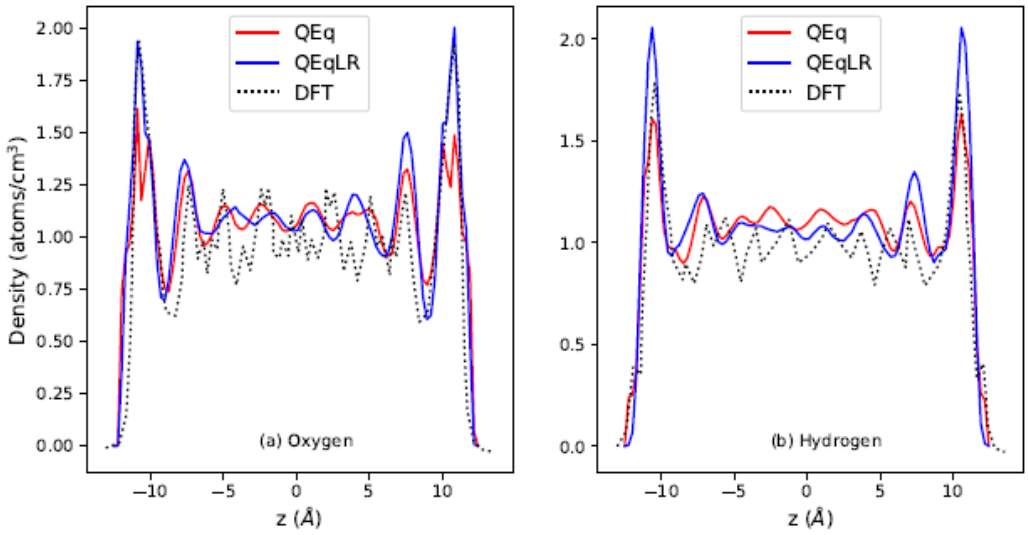

Figure 6. 3: Number densities of oxygen (a) and hydrogen (b) of water for MD results with QEq (red) and QEqLR (blue) compared with DFT (dotted black) [216] at 0.0 V and for system L symmetrized about $z = 0$ Å.

and describes interactions between atoms than when we employ SRC. Also, it is an indication that more structured solvation shells are close to the electrode surface using QEqLR instead of QEq, thereby elucidating consistency with the preferential water orientation around the hydrophobic graphene wall [219]. And conclusively, QEq predicts an under-structured solvation shell around the graphene surface. The similarity between the two models indicates the conservation of water properties with either of the models. Although a thorough inspection

of the plots shows that modulations with QEq are slightly higher, especially on the intermediate lamellas relative to those of QEqLR, it becomes more visible as the separation increases.

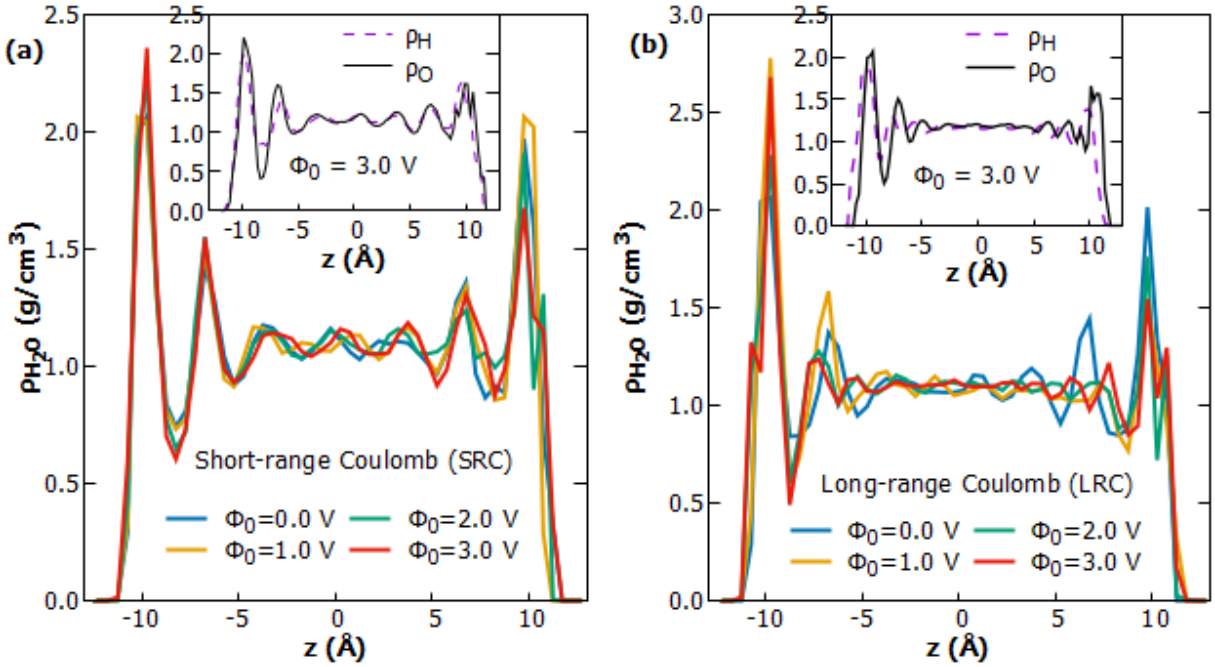

Figure 6. 4: Density profile for water without (a) and with (b) long-range Coulomb and at various external potential difference perturbations to the electrodes in the L system. The inset plots are the density profile for Oxygen (solid line) and Hydrogen (dashed line) at $\Phi_0 = 3$ V.

At zero applied voltage, the density distribution appears symmetric about the center of the simulation box, as seen in Figure 6.2. When a potential difference is applied between the electrodes, the density distributions lose symmetry, as illustrated in Figure 6.4. The Figure 6.4 describes the density profile distributions of water at different external voltages applied between the electrodes and predicts similar but slightly different results for the QEq (short-range Coulomb (SRC)) and QEqLR (long-range Coulomb (LRC)) methods. While in the QEqLR, the amplitudes of the peaks near the surface of the electrodes attenuate significantly and flatten around the center of the cell with increased voltage, a significant oscillation persists towards the center of the cell from the two electrodes in the QEq, suggesting that bulk-like water behavior is easily possible with LRC. The oxygen and hydrogen density profiles for water are shown at 3.0 V applied voltage as insets in Figure 6.4 to illustrate the relative difference between the attenuation of oscillations recorded in the two models. It also reveals the relative shift between the oxygen and hydrogen density distributions, which demonstrates the orientation of water molecules owing to the applied potential. It is observable from the inset plots in Figure 6.4 that this shift is conspicuous with the LRC in agreement with SPC/E

modelled water between platinum electrodes (see [218], [220]) of opposite polarity than the SRC.

6.4 Water Radial Distribution functions (RDF)

The RDF $g_{\alpha-\beta}(r)$ where α and β are atomic or molecular species in the system ($\alpha, \beta \in \{\mathrm{C}, \mathrm{H}, \mathrm{O}, \mathrm{H_2O}\}$), provides better insight into understanding the water structures and ordering of the water atoms near the graphene surfaces. The RDFs $g_{\mathrm{O-O}}(r)$ and $g_{\mathrm{O-H}}(r)$ predicted in the two sets of calculations are presented in Figures 6.5 & 6.6 and are in perfect similarity. The first peaks on $g_{\mathrm{O-H}}(r)$ are located at 0.95 Å for the O – H intra-atomic bonding, while the first peaks on $g_{\mathrm{O-O}}(r)$ and the second peaks on $g_{\mathrm{O-H}}(r)$ describing O – O and O – H intermolecular interactions and bond distances are located at 2.75 and 1.85, Å respectively. These results perfectly agree with the X-ray diffraction experiment [221], [222] and DFT results [223]. The performance agreement of the QEqLR results with QEq, DFT, and experiments indicates the preservation of the structural properties of water with the QEqLR charge computation model and an indication that the partial charge predicted for water atoms with both models are roughly the same and the structural properties of water are independent of the partial charge prediction model provided the same (or nearly the same) charges are predicted. In both simulations and across all systems studied at 0.0 V potential difference, we observed that increase in the inter-electrode separation does not significantly create changes in the locations of the peaks. Instead, it results in an appreciable reduction in the amplitudes and slightly narrower and flattened distributions at the surfaces and subsequent peaks, respectively. These outcomes suggestively imply that the introduction of long-range Coulomb in partial charge computations has little/no effect on the geometrical parameters of the water molecules at zero volts bias. We note that under non-zero potential difference, the radial distribution of the water molecules is invariant in terms of the positions of maximum and minimum peaks, as illustrated in Figure 6.6, implying that the potential difference did not change the water structures with either of the models. However, the applied voltages influenced the structural order/arrangement of the water molecules near the surface of the electrodes. The outcomes recorded here agree with those of [224] regarding the invariance of the positions and amplitudes of the peaks with an increasing potential difference. The RDF $\mathrm{g}_{\mathrm{O-H}}(r)$ and $\mathrm{g}_{\mathrm{O-O}}(r)$ of water atoms lying around the oxygen atoms in the first solvation shell are on display for various applied voltages in Figure 6.6, which unveils that though the locations of the extrema are unaffected by the increasing voltages, their amplitudes increase slightly with it. With the inclusion of LRC, there is a slight difference in

the amplitude of the peaks compared with SRC. For instance, in the $g_{O-O}(r)$ plot, the peaks' amplitude is slightly higher in the LRC than in SRC models, and they have differences of about 0.147 at 0.0 V and to about 0.03 at the other potentials. Therefore, the results here elucidate that the structural properties of water within the electrodes are described sufficiently with the short-range Coulomb. However, since it is not the structural exhibition of the solvent, and its densities that characterize and impact the device as a capacitor but rather the charge density distribution, we switch to analyzing the device based on charge distribution.

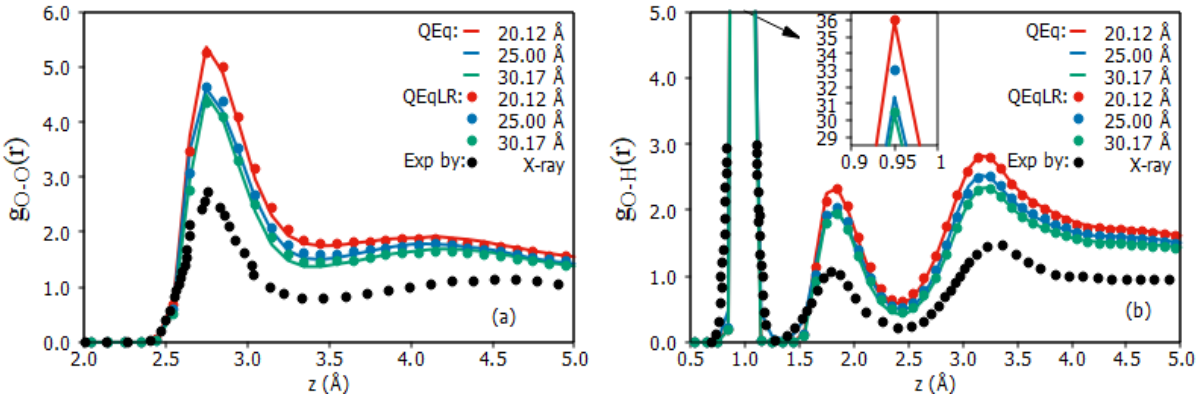

Figure 6. 5: Partial RDFs of water for (a) $g_{O-O}(r)$ and (b) $g_{O-H}(r)$ predicted at 300 K and 0.0 V. Distances accompanying the legends denote separation between electrodes. The black dots denote plots of data from X-ray diffraction experiment for $g_{O-O}(r)$ and joint X-ray/neutron diffraction experiments for $g_{O-H}(r)$ [221], [222]; QEq (QEqLR) = colored lines (colored dots).

6.5 Electrodes Under Applied Voltage but Zero Water-Intercalation

To investigate the performance of the graphene capacitor with and without long-range Coulomb interaction in QEqLR/ReaxFF and QEq/ReaxFF for L system at various applied voltages, and with water molecules intercalated between the electrodes first, we check how the electrodes respond to applied potential concerning charge accumulations. Emphatically before the simulation ran, the charge on each atom was zero. Table 6.2 shows the surface charge density on the electrodes with no water intercalated between them. The predicted charge densities vary linearly with the applied potential difference. The results, which bare the impact of Coulomb interaction with and without the long-range effect in describing non-bonded electrostatic potential in the charge equilibration models, are consistent with those obtained in the previous chapter that shows QEq predicting more charge at zero solvent placed between the electrodes. Subsequently, we intercalate the inter-electrode space with water. And observe

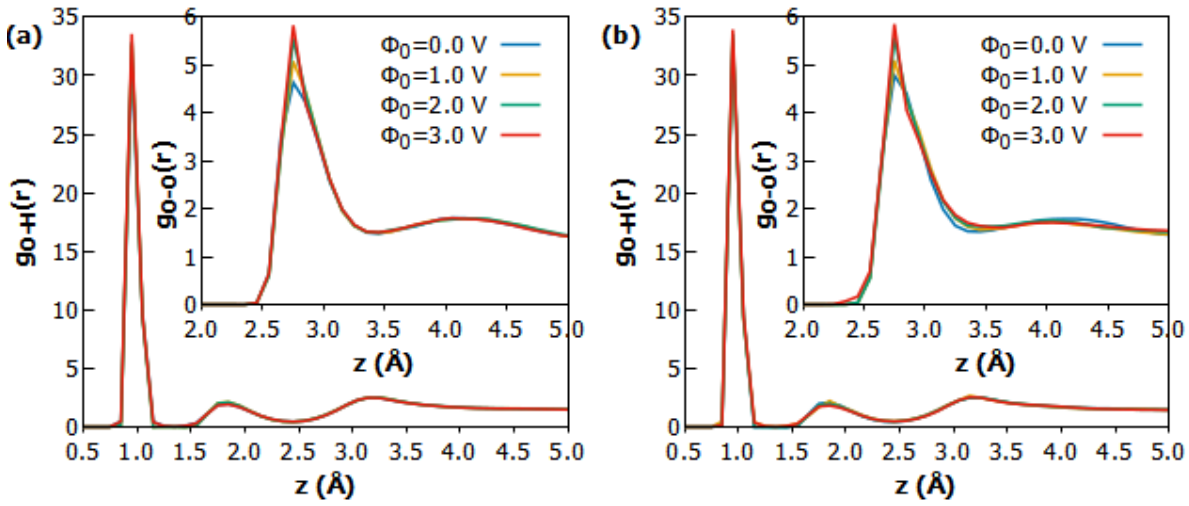

Figure 6. 6: Partial RDFs $g_{O-H}(r)$ and $g_{O-O}(r)$ of water atoms without (a) and with (b) long-range Coulomb for various Φ_0 and for $d_{sep} = 25.00$ Å.

the surface charge density evolution with increased separation between the electrodes at a zero applied field. The charge values or surface charge densities at 0.0 V are possible, consequent to the (i) differences in the electronegativity of the electrodes' atoms and the atoms of the water molecules and the interactions existing thereof, and (ii) dipolar orientation of water molecules. Note that the charge values vary a little for the two electrodes and are not linear with separation (the numerical extent of this variation is highlighted under additional investigation in sub-sec. 6.7) as expected since water has different orientations [224] at the electrolyte/electrode interfaces. That is because the electrode charges adjust in response to the local field changes and charge fluctuation due to the water atoms described by a reactive field function other than the SPC/E-modelled water with fixed oxygen and hydrogen charges. This calculation and others in subsequent sub-sections are done with the inter-electrode space intercalated with water.

Table 6. 2: Total surface charge density ($\mu C/cm^2$) on the electrodes at various applied potential and with no water intercalated between the electrodes. LE(RE) = left electrode (right electrode).

Φ_0	QEqLR		QEq	
	LE	RE	LE	RE
0.0	0.000	0.000	0.000	0.000
1.0	1.103	-1.103	2.082	-2.082
1.6	1.764	-1.764	3.331	-3.331
2.0	2.206	-2.206	4.164	-4.164
2.2	2.426	-2.426	4.580	-4.580
3.0	3.308	-3.308	6.246	-6.246

6.6 Electrodes Surface Charge Distribution

Figure 6.7 is a distribution (histogram) of the partial charge on carbon atoms of the positive (solid lines) and negative (dashed lines) electrodes, averaged over the entire statistic production time. The distribution is non-Gaussian but a bimodal [224], and it exhibits similar behaviors as the non-Gaussian charge distribution recorded in a simulation by Baris [225]; however, the systems differ from ours in that the electrolytes were ionic liquids. The non-Gaussian charge distribution, perhaps, delineates some differences between dynamic and fixed charge models [226], such as charge adjustments in the former to respond to local charge density fluctuations between an electrolyte and the electrode atoms. Evidence in the plots is a drifting of the mean of the histograms away from zero at increasing the potential difference between the electrodes.

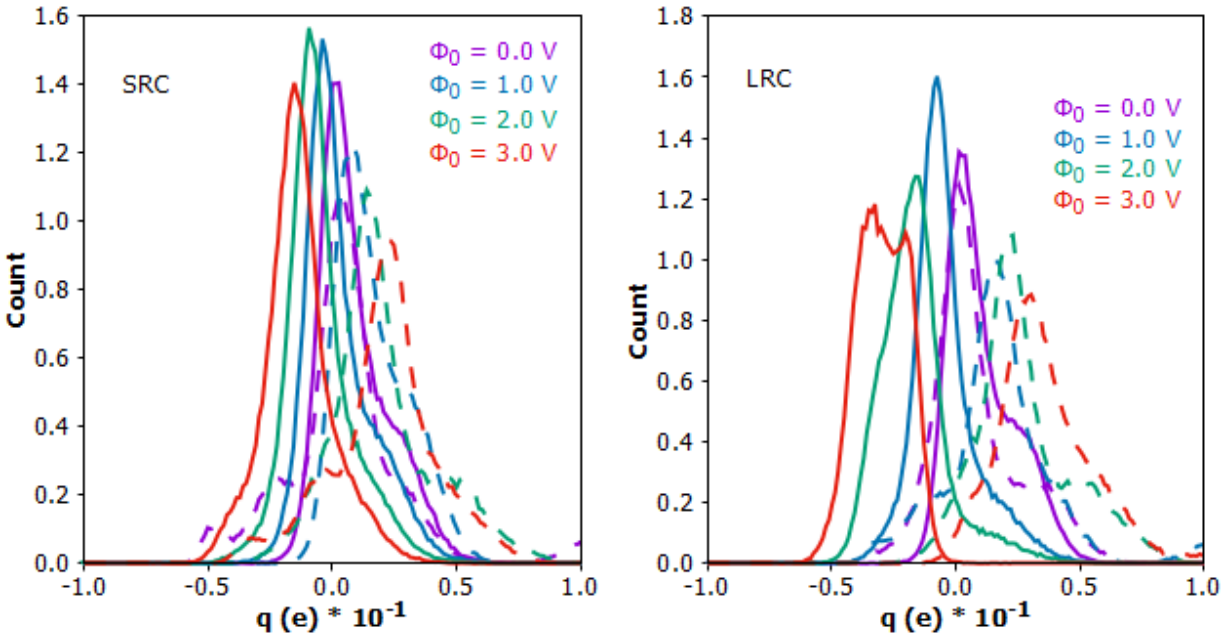

Figure 6. 7: Distribution of graphene atom charges for positive (solid lines) and negative (dashed lines) electrodes at various applied potential difference.

That shift is more pronounced during electrode polarization with LRC than the SRC, which indicates that the LRC could be encouraging charge over-screening [227] that delivers more counter charge than the absolute value of the electrode charges at the interfacial layer more than the SRC; especially when ionic liquids become the electrolyte. The Figure shows varying amplitudes, which explains the fluctuation in the number of electrode atoms possessing certain partial charges due to interfacial water molecules/atoms interaction. The bimodal distribution is a consequence of the ordering/orientation [224], [228] of the water molecules seen on the OH bonds' responses to the applied field, which could be tilting toward the graphene surface or away from it.

6.7 Time Evolution of Surface Charge at the electrode

Figure 6.8 describes the total surface charge on the negative (positive) electrode, which is the sum of individual atomic charges as a function of simulation time evaluated at various applied voltages. Except for the zero potential, LRC predicts more surface charges on the electrode than the SRC; for example, at 3.0 V, the LRC average q_{tot} is about 1.16e against 0.84e for SRC; thereby elucidating the influence of allowing long-range Coulomb in the presence of applied potential. Combining this result with Figure 6.4 suggests that LRC orders more structure near the surface of the electrodes than the SRC. The atom charges, including those of the solvent, fluctuate with time; therefore, the total q_{tot} fluctuates. But the averages $\langle q_{tot} \rangle$ of these fluctuations indicated on the plots by dotted and solid horizontal lines for QEq and QEqLR, respectively, after a long equilibration, are the actual quantity needed for quantifying the capacitance of the capacitor.

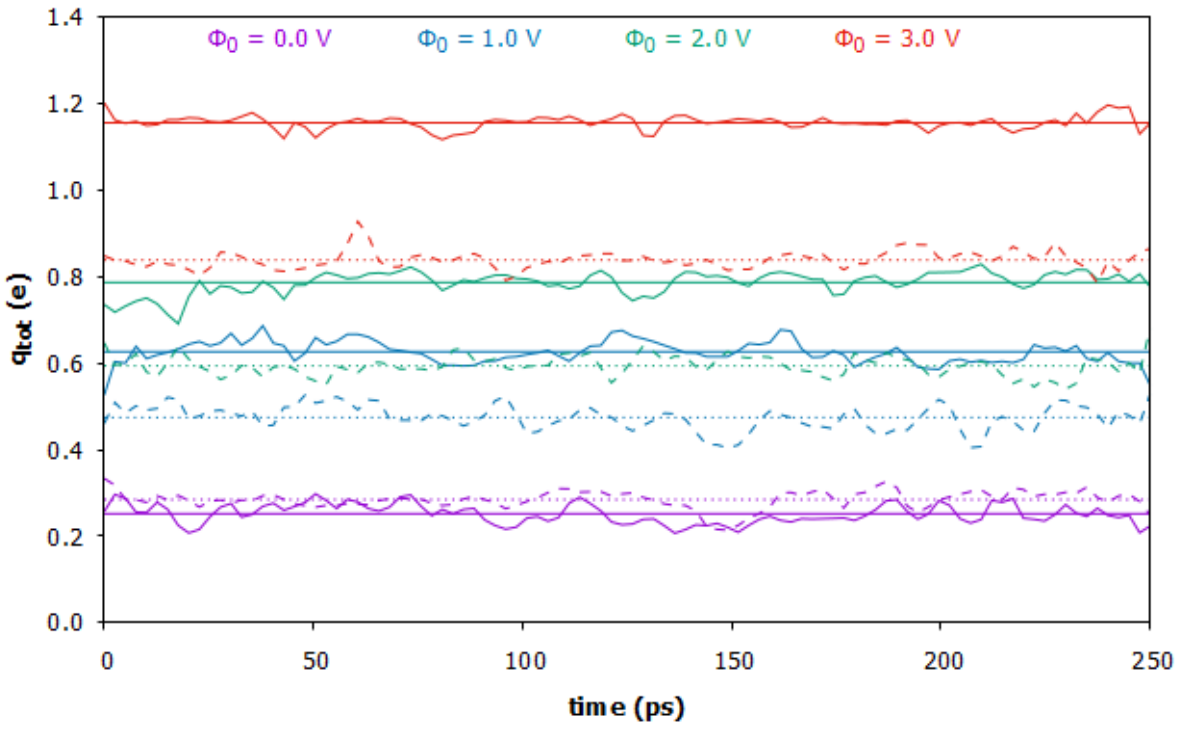

Figure 6. 8: Time evolution of total q_{tot} and average total $\langle q_{tot} \rangle$ electrode surface charge as a function of applied voltage Φ_0; fluctuating dashed and solid lines represent SRC and LRC, respectively while dotted and solid horizontal lines are the corresponding average total surface charges.

An additional investigation deals with how the electrode atom charges respond to increasing g inter-electrode spacing over the simulation times. Note that the atom charges fluctuate in time but vary inappreciably over separation. However, the net electrode charges

change significantly within a small window while increasing the separation between the electrodes. The average net electrode charges are within 0.105 – 0.279 e (0.181 – 0.312 e) at the positive electrode and 0.103 – 0.284 e (0.085 – 0.310 e) at the negative electrode for QEq (QEqLR) in non-linear order with the lower values corresponding to the system with the minimum electrode separation (i.e., the most confined state). The results indicate that long-range QEq is not necessarily needed to characterize the same electrode material capacitive devices subjected to zero applied fields; conversely, SRC models underperform when the systems are tuned to an external voltage, as shown in the total surface charge density.

6.8 Integral Capacitance of the Device

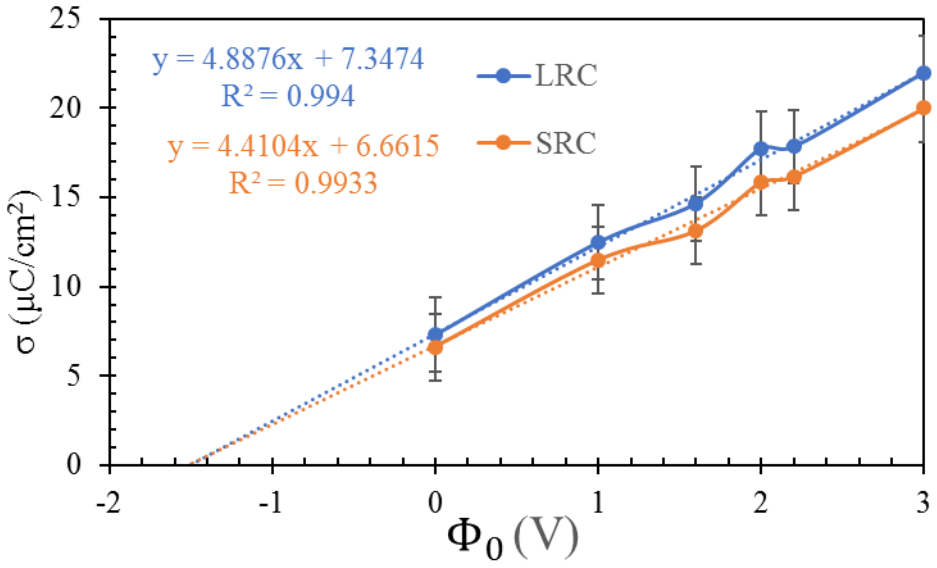

Figure 6. 9: Surface charge density on the positive electrode as a function of the applied potential difference with standard deviation expressed as error bars.

Figure 6.9 shows the interfacial average surface-charge density $\langle\sigma\rangle$ on the positive electrode as a function of the applied potential. As expected, the predicted surface charge densities or charges are in linear correspondence with the applied potential, which results in a constant value for the integral capacitance. The capacitance is defined here according to [229] – [231]. And for easy calculation, it is simplified as a ratio of average surface-charge density $\langle\sigma\rangle$ to potential difference across the electrodes (in this case, the applied voltage values and not the potential drop of the electrode relative to the bulk region of the system).

$$C_{int} = \frac{\langle q_{tot}\rangle}{A\Phi_0} = \frac{\langle\sigma\rangle}{\Phi_0} \tag{6.1}$$

$\Phi_0 = \Phi_0^+ - \Phi_0^-$ is the potential difference applied across the electrodes, which equals the overall (sum of the) potential drops between the bulk of the electrolyte and the individual electrode surface. From the plot (Figure 6.9) and linear regression of the data, the capacitance recorded is 4.4 ± 0.2 and 4.9 ± 0.2 μF cm^{-2} with QEq and QEqLR, respectively. The results are comparable with 5.0 μF cm^{-2} recorded for liquid water with an extended single point charge (SPC/E) model, intercalated between graphene electrodes, and studied using MD simulations [86]. The substantial difference between the short-distance and long-range Coulomb models is not surprising since the latter includes a more realistic description of the interaction field between atoms in a system. The intercept on the vertical axis corresponds to the interfacial surface charge density due to the interaction between the atoms of the electrode and the water molecules at a zero applied field for system L. The integral capacitance is a measurable quantity for quantifying the energy density of supercapacitors. By the results obtained and comparisons made, SRC under-predicts this quantity by 12 %.

6.9 Spatial Distribution of Atomic Charges

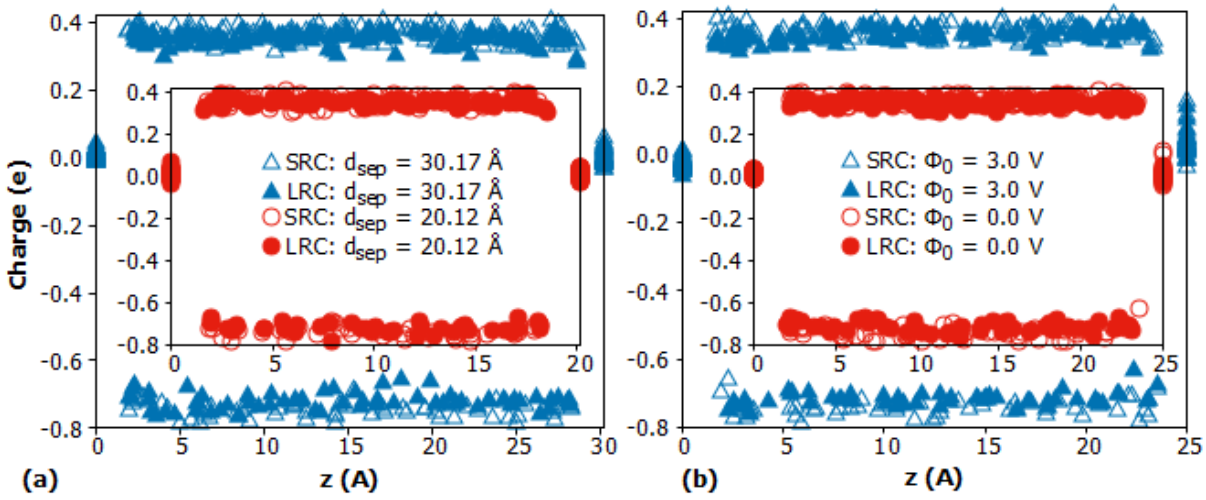

Figure 6. 10: Spatial distribution of charges for (a) systems XM and XL at zero-volt bias, and (b) system L at 0.0- and 3.0-volts bias. The top and bottom points represent the H and O atoms while the left and right points are the electrodes. Hollow and solid points represent SRC and LRC respectively.

Figure 6.10 shows the partial charges of the atoms spatially distributed over space at an instant to quantify the charge dynamics of the water atoms. Note that the water atom charges fluctuate inappreciably in time and over separation. However, the net individual electrolyte atom charges change significantly over increasing the separation between the electrodes. The increase is due to the increased number of water molecules required in each channel

configuration to maintain the bulk density of the water at unity for each system. Therefore, from the figures, the water atoms possess average partial charges of the magnitude $q_H = 0.367 \pm 0.020\, e$ $(q_O = 0.743 \pm 0.021\, e)$ and $q_H = 0.353 \pm 0.021\, e$ $(q_O = 0.715 \pm 0.021\, e)$ lying between the experimentally obtained values quoted in Table 5.1 and $q_H = 0.4238\, e$ $(q_O = 2q_H)$ of the SPC/E water. Notice that the QEq and QEqLR charges for the water atoms in Table 5.1 differ sparingly from the results here; the difference results from the variations in parameters of the force field used in the calculations. Observe that q_O does not strictly equal $2q_H$; that is the consequence of fluctuating charge technique where the atom charges depend on their local environment; however, while the electrodes offset the deficit in the water atom charges, the overall charge of the system is to the order of 10^{-6} zero.

6.10 Charge Density Distribution in the Electrolyte

Instead of the smooth exponential decay described in chapter two for the ion concentration or charge density, the atomistic simulation considers fine structures and local arrangements of atoms and molecules for calculating the electrode/electrolyte interface properties. The local charge density ρ_q of the electrolyte as a function of the coordinate z in the direction normal to the electrode surface follows Eq. (6.2) as is given by:

$$\rho_{qj} = \int \rho_i(z')dz' = \frac{1}{\mathrm{V}}\left[\sum_{i=1}^{N} q_i\right]_{z_0+jh_z}^{z_0+(j+1)h_z} \tag{6.2}$$

Here, the density of the fluid is inhomogeneous especially at the interfacial regions, and therefore, generates inhomogeneous partial charge distribution for the atom species in the systems. Consequently, the charge density distribution $\rho_i(z) = \sum_i q_i \delta(z - z_i)/\mathrm{V}$ (δ denotes the Dirac delta function) of a water molecule between the electrodes arises from a set of point charges q_i, and is calculated by binning the position of the atoms with their associated partial charges into small rectangular bins along the z-direction. V equals the area A_{xy} of the xy-plane multiplied by the bin size h_z, and it equals the bin volume. The lower and upper limit of each bin is $z_0 + jh_z$ and $z_0 + (j+1)h_z$ with $0 \leq j \leq nbins$ (number of bins). q_i are the charge of ith atoms bounded by the bin walls, within which the charge density ρ_q relating to bin j is computed. A case where the atom species possess equal partial charges, the charge density is simply $\rho_q = \sum \rho_\alpha . q_\alpha$ (ρ_α and q_α are the number density and the partial charge of species α). Note we had no mobile ions that would adsorb at the electrode; therefore, electrostatic

screening at the electrodes resulted from the developed interactions of the electrode atoms and those of the water, plus the reorientation of the water dipoles.

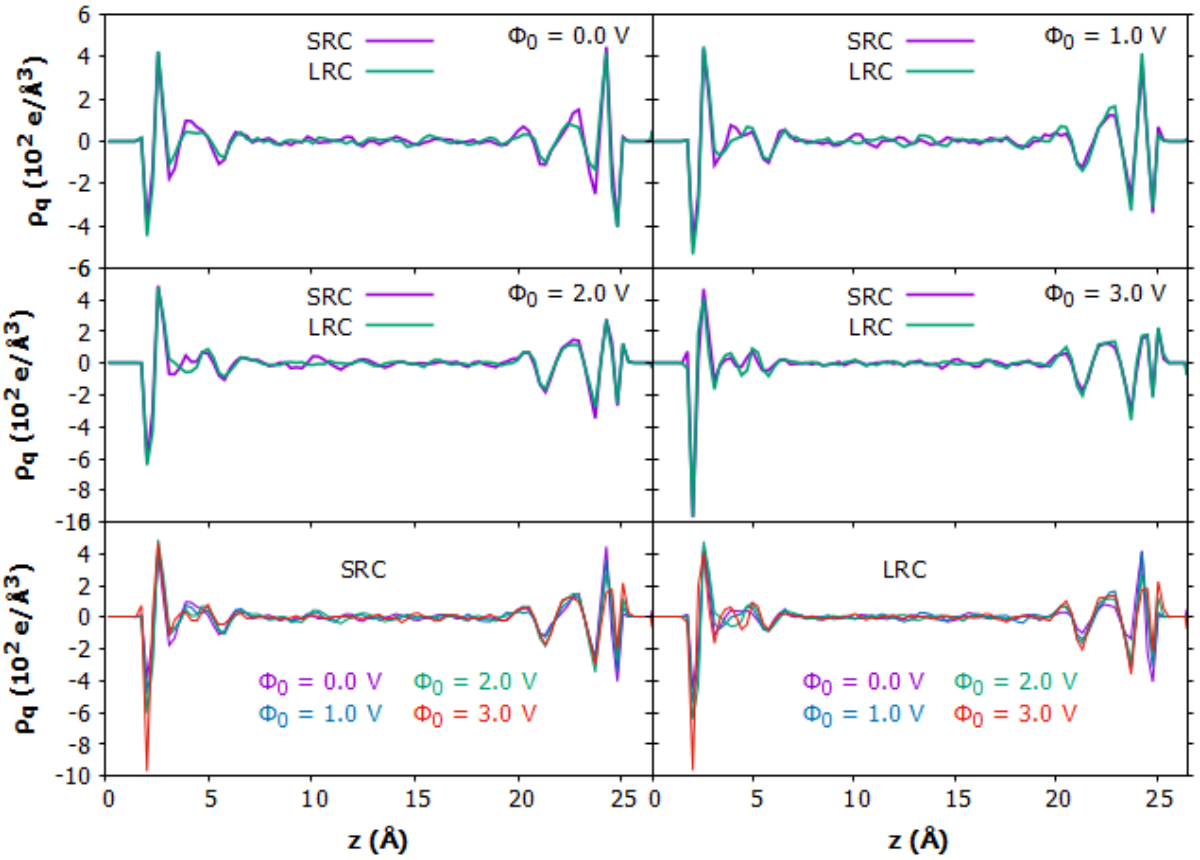

Figure 6. 11: Charge density profile of system L at various Φ_0 applied across the graphene electrodes for the short-range (SR) and long-range (LR) Coulomb descriptions of interaction among atoms.

Figure 6.11 shows the charge density distribution along the electrodes' normal surface (z-direction) at different potential differences. It portrays charge oscillations near the surfaces of the electrodes with alternating negative and positive peaks, which extend to about 5 Å into the system before showing bulk-like distribution for the electrolyte in zero and non-zero applied voltages. For all Φ_0, the plots compare the short- and long-range Coulomb (SRC and LRC) results. The two models gave an identical pattern of charge distributions except for a minor difference where LRC seems to project more negative charge to the left electrode surface than the SRC at the non-zero potentials. As an external potential difference is applied, the system becomes polarized. At 0.0 V, the charge distributions exhibit symmetry between the negative and positive peaks co-existing at both electrode surfaces, which were the consequence of the interactions between the graphene electrodes and the atoms of the water molecules. On switching the voltage to various values, the systems became polarized, and an excess positive

charge developed near the right electrode leading to negative atom charges near the left electrode in compliance with the applied field. These charge distributions at interfacial regions generate additional electric fields, which add to those of the applied voltage and influence the orientation of the water molecules toward and away from the positive electrode breaking the symmetry (Figures 4) of the density profile.

6.11 Poisson Potential and Differential Capacitances

Proceeding further to characterizing the device leads to a more complex electrostatic potential file, which could be solved by evaluating the Poisson equation along the surface normal to the electrodes. Solving the Poison equation allowed the computation of the evolution of the potential across the device. The electrostatic potential and the ionic distribution of Eq. (2.4) relate through the Poisson-Boltzmann equation, which in the anisotropic z-axis that is normal to the electrode surface is:

$$\frac{\mathrm{d}^2\Phi}{\mathrm{dz}^2} = -\frac{Ze}{\varepsilon_0}[c_+ - c_-] = -\frac{\rho_q(z)}{\varepsilon_0} \tag{6.3}$$

This second-order non-homogeneous differential equation is solved while recognizing two boundary conditions depending on the method [232] employed for calculating the potential. Here, the solution and potential across the electrodes are sorted analytically with the one-sided Green's function method, which seems to be a favorable method for researchers [232] – [234] to obtain the complementary homogeneous and the particular integral solutions that yield the following general solution:

$$\Phi(z) = -\frac{1}{\varepsilon_0}\int_0^z \int_{z'}^z dz'' \rho_q(z')dz' + C_1 z + C_2 = -\frac{1}{\varepsilon_0}\int_0^z (z - z')\rho_q(z')dz' + C_1 z + C_2 \quad (6.4)$$

The final Poisson potential is evaluated numerically through the numerical integration method (specifically the trapezoidal rule), which allows the binning of the atomic positions and the charge density distribution as employed in [232]. ρ_q is the average charge density across the cell, including contribution from the electrodes. C_1 and C_2 are integration constants for the electrodes located at z_0 and $z_{d_{sep}}$, usually at $z_0 = 0$ and $z_{d_{sep}} = d_{sep}$, relating to $\mp\Phi_0/2$ volt perturbation applied alternately to both electrodes, respectively. Figure 6.12 gives the electrostatic potential calculated with the Poisson equation illustrated above. Note that the potential fluctuates in the two models and oscillates heavily near the surfaces of the electrodes on which it drops. The oscillations extend to about 7.5 Å measuring from the electrodes before

exhibiting constant values in the interior around the bulk region of the system. Although little ripples exist in the bulk portion of the system, not only with the potential but also on the water and charge density profiles. These are due to the prevailing slow relaxation of the water, which would require longer simulation times and the accumulation of more statistics to generate smoothly distributed profiles.

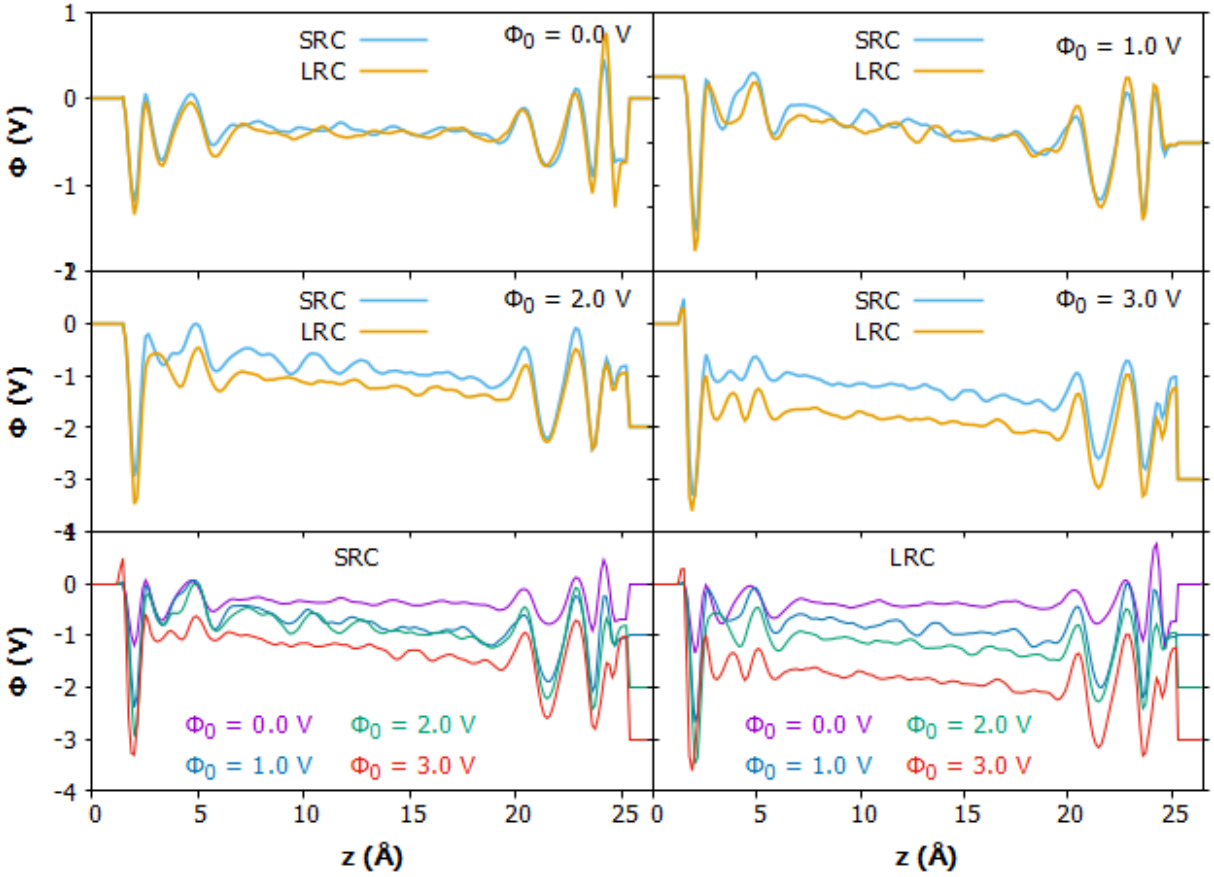

Figure 6. 12: Poisson potential profiles across the simulation cell calculated at various applied voltages Φ_0 and compared between the SRC and the LRC.

The profound near-electrode surface oscillations are due to the ordering of the water molecules in these regions, as depicted in the water density and charge profiles. The SRC and LRC approach behave alike in oscillation patterns; however, some significant differences abound in the responses to applied voltages. The differences are related to the average partial charges on the surfaces of the electrodes. Notice that the potential plots show constant steepness typical of a bulk dielectric system under an applied electric field; with LRC predicting higher numerical values at the positive left electrode and lower values at the negative right, the SRC yields the reverse results. It seems like LRC tends to stabilize charge separation (screening) at the interfacial layers to a much greater extent than the SRC when judged by the potential drops and the differential capacitance at the electrodes.

The differential capacitance C^s_{diff} is a single-electrode capacitance calculated as the ratio of the average surface charge density $\langle\sigma\rangle$ on one of the electrodes to the potential drop $\Delta\Phi^{\pm}$ across the same electrode relative to the center (bulk region) of the capacitor. It gives details of the solvation, ion or charge absorption, and general physiochemical processes happening at the interfacial region more than the integral capacitance that informs about the energy storage density. This quantity is always written in a compact form as follows; Φ_{bulk} is the Poisson potential at the center of the capacitor:

$$C^s_{diff} = \frac{\partial\langle\sigma\rangle}{\partial\Delta\Phi^{\pm}};\ \text{where}\ \Delta\Phi^{\pm} = \begin{cases}\Phi^{+} - \Phi_{bulk};\\ \Phi^{-} - \Phi_{bulk};\end{cases} \tag{6.5}$$

The slopes of the linear fits in Figure 6.13 give the differential capacitance as $C^{-}_{diff}\left(C^{+}_{diff}\right) = 10.7(9.9)\ \mu F/cm^2$ and $C^{-}_{diff}\left(C^{+}_{diff}\right) = 7.0(16.2)\ \mu F/cm^2$ for the LRC and SRC models, respectively. The results show that the capacitance is higher on the positive electrode than on the counterpart for the SRC. For LRC, the capacitances are close but slightly higher on the negative electrode than on the opposing one. It also shows that the average surface charge density to electric potential drop ratio on the surfaces of the electrodes is distributed equitably with the LRC than is with SRC.

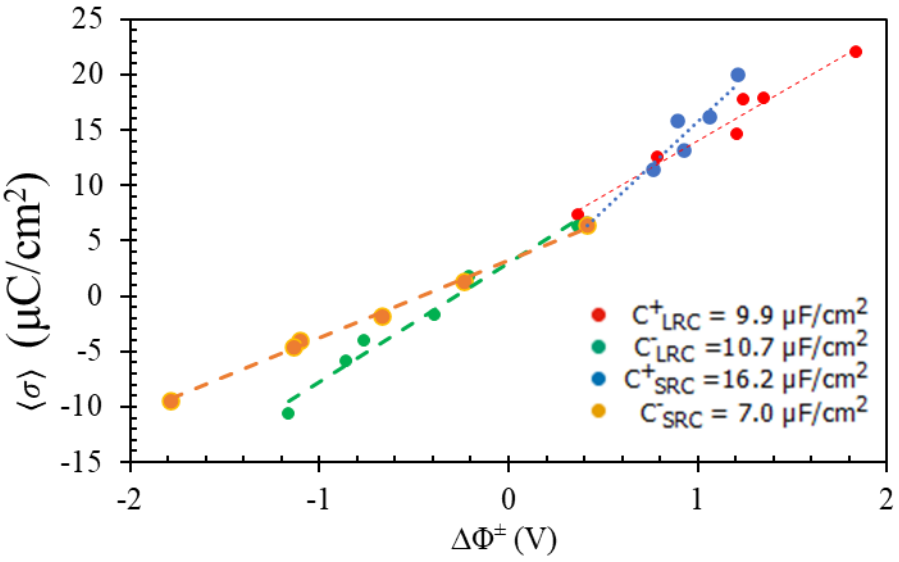

Figure 6. 13: Surface charge density as a function of interfacial electrostatic potential drop relative to the bulk region. The slopes of the linear fits give the differential capacitance.

Checked against the literature, [235] calculated the C^s_{diff} of graphene supercapacitors with an ionic liquid electrolyte to have slightly higher negative electrode capacitance than the positive electrode in all systems studied. [207] C^s_{diff} also computed the

negative electrode to have higher differential capacitance than the positive one for a graphene/ionic-liquid electrolyte system; the same trend was the works of [235] - [237] with graphene electrodes and ionic liquids. Against these checks, LRC seems to predict better information about the electrodes than SRC.

Chapter 7

Conclusion and Future Prospect

7.1 Conclusions

We were interested in studying capacitors or super-capacitors, ECM cells, EDLs, and batteries with QEq and ReaxFF via reactive atomistic simulations. But the numerical implementations of QEq and ReaxFF treat the Coulomb interaction up to a short-distance cut-off (usually about 10 Å) and reduce the number of pairwise non-bonded interactions between atoms for better computational speed. Beyond the cut-off, the potential function describing the atomic interactions is truncated to zero using polynomial functions. However, Coulomb interaction is long ranged for non-covalent interactions (NCI). Such interactions exist in ionic and polarized systems where the motion of charged particles characterizes the electrical and electronic properties and behaviors of the devices such as capacitors, ECM, EDLs, and batteries.

Therefore, these models are only accurate for small systems whose atomic spreads are within the cut-off distance allowable for atoms to interact. Otherwise, the interaction of an atom with others in large systems is only regional and it only extends to the particles in the neighbor list of the focused atoms at any time step. It does not matter whether the Coulomb force or energy has sufficiently decayed to zero; energy contributions beyond the said radius are ignored. To perform MD simulations, for which the separation between the electrodes is more than 1.0 nm, we needed a long-range interaction model for charge equilibration calculations. Thus, this work gained impetus from these challenges to utilizing the Ewald summation to develop QEqLR that calculates charges under realistic Coulomb interactions. Therefore, the primary purpose of this study was to develop long-range Coulomb models for the evaluation of dynamic charges and forces in reactive molecular dynamics (MD) simulations. Implement the long-range Coulomb for QEq evaluation of atom charges and ReaxFF computation of Coulomb forces and energy of a particle. Then, they are applied to study a capacitive device.

In this work, we have included long-range effects on the shielded Coulomb interaction function in reactive force potential and implemented a stand-alone shielded long-range Coulomb pair interaction potential. Then we used the models to compute Coulomb forces and energy on simple systems of $MgCl_2$ and NaCl, respectively. Generally, the results are in perfect

agreement when matched with the analytical results. And they depict the expected shielded Coulomb curves compared with the solutions via the Slater integral of Coulomb potential. For the stand-alone potential, the energy per unit volume as a function of the increased size of the supercell is constant, as expected. The Coulomb interaction force, as well as energy, are shielded consistently at short interatomic separations. That is an improvement to the unphysically repulsive energy and forces recorded when atoms are at short-distance separation in the order of vdW diameter or less between them. For the Reaxff inclusion, there were improvements accounting for the real-space short-distance part of long-range Coulomb. We could achieve a striking agreement between Ewald and Reaxff with shielded long-range correction.

On the charge model, in view of applying dynamical charge equilibration to compute atomic partial charges for the reactive molecular dynamics simulation of large-scale electrochemical systems, we have included a long-range effect on the Coulomb interaction potential. The reformulated QEq termed QEqLR utilized the Ewald sum to modify the Coulomb interaction terms in the QEq equation. In addition, it includes modification to the real-space part of the Ewald summation to offset orbital overlaps problems. QEqLR yield charges in acceptable agreement with the *ab initio* method for the simple systems tested and MOF charges compared at a default Ewald splitting parameter of 0.15 Å. We showed that by shifting between the real- and reciprocal space contributions to the interaction function, we could fit charges to DFT methods. A property that QEq lacks once the atomic electronegativity, chemical hardness, and shielding parameters are deduced from the ionization energies, electron affinities, and atomic radius. Throughput analyses of the evolution of surface charges in Cu-Cu parallel plates capacitor configuration under an external field reveal that QEq overestimates and predicts constant charge distribution on the electrodes. Contrarily, QEqLR improves on the results by predicting decaying surface charge distribution against separation after the order of long-range Coulomb potential energy and force and in agreement with the exponentially decay pattern of the surface charge densities recorded in [187], [188] and [189]. Similar behaviors also were the case with the forces acting along the inner surfaces of the electrodes and their layers.

We employed the models to perform MD simulations for water between sheets of graphene electrodes. The simulations were in two categories: (i) various separations at a zero-voltage bias and (ii) various applied potential differences at 25.00 Å inter-electrode separation. At all

inter-electrode spacing, water shows strongly stratified lamellae of density modulations in the direction normal to the electrode surfaces. We observed related results from both models; however, a closer inspection unveils some differences. LRC predicts a little more structured solvation around the interfacial graphene walls than was seen with SRC, suggesting that the water molecules tilt more to the electrode with LRC. On applying a non-zero potential across the device, LRC reveals a clear relative shift between the oxygen and hydrogen density profiles in agreement with SPC/E modeled water between Pt walls than the SRC. The RDF illustrates that the location of extrema in both models is at the same position, and an increase in inter-electrode spacing or applied potential does not change the location of the peaks. Instead, it results in appreciable peak reduction at increased d_{sep} or a slight increase with increasing external voltage with those of the LRC higher a little. That indicates that even though the molecules of water structure are uninfluenced, the reorientation and ordering near the electrodes are affected. Both results perfectly agree with the X-ray diffraction experiment [221], [222], and DFT [223], an indication that the LRC preserves the structural properties of water between the graphene electrodes. On the charge densities, we recorded a higher surface charge density with the LRC and a capacitance value of $4.9 \pm 0.2\ \mu\mathrm{F/cm^2}$ compared with $4.4 \pm 0.2\ \mu\mathrm{F/cm^2}$ predicted by the SRC model. The results imply that SRC underestimated the capacitance of water between graphene walls by 12 % when compared with the $5.0\ \mu\mathrm{F/cm^2}$ predicted with the SPC/E water model. The differential capacitances of the electrodes were $C^{-}_{diff}\left(C^{+}_{diff}\right) = 10.7(9.9)\ \mu\mathrm{F/cm^2}$ and $C^{-}_{diff}\left(C^{+}_{diff}\right) = 7.0(16.2)\ \mu\mathrm{F/cm^2}$ for the LRC and SRC models, respectively.

This research project provides a technique for modeling electrochemical processes in different devices at a more realistic Coulomb interaction description and fosters the processing of the details about the operation of these devices**.** This approach would describe electrochemical systems with practical electrolyte thickness while conserving the electrostatic effect of charged electrodes throughout the dielectric layer and would apply to devices such as batteries and emerging solid-state memory. The implementation part of the thesis completed the challenging programming work of adding new computational algorithms to the sophisticated open-source software, viz. LAMMPS.

Table 7. 1: Tabulated summary of calculations made and models used on various systems, accompanied with concluding remarks

Systems	Quantity Calculated	Model Used		Compared calculation with	Concluding Remark
		Old	New		
MgCl2	Coulomb force and Energy	ReaxFF, and ReaxFF + LR effect	Reformulated ReaxFF	Analytical (1/r) and Ewald results	ReaxFF + LRC agree with analytical or Ewald result.
NaCl		LR Coulomb	Shielded LR Coulomb	Ewald	Catastrophic repulsions at close-distance interaction are resolved.
Simple molecules; e.g., NaCl, NH3, CH4, HF, CH4O3	Partial atomic charge	QEq	QEqLR	DFT/Experimental charge	Minor differences exist between charges computed with both models. QEqLR compares better with DFT/Expt results.
Complex structures; e.g., MOFs				REPEAT and EQEq charges	QEq poorly predicts charge on the MOF atoms, but QEqLR improves the results.
Some solid-state/ionic materials				Bader charges	QEqLR charges are in better agreement with Bader charges than QEq charges.
Model parallel plate capacitor	Total surface charge and forces	QEq + (Coul/cut and Coul/long)	QEqLR + (Coul/cut and Coul/long)	Decay pattern with Expt.	QEqLR with Ewald approach gives more adequate estimate of charges and forces on the electrodes.
Graphene-water capacitor	Structural, Electrostatic and capacitive properties	QEq and ReaxFF	QEqLR and Reformulated ReaxFF	SPC/E water model	Water bond properties were preserved in both models. SRC under-predicts the capacitance by 10 %.

7.2 Future Work

Presently, QEqLR runs only in **serial** as a piece of software plugin, i.e., a fix, in our installed LAMMPS-31Aug2021 version. As such, it is used effectively for single-point calculation and dynamical simulations of very few (about 200 – 500) atoms due to its low speed. So, part of our plan is to implement it in **parallel**. Then, study electrochemical processes with the target to explore resistance switching in ECM cells and high charge density ordering in super-capacitors, EDL devices, and batteries.

Specifically, we will perform simulations with the QEqLR to demonstrate resistance switching in $Cu/SiO_2/Cu$ ECM cells using electrochemical dynamics with the implicit degree of freedom model [8], [204]. This model can provide a description of electrochemical reactions under applied electrical bias by solving the diffusion equation for the electrochemical potential propagated from each metallic electrode during reactive simulations. The aim will be to recharacterize the device under this improved QEq model to evaluate the switching time and retention.

It would be likely worthwhile to develop a full environment-dependent QEq scheme where, instead of a fixed architecture per atom type in a system that makes all elements of the same type chemically equivalent, the electronegativity as well as the hardness terms will depend on the positions of the interacting atom in the system. The project would resolve the problem of infinite charge separation witnessed with QEq completely. It would contribute to a better understanding of the polarization physics in charged or polar systems. The project would be likely conducted through a data-driven numerical and machine learning techniques using experimental or *ab initio* data for validation to reduce the computational cost.

Appendices.

A. Appendix for chapter 4

A.1 Detail Equation of QEq

In the development of QEq by Rappä amd Goddard [29], also called the electronegativity equalization method (EEM) by Mortier *et al* [150], the electrostatic energy of an isolated atom i as a function of charge, Q is Taylor expanded around its neutral reference state up to second order as:

$$E_{i\to i}(Q) = E_{i_0} + Q_i\left(\frac{\partial E}{\partial Q}\right)_{i_0} + \frac{1}{2}Q_i^2\left(\frac{\partial^2 E}{\partial Q^2}\right)_{i_0} + \cdots \qquad \text{(A. 1.1)}$$

The atom in its neutral reference state, i.e., the charge is zero, possesses energy equal to the energy of its ground state as:

$$E_{i\to i}(0) = E_{i_0} \qquad \text{(A. 1.2)}$$

Because Eq. (A.1.1) is expressible in terms of measurable physical parameters such as ionization potential (IP) and electron affinity (EA) associated to the removal and addition of an electron to atom *A*, the energy cost of changing the charge state of this isolated atom by ± 1 is considered. Changing the charge by the removal of an electron results in charge state value by $+1$. The associated energy difference between this state and the neutral state is the IP (ionization energy), then, it implies from Eq. (A.1.1) that:

$$E_{A\to A}(+1) - E_{A_0} = \left(\frac{\partial E}{\partial Q}\right)_{A_0} + \frac{1}{2}\left(\frac{\partial^2 E}{\partial Q^2}\right)_{A_0} = IP \qquad \text{(A. 1.3a)}$$

Similarly, changing the charge state by the addition of an electron results in charge state value by -1. The associated energy difference between this state and the neutral state is the EA (electron affinity), then, it implies from Eq. (A.1.1) that:

$$E_{i_0} - E_{i\to i}(-1) = \left(\frac{\partial E}{\partial Q}\right)_{i_0} - \frac{1}{2}\left(\frac{\partial^2 E}{\partial Q^2}\right)_{i_0} = EA \qquad \text{(A. 1.3b)}$$

The electronegativity, χ given by Mullikan is obtained here by adding Eq. (A.1.3 a & b).

$$\left(\frac{\partial E}{\partial Q}\right)_{i_0} = \frac{IP + EA}{2} = \chi_i^0 \qquad \text{(A. 1.4a)}$$

The difference between Eqs. (A.1.3a & b) gives an idempotent or self-Coulomb term of atom i generally known as hardness J_{ii}^0. The hardness is the ability of an atom to resist change to its charge state, i.e., to oppose removal or addition of a charge from its state. It results from self-Coulomb integral of electrons doubly occupying orbital, ϕ of atom i and is a function of inverse the atom size.31

$$\left(\frac{\partial^2 E}{\partial Q^2}\right)_{i_0} = IP - EA = J_{ii}^0 \qquad \text{(A. 1.4b)}$$

Substituting Eqs. (A.1.4a & b) in Eq. (A.1.1) returns the total energy cost of changing the charge of this isolated atom by $\pm$ 1 as:

$$E_{i\to i}(Q) = E_{i_0} + Q_i\chi_i^0 + \frac{1}{2}Q_i^2 J_{ii}^0 \qquad \text{(A. 1.5a)}$$

Particularly important in the description of molecular system is the Coulomb interaction potential between atoms. Therefore, if atom i forms a molecule in a system, in which atom j is a member, then, Coulomb electrostatic interaction potential between i and every other j in the system is as given below.

$$E_{i\to j}(Q) = \sum_{i<j} Q_i Q_j J_{ij} \qquad \text{(A. 1.5b)}$$

J_{ij} is the kernel of the Coulomb interaction. In its direct analytical form, it is proportional to the inverse distance between atoms i and j and can be represented by the two-center Coulomb integral function given in the text. Emphatically, $i = j$ may be allowed in Eq. (A.1.5b). This corresponds to the self-Coulomb interaction of charge distribution of an atom with itself; and gives the idempotential of Eq. (A.1.4b) when $J_{ij} \to J_{ii}^0$ as $r_{ij} \to 0$. The total non-bonded electrostatic energy of atom A interacting also with atoms B having charges $Q_1 \cdots Q_N$, N is the total number of atoms in the system, is thus obtained by adding Eq. (A.1.5a & b):

$$E_{sys}(Q_1 \cdots Q_N) = \sum_i \left(E_{i_0} + Q_i\chi_i^0 + \frac{1}{2}Q_i^2 J_{ii}^0\right) + \sum_{i<j} Q_i Q_j J_{ij} \qquad \text{(A. 1.6)}$$

From statistical mechanic, the electrochemical potential μ and/or the electronegativity χ of atoms is defined in terms of charge or number of particles N. In terms of charge, χ is obtained by taking the partial derivative of the total energy of the atoms with respect to each of the atomic charges in the system, i.e., $\partial E/\partial Q$. Therefore, derivative of Eq. (4.7) with respect to Q_A gives the Goddard and Rappë charge equilibration (QEq) equation as:

$$\chi_i(Q_1 \cdots Q_N) = \chi_i^0 + Q_i J_{ii}^0 + \sum_{i \neq j} Q_B J_{ij} \tag{A. 1.7}$$

At electrochemical or electronegativity equilibrium proposed by Sanderson, each atom of the system sees the same electrochemical potential (electronegativity). At this point, it is said that the charges are equilibrated, and any change in the charges results in re-adjustment of the atoms until they feel the same electronegativity or potential. When electronegativity equilibrium is attained, the electronegativity (electrochemical potential) of each atom is equated to one another, thus,

$$\frac{\partial E_{sys}}{\partial Q_i} = \frac{\partial E_{sys}}{\partial Q_j} = \cdots = \frac{\partial E_{sys}}{\partial Q_N} \Longrightarrow \chi_1 = \chi_2 = \cdots = \chi_N \tag{A. 1.8}$$

Eq. (A.1.8) states that the optimal charge values for the atoms occur when the chemical potential is the same for and/or on all the atoms in the system. Equating the chemical potential of each atom to one another gives $N - 1$ independent linear equations in N unknown subject to the constraint or restriction that the total charge in the system is equal to the sum of individual charges. That is.

$$\sum_{i=1}^{N} Q_i = Q_{TOT} \tag{A. 1.9}$$

Expanding Eq. (A.1.7) for each atom in a N system of atoms results in:

$$\chi_1 = x_1^0 + J_{11}Q_1 + J_{12}Q_2 + J_{13}Q_3 + \cdots + J_{1N}Q_N$$
$$\chi_2 = x_2^0 + J_{22}Q_2 + J_{21}Q_1 + J_{23}Q_3 + \cdots + J_{2N}Q_N$$
$$\chi_3 = x_3^0 + J_{33}Q_3 + J_{31}Q_1 + J_{32}Q_2 + \cdots + J_{3N}Q_N$$
$$\chi_4 = x_4^0 + J_{44}Q_4 + J_{41}Q_1 + J_{42}Q_2 + \cdots + J_{4N}Q_N$$
$$\chi_N = x_N^0 + J_{NN}Q_N + J_{N1}Q_1 + J_{N2}Q_2 + \cdots + J_{NN}Q_N$$

For a neutrally charged system, $Q_{TOT} = 0$ then Eq. (A.1.9) and the application of Eq. (A.1.8) to these systems of equations give:

$$Q_1 + Q_2 + Q_3 + \cdots + Q_N = 0$$
$$\chi_2 - \chi_1 \Longrightarrow (J_{21} - J_{11})Q_1 + (J_{22} - J_{12})Q_2 + (J_{23} - J_{13})Q_3 + \cdots + (J_{2N} - J_{1N})\,Q_N = -(x_2^0 - x_1^0)$$
$$\chi_3 - \chi_1 \Longrightarrow (J_{31} - J_{11})Q_1 + (J_{32} - J_{12})Q_2 + (J_{33} - J_{13})Q_3 + \cdots + (J_{3N} - J_{1N})\,Q_N = -(x_3^0 - x_1^0)$$
$$\chi_4 - \chi_1 \Longrightarrow (J_{41} - J_{11})Q_1 + (J_{42} - J_{12})Q_2 + (J_{43} - J_{13})Q_3 + \cdots + (J_{4N} - J_{1N})\,Q_N = -(x_4^0 - x_1^0)$$

These linear equations can elegantly be represented in matrix form as follows:

$$\begin{pmatrix} 1 & 1 & 1 & \cdots & 1 \\ J_{21}-J_{11} & J_{22}-J_{12} & J_{23}-J_{13} & \cdots & J_{2N}-J_{1N} \\ J_{31}-J_{11} & J_{32}-J_{12} & J_{33}-J_{13} & \cdots & J_{3N}-J_{1N} \\ \vdots & \vdots & \vdots & \cdots & \vdots \\ J_{N1}-J_{11} & J_{N2}-J_{12} & J_{N3}-J_{13} & \cdots & J_{NN}-J_{1N} \end{pmatrix} \begin{pmatrix} Q_1 \\ Q_2 \\ Q_3 \\ \vdots \\ Q_N \end{pmatrix} = -\begin{pmatrix} 0 \\ \chi_2^0-\chi_1^0 \\ \chi_3^0-\chi_1^0 \\ \vdots \\ \chi_N^0-\chi_1^0 \end{pmatrix} \equiv C_{ij}Q_i = -D_i \qquad \text{(A. 1.10)}$$

Eq. (A.1.10) is soluble for Q_i by any method of solving a matrix once the elements of the matrices are specified though its solution is sought via matrix inversion (Brute-force) method in our Python implementation. D_i is a column matrix and its elements are given by:

$$D_i = \chi_i^0 - \chi_1^0; \quad i \neq 1 \; and \; D_1 = 0 \qquad \text{(A. 1.11a)}$$

D_1 is zero if we take that at equilibrium, the net charge $\sum_{i=1}^{N} Q_i$ of the system is zero (neutral system), otherwise $D_1 = -Q_{TOT}$. Q_i is a column matrix and are the unknown charge values to be determined. C_{ij} is a $N \times N$ matrix with elements as:

$$C_{ij} = J_{ij} - J_{1j}; \;\; i \neq 1 \; and \; C_{1j} = 1 \qquad \text{(A. 1.11b)}$$

A.2 Detail Equation of SQE

The use of the notion of split-charges to reflect the bond-dependent property of charges results in rewriting the potential energy in terms of bond or pair parameters rather than atomic parameter. This results in an additional term $\frac{1}{2}\kappa_{ij}q_{ij}^2$ in the double sum of the last term of QE (Eq. (A.1.6)) leading to:

$$E(\{r_i\}\{Q_i\}) = \sum_i \left(E_i^0 + \chi_i Q_i + \frac{1}{2}\kappa_i Q_i^2\right) + \sum_{i<j}\left(\frac{1}{2}\kappa_{ij}q_{ij}^2 + Q_i Q_j J_{ij}(r_{ij})\right) \qquad \text{(A. 2.1)}$$

Where κ_i, κ_{ij} and χ_i represent the atomic hardness, bond hardness and atomic electronegativity respectively, q_{ij} is the so-called "split charge." The split-charge represents the charge flown from a covalently bonded neighbor atom j to atom i. In SQE, the net charge, Q_i of an atom is related to the split-charge, q_{ij} by:

$$Q_i = \sum_j^N q_{ij} \qquad \text{(A. 2.2)}$$

Eq. (A.2.2) is the sum of the split-charges debited and credited to an atom by the covalently bonded neighbors. This formalism can be extended to allow ionization states by swapping integer charges across bonded atoms, leading to the redox SQE framework where $Q_i = n_i e +$

$\sum_j q_{ij}$, with n_i the oxidation state of the atom. The equilibration of chemical potential in SQE (or redoxSQE) is done in an analogous manner as in QEq but with respect to split-charges q_{ij}, which corresponds to $\partial E/\partial q_{ij} = 0$. Considering that atom i is connected (bonded) to some atom j, the difference in electronegativity of the connected atoms is represented by an arbitrary value $\bar{\chi}_{ij}$ such that $\bar{\chi}_{ij} = -\bar{\chi}_{ji}$. With the SQE net charge (Eq. (A.2.2)), the above potential energy (Eq. (A.2.1)) of a system of N atoms can be written as:

$$E_{SQE}(\{r_i\}\{Q_i\}) = \frac{1}{2}\sum_{i,j}\left(\kappa_i \sum_j q_{ij} + \bar{\chi}_{ij} + \kappa_{ij}^{(s)} q_{ij}\right) q_{ij} + \frac{1}{2}\sum_{i<j,i',j'} q_{ij} J_{ij}^{i'j'} q_{i'j'} \qquad \text{(A. 2.3)}$$

The one-half factor in the last term of Eq. (A.2.3) accounts for double counting over summation on i' and j'. The atomic hardness κ_i has been influenced by the chemical nature of the atoms, to which it is bonded to, therefore, in relation to the atomic hardness of a connected neighbor atom j, some authors replaced κ_i with κ_{ij}^0, which is an intrinsic or irreducible two-body parameter [155], [156]. However, Nistor and Müser [38] defined κ_i in relation to the entire product $\kappa_i \sum_j q_{ij}$ as a linear average of the difference between the product of κ_i and its Q_i and the product of κ_j and it's Q_j of covalently bonded neighbor atom j, i.e.

$$\kappa_i \sum_j q_{ij} = \frac{1}{2}(\kappa_i Q_i - \kappa_j Q_j) \qquad \text{(A. 2.4a)}$$

Since there are no doubly indexed two-body parameter in QEq, therefore, to express QEq as the limiting case to the general SQE method, Eq. (A.2.4a) is re-written in Eq. (A.2.4b) as a linear combination of doubly indexed parameters, which are expresses in terms of singly indexed atomic parameters given in Eqs. (A.2.6 b & c).

$$\kappa_i \sum_j q_{ij} = \kappa_{ij}\bar{Q}_{ij} + \bar{\kappa}_{ij} Q_{ij} \qquad \text{(A. 2.4b)}$$

The introduction of the two-body parameters in the QEq technique makes the parametrization of several other schemes [38] possible through setting one or two parameters to zero in the general SQE. Thus, we re-express Eq. (A.2.3) using Eq. (A.2.4b) in a mixed atomic- and split-charge form as:

$$E_{SQE}(\{r_i\}\{Q_i\}) = \frac{1}{2}\sum_{i,j}\left(\kappa_{ij}^{(s)} q_{ij} + \kappa_{ij}\bar{Q}_{ij} + \bar{\kappa}_{ij} Q_{ij} + \bar{\chi}_{ij}\right) q_{ij} + V_C \qquad \text{(A. 2.5)}$$

$$V_C = \frac{1}{2}\sum_{i<j,i',j'} q_{ij} J_{ij}^{i'j'} q_{i'j'} \qquad \text{(A. 2.6a)}$$

$$Q_{ij} = \frac{(Q_i + Q_j)}{2} \text{ and } \bar{Q}_{ij} = \frac{(Q_i - Q_j)}{2} \qquad \text{(A. 2.6b)}$$

$$\kappa_{ij} = \frac{(\kappa_i + \kappa_j)}{2}, \qquad \bar{\kappa}_{ij} = \frac{(\kappa_i - \kappa_j)}{2} \text{ and } \bar{\chi}_{ij} = \chi_i - \chi_j \qquad \text{(A. 2.6c)}$$

The equations labelled A.2.6c are the so-called "charge equilibration rules," which make Eq. (A.2.5) similar in form and relation to Eq. (A.1.6). It is important to note that the following relations generally hold true.

$$i.\ q_{ij} = -q_{ji} \quad \text{ii. } \bar{\chi}_{ij} = -\bar{\chi}_{ji} \quad \text{iii. } \kappa_{ij} = \kappa_{ji} \quad \text{iv. } \bar{\kappa}_{ij} = -\bar{\kappa}_{ji} \quad \text{v. } \kappa_{ij}^{(s)} = \kappa_{ji}^{(s)} \qquad \text{(A. 2.7)}$$

Before we set to minimize Eq. (A.2.5), let us for understanding, explain the form of the Coulomb interaction in the split-charge framework. For illustration, consider Figure A.2.1 below with N atoms ($N = 6$), in which we want to determine the Coulomb interaction Eq. (A.2.6a) between atoms 1 and 2. Let atom 1 be represented by i and any atom connected to it except for atom 2 be represented by i'. In analogous manner, let atom 2 be j and any atom connected to it except for atom 1 be j'. The Coulomb interaction J_{ij} between i and j is given as the sum of the interactions of i with atoms i' and the interactions of j with atoms j' minus the sum of the interactions of i with atoms j', and the interactions of j with atoms i' as given in Eq. (A.2.8). Each term on the right side of Eq. (A.2.8) depends on inverse distance between the atoms and is here evaluated with Slater integral function, thus orbital overlap of electronic wave function of two interacting atoms is accounted for.

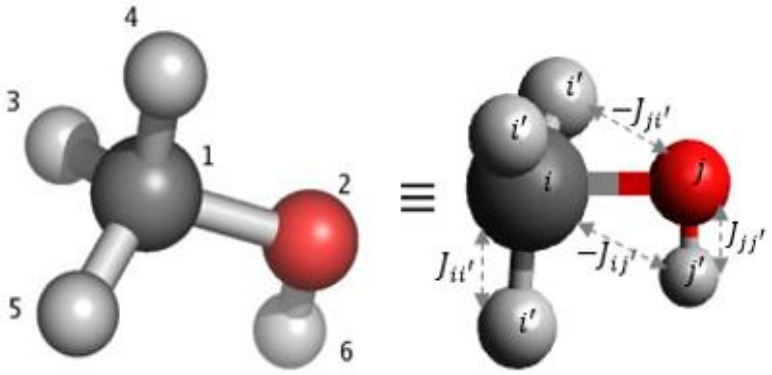

Figure A. 1: Schematic explanation of the Coulomb interaction between covalently bonded atoms in the split-charge equilibration scheme.

$$J_{ij} \equiv J_{ij}^{i'j'} = J_{ii'} - J_{ij'} - J_{ji'} + J_{jj'} \qquad \text{(A. 2.8)}$$

The electrochemical equilibrium in QEq is capture in Eq. (A1.9), which is the result of minimizing the potential energy equation (Eq. (A1.7)) of an atom. It trails from the electrochemical and/or chemical potential equalization requirement that:

$$\frac{\partial E_{QEq}}{\partial Q_i} - \frac{\partial E_{QEq}}{\partial Q_j} = 0 \tag{A. 2.9a}$$

The SQE equivalence of the equilibration condition requires that:

$$\frac{\partial E_{SQE}}{\partial q_{ij}} = 0 \tag{A. 2.9b}$$

Moreover, it is worth noting while applying Eq. (A2.9b) that

$$\frac{\partial Q_i}{\partial q_{jk}} = \delta_{ij} - \delta_{ik} \tag{A. 2.10}$$

provided the E_{QEq} and E_{SQE} correspond in form and relation while also abiding by the charge equilibration rules, Eqs. (A.2.6c).

Minimizing Eq. (A.2.5) with respect to a generic split-charge indexed $q_{kk'}$ leads to a system of $N-1$ independent linear equations in $N-1$ unknowns. For clarity, we present concisely detailed term by term minimization steps of Eq. (A.2.5). Using Eqs. (A.2.6b & A.2.8) and applying Eqs. (A.2.7, A.2.9b & A.2.10) to each term in Eq. (A.2.5), we explored the summations, for which $i=j=k, i=k\ \&\ j=k', \ i=k'\ \&\ j=k$ and $i=j=k'$ unless otherwise stated, and then, writing only the nonzero contributions to each term lead to:

$$\frac{\partial V_{\kappa^{(s)}}}{\partial q_{kk'}} = \frac{1}{2}\sum_{i,j}\kappa_{ij}^{(s)}\frac{\partial q_{ij}^2}{\partial q_{kk'}} = \frac{1}{2}\left(\kappa_{k'k}^{(s)}\frac{\partial q_{k'k}^2}{\partial q_{kk'}} + \kappa_{kk'}^{(s)}\frac{\partial q_{kk'}^2}{\partial q_{kk'}}\right) = 2\kappa_{kk'}^{(s)}q_{kk'} \tag{A. 2.11}$$

$$\frac{\partial V_{\bar{\chi}}}{\partial q_{kk'}} = \frac{1}{2}\sum_{i,j}\bar{\chi}_{ij}\frac{\partial q_{ij}}{\partial q_{kk'}} = \frac{1}{2}\left(\bar{\chi}_{kk'}\frac{\partial q_{kk'}}{\partial q_{kk'}} + \bar{\chi}_{k'k}\frac{\partial q_{k'k}}{\partial q_{kk'}}\right) = \bar{\chi}_{kk'} \tag{A. 2.12}$$

$$\frac{\partial V_{\kappa}}{\partial q_{kk'}} = \frac{1}{2}\sum_{i,j}\kappa_{ij}\frac{\partial\left(\bar{Q}_{ij}q_{ij}\right)}{\partial q_{kk'}} = \frac{1}{4}\sum_{i,j}\kappa_{ij}\left[\left(\frac{\partial Q_i}{\partial q_{kk'}} - \frac{\partial Q_j}{\partial q_{kk'}}\right)q_{ij} + \left(Q_i - Q_j\right)\frac{\partial q_{ij}}{\partial q_{kk'}}\right]$$

$$= \frac{1}{4}\sum_{i,j}\kappa_{ij}\left(\delta_{ik} - \delta_{ik'} - \delta_{jk} + \delta_{jk'}\right)q_{ij} + \frac{1}{4}\sum_{i,j}\kappa_{ij}\left(Q_i - Q_j\right)\frac{\partial q_{ij}}{\partial q_{kk'}}$$

$$= \frac{1}{4}\sum_{i}\left(\underbrace{2\kappa_{ik'}q_{ik'}}_{i=k\ \forall i\in\delta\text{ index},j=k'} - \underbrace{2\kappa_{ik}q_{ik}}_{i=k'\ \forall i\in\delta\text{ index},j=k}\right) + \frac{1}{4}\left(\kappa_{kk'}(Q_k - Q_{k'}) + \kappa_{k'k}(Q_k - Q_{k'})\right)$$

$$= \frac{1}{2}\sum_i (\kappa_{ik'} q_{ik'} - \kappa_{ik} q_{ik}) + \frac{1}{4}\sum_i \left((\kappa_{kk'} + \kappa_{k'k})\, q_{ki} - (\kappa_{kk'} + \kappa_{k'k}) q_{k'i} \right)$$

$$\frac{\partial V_{\bar{\kappa}}}{\partial q_{kk'}} = \frac{1}{2}\sum_{i,j} \bar{\kappa}_{ij} \frac{\partial (Q_{ij} q_{ij})}{\partial q_{kk'}} = \frac{1}{4}\sum_{i,j} \bar{\kappa}_{ij} \left[\left(\frac{\partial Q_i}{\partial q_{kk'}} + \frac{\partial Q_j}{\partial q_{kk'}} \right) q_{ij} + (Q_i + Q_j) \frac{\partial q_{ij}}{\partial q_{kk'}} \right]$$

$$= \frac{1}{4}\sum_{i,j} \bar{\kappa}_{ij} (\delta_{ik} - \delta_{ik'} + \delta_{jk} - \delta_{jk'}) q_{ij} + \frac{1}{4}\sum_{i,j} \bar{\kappa}_{ij} (Q_i + Q_j) \frac{\partial q_{ij}}{\partial q_{kk'}}$$

$$= \frac{1}{4}\sum_i \left(\underbrace{2\bar{\kappa}_{ik} q_{ik}}_{i=k \;\; \forall i \in \delta \text{ index}, j=k} - \underbrace{2\bar{\kappa}_{ik'} q_{ik'}}_{i=k' \;\; \forall i \in \delta \text{ index}, j=k'} \right) + \frac{1}{4} \left(\bar{\kappa}_{kk'} (Q_k + Q_{k'}) + \bar{\kappa}_{k'k} (Q_k - Q_{k'}) \right)$$

$$= \frac{1}{2}\sum_i (\bar{\kappa}_{ik} q_{ik} - \bar{\kappa}_{ik'} q_{ik'}) + \frac{1}{4}\sum_i \left((\bar{\kappa}_{kk'} + \bar{\kappa}_{k'k}) q_{ki} + (\bar{\kappa}_{kk'} - \bar{\kappa}_{k'k}) q_{k'i} \right)$$

$$\frac{\partial V_{\kappa}}{\partial q_{kk'}} + \frac{\partial V_{\bar{\kappa}}}{\partial q_{kk'}} = \frac{1}{2}\sum_i (-\kappa_{k'i} q_{k'i} + \kappa_{ki} q_{ki} + \bar{\kappa}_{ki} q_{ki} - \bar{\kappa}_{k'i} q_{k'i})$$

$$+ \frac{1}{2}\sum_i (\kappa_{kk'} q_{ki} - \kappa_{k'k} q_{k'i} + \bar{\kappa}_{kk'} q_{ki} - \bar{\kappa}_{k'k} q_{k'i})$$

$$= \frac{1}{2}\sum_i (\kappa_{kk'} + \bar{\kappa}_{kk'} + \kappa_{ki} + \bar{\kappa}_{ki}) q_{ki} - \frac{1}{2}\sum_i (\kappa_{k'k} + \bar{\kappa}_{k'k} + \kappa_{k'i} + \bar{\kappa}_{k'i}) q_{k'i} \quad \text{(A. 2.13)}$$

$$\frac{\partial V_C}{\partial q_{kk'}} = \frac{1}{2}\sum_{i<j} \left(\sum_{i',j'} \frac{\partial q_{i'j'}}{\partial q_{kk'}} J_{ij}^{i'j'} \right) q_{ij} = \frac{1}{2}\sum_{i<j} \left(\frac{\partial q_{kk'}}{\partial q_{kk'}} J_{ij}^{kk'} + \frac{\partial q_{k'k}}{\partial q_{kk'}} J_{ij}^{k'k} \right) q_{ij}$$

$$= \frac{1}{2}\sum_{i<j} (J_{ij}^{kk'} - J_{ij}^{k'k}) q_{ij} = \sum_{i<j} (J_{ik} - J_{ik'} - J_{jk} + J_{jk'}) q_{ij} \quad \text{(A. 2.14)}$$

Finally, the split-charge equation is obtained by substituting equations (A.2.11 – A.2.14) in Eq. (A.2.5).

$$-\bar{\chi}_{kk'} = 2\kappa_{kk'}^{(s)} q_{kk'} + \frac{1}{2}\sum_i^N (L_i q_{ki} - M_i q_{k'i}) + J_{kk'} \quad \text{(A. 2.15)}$$

$$L_i = (\kappa_{kk'} + \bar{\kappa}_{kk'} + \kappa_{ki} + \bar{\kappa}_{ki})$$

$$M_i = (\kappa_{k'k} + \bar{\kappa}_{k'k} + \kappa_{k'i} + \bar{\kappa}_{k'i})$$

$$J_{kk'} = \sum_i^N \sum_{j=i+1}^N (J_{ik} - J_{ik'} - J_{jk} + J_{jk'})\, q_{ij}$$

In addition to the anti/symmetry relations given in Eq. (A.2.7), we make a summary of the following rules and conditions, which are applicable in all SQE cases. Some of them were

applied during the energy minimization and were impactful in remedying the artifact of having a resultant net charge on the dissociated atoms or molecules separated at large distance.

1. $q_{ii} = \chi_{ii} = 0$, since q_{kk} and χ_{kk} are forbidden; charge flow from an atom to itself is not allowed.
2. $q_{ij} = \chi_{ij} = 0$, if i and j are not bonded and/or their bond is broken via short-distance cut-off.
3. $J_{ii} = J_{jj} = 0$, i.e., if any of the indices in $J_{kk'}$ summation terms are equal, that term is zero; this connote that no atom is allowed to interact with its own self.
4. $\forall\, i < j$ and $\forall\, k \neq k'$ (no atom transfers charge to itself) in the expansion of $J_{kk'}$ are cases, for which solutions are sought.

Though Eq. (A.2.15) can be formulated in similar matrix form and written in compact form as the QEq equation, it defers from QEq in *order* and element compositions:

$$\boldsymbol{A} \cdot \boldsymbol{q} = -\boldsymbol{b} \qquad \text{(A. 2.16)}$$

Here, $\boldsymbol{A}$ is a matrix of $m \times m$ order (where $m = N - 1 =$ the number of split-charges, nsq in a molecule) whose elements are sums of $\kappa_{kk'}^{(s)}$, L_i, M_i, and $J_{kk'}$ terms ($\kappa_{kk'}^{(s)}$ is actually a diagonal matrix). $\boldsymbol{q}$ and $\boldsymbol{b}$ are each m column vector for the split-charges and difference in atomic electronegativity, respectively. As an illustration, utilizing the conditions list above and Eq. (A.2.17), we explore Eq. (A.2.15) on Figure A.2.1 and write the resulting $N - 1$ equations after the order of E. (A.2.16) as follows.

$$\begin{pmatrix} 2\kappa_{12}^{s} + \frac{L_2 - M_1}{2} - J_{12} - J_{21} & \frac{L_3}{2} - J_{12} - J_{31} + J_{32} & \frac{L_4}{2} - J_{12} - J_{41} + J_{42} & \frac{L_5}{2} - J_{12} - J_{51} + J_{52} & \frac{M_6}{2} + J_{21} - J_{61} + J_{62} \\ \frac{L_2}{2} - J_{13} - J_{21} + J_{23} & 2\kappa_{13}^{s} + \frac{L_3 - M_1}{2} - J_{13} - J_{31} & \frac{L_4}{2} - J_{13} - J_{41} + J_{43} & \frac{L_5}{2} - J_{13} - J_{51} + J_{53} & J_{21} - J_{23} - J_{61} + J_{63} \\ \frac{L_2}{2} - J_{14} - J_{21} + J_{24} & \frac{L_3}{2} - J_{14} - J_{31} + J_{34} & 2\kappa_{14}^{s} + \frac{L_4 - M_1}{2} - J_{14} - J_{41} & \frac{L_5}{2} - J_{14} - J_{51} + J_{54} & J_{21} - J_{24} - J_{61} + J_{64} \\ \frac{L_2}{2} - J_{15} - J_{21} + J_{25} & \frac{L_2}{2} - J_{15} - J_{31} + J_{35} & \frac{L_4}{2} - J_{15} - J_{41} + J_{45} & 2\kappa_{15}^{s} + \frac{L_5 - M_1}{2} - J_{15} - J_{51} & J_{21} - J_{25} - J_{61} + J_{65} \\ \frac{-L_1}{2} + J_{12} - J_{16} + J_{26} & J_{12} - J_{16} - J_{32} + J_{36} & J_{12} - J_{16} - J_{42} + J_{46} & J_{12} - J_{16} - J_{52} + J_{56} & 2\kappa_{26}^{s} + \frac{L_6 - M_2}{2} - J_{26} - J_{62} \end{pmatrix} \begin{pmatrix} q_{12} \\ q_{13} \\ q_{14} \\ q_{15} \\ q_{26} \end{pmatrix}$$

$$= -\begin{pmatrix} \bar{\chi}_{12} \\ \bar{\chi}_{13} \\ \bar{\chi}_{14} \\ \bar{\chi}_{15} \\ \bar{\chi}_{26} \end{pmatrix} \qquad \text{(A. 2.17)}$$

With the SQE generalization of the QEq method, we expect individual molecules or isolated atoms to be electrically neutral since charges are only allowed to flow between bonded atoms. We observe from Eq. (A.2.17) that hardness terms that are non-diagonal in the index of atoms are included unlike in QEq where they are neglected. In this scheme, in which the QEq rules are obeyed, there are two parameters (χ_i and κ_i) per atom type and one parameter $\kappa_{ij}^{(s)}$ per bond. The bonding is also assumed to be well defined, i.e., only covalently bonded atoms are considered in determining the doubly indexed parameters.

A.3 Ewald summation for the Coulomb interaction energy

Our interest was to calculate the Coulomb contribution to the potential energy of N-particles in a system. This energy contribution is:

$$E_{Coul} = \frac{k_C}{2}\sum_{i=1}^{N} Q_i \Phi(r_i) \qquad \text{(A. 3.1)}$$

where $\Phi(r_i)$ electrostatic potential at the position of particle i.

$$\Phi(r_i) = \sum_{j,|n|}^{N,\infty}{}' \frac{Q_j}{|\boldsymbol{r}_{ij} + \boldsymbol{nl}|} \qquad \text{(A. 3.2)}$$

In the energy expression, atom i in a unit box of length l interacts with all other atoms j in the unit box and with all the image atoms in the periodic images L of the unit box. The prime symbol indicates that terms for $j = i$ do not count if $L = 0$. Then, sum this interaction over individual atoms in the unit box. In this treatment, the particles are under periodic boundary conditions, which three repeat vectors $\vec{a}_1, \vec{a}_2$, and $\vec{a}_3$ describe. That means, for particle i of charge Q_i located at $\vec{r}_i$, there are particles of the same Q_i located at $\vec{r}_i + n_1\vec{a}_1 + n_2\vec{a}_2 + n_3\vec{a}_3$. In a simplified notation, $n_1\vec{a}_1 + n_2\vec{a}_2 + n_3\vec{a}_3 = \boldsymbol{nl}$ with $|\vec{a}_1| = |\vec{a}_2| = |\vec{a}_3| = l$ for a cubic system and vector $\boldsymbol{n}$ equals simple cubic lattice (n_1, n_2, n_3) form arbitrary integers. Eq. (S2.1) converges poorly or conditionally and cannot be summed directly for point charges during simulation. Enhancing its convergence entails rewriting it. First, each point charge Q_i at $\vec{r}_i$ receives a special treatment of being smeared out with or surrounded by a Gaussian charge cloud (distribution) of opposite sign but equal magnitude as Q_i. An advantage here is that the electrostatic potential at point $\vec{r}_i$ due to the Gaussian charge distribution decays rapidly at an increasing distance; therefore, it is computed easily by direct summation in real space. However, it contains a singularity, implies that if two atoms are too close to each other in the central box, it could return nonphysical energy. We remedied this by modifying the real space

contribution with a shielding function when the interaction between atoms is in the central box. Second, because we are interested in the electrostatic potential of point charges, the assumed charge cloud needs to be removed. Therefore, a compensating or canceling Gaussian charge cloud of the same magnitude as the smeared charge cloud but has the opposite sign is allowed around each point charge to cancel out the smeared cloud. This compensating charge cloud appears as a smoothly varying function that is also periodic; thus, it is conveniently solvable in Fourier space. At this point, we have three contributions to the potential at point $\vec{r}_i$. (1) Contribution due to the point charge Q_i, (2) Contribution due to the Gaussian charge cloud with charge $-Q_i$, and (3) Contribution due to a compensating Gaussian charge cloud of charge Q_i. And another contribution is due to the self-interaction of item 3 with item 1 and must not count in the sum of the real- and Fourier-space contributions. Given the Gaussian charge distribution, the electrostatic potentials due to these charge distributions are solved more like solving the Poisson equation.

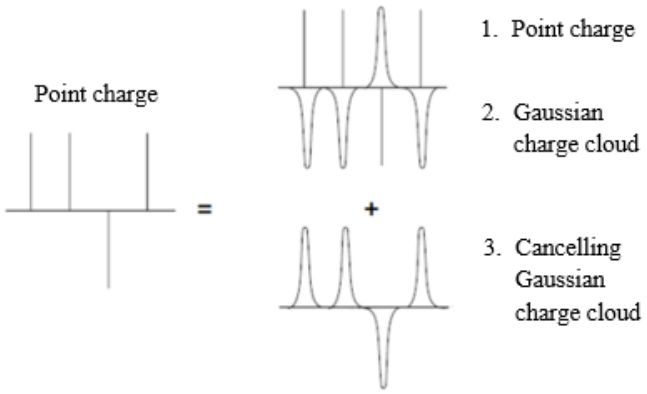

Figure A. 2: Charge distribution in Ewald sum, a set of point charges are considered a set of smeared Gaussian charges plus smoothly varying cancelling background charges that includes the self-interaction of the cancelling background charges with the set of point charges. See refs [102] and [133].

For particle i at r_i interacting with another particle j at r_j and the image particles so that $r_{ij} = \left|\vec{r}_{ij} + n_1\vec{a}_1 + n_2\vec{a}_2 + n_3\vec{a}_3\right|$, the results for these contributions to the energy are as follows.

The point charge contribution appears in real space as,

$$\Phi^{point}(r_i) = \frac{Q_j}{r_{ij}} \tag{A. 3.3}$$

For the Gaussian charge cloud solvable in real space,

$$\Phi^{\text{real}}(r_i) = -\frac{Q_j}{r_{ij}}\,\text{erf}\left(\zeta r_{ij}\right) \tag{A. 3.4}$$

Combining the contribution due to the point charge and smeared charge cloud gives a fast-decaying function (short-range part of the Ewald) in terms of a complementary error function as

$$\Phi^{sr}(r_i) = \frac{Q_j}{r_{ij}} - \frac{Q_j}{r_{ij}}\mathrm{erf}(\zeta r_{ij}) = \frac{Q_j}{r_{ij}}\mathrm{erfc}(\zeta r_{ij}) \qquad \text{(A. 3.5)}$$

Let L be the number of translated unit cells, for which the charge converges; then, summing the interaction over all particles and image cells will give Eq. (A.3.6) where $V_{sr}(r_{ij}) = erfc(\zeta \boldsymbol{r_{ij}})/\boldsymbol{r_{ij}}$.

$$E_{Coul}^{sr} = \sum_{i=1}^{N}\sum_{\substack{j=1 \\ j\neq i^*}}^{N} Q_i Q_j \sum_{n_1,n_2,n_3=-L}^{L} V_{sr}(r_{ij}) \qquad \text{(A. 3.6)}$$

Notice that we dropped the prime and replaced it with $j \neq i^*$ for ease of interpretation (see the paper). Correcting for orbital overlap or close-distance (CDC) implies Eq. (A.3.7) and $r_{ij}^{cdc} = \left(r_{ij}^3 + \gamma_{ij}^{-3}\right)^{1/3}$.

$$V_{sr}(r_{ij}) = \begin{cases} \dfrac{erfc(\zeta r_{ij}^{cdc})}{r_{ij}^{cdc}};\ n_1 = n_2 = n_3 = 0 \\ \dfrac{erfc(\zeta r_{ij})}{r_{ij}}; \qquad otherwise \end{cases} \qquad \text{(A. 3.7)}$$

For the canceling or compensating Gaussian charge cloud, the Fourier transform of the compensating Gaussian charge becomes eminent. The Fourier space distance between particle i and particle j in the unit box and any image particle is $h_{ij} = \left|\vec{h}_{ij} + m_1\vec{b}_1 + m_2\vec{b}_2 + m_3\vec{b}_3\right|$. $\left(\vec{b}_1, \vec{b}_2, \vec{b}_3\right)$ are the translational reciprocal lattice vectors and (m_1, m_2, m_3) are integer vectors describing the reciprocal lattice points.

$$\Phi^{Fourier}(r_i) = \frac{4\pi Q_j}{\mathrm{V}h_{ij}^2}\exp\left(i\vec{h}_{ij}\,.\,\vec{\mathrm{r}}_{ij}\right)\exp\left(-\frac{h_{ij}^2}{4\zeta^2}\right) \qquad \text{(A. 3.8)}$$

If the number of reciprocal space points considered equals the number of translated unit boxes, then the sum of the Fourier space contribution over all particles and their image will yield:

$$E_{Coul}^{lr} = \sum_{i=1}^{N}\sum_{\substack{j=1 \\ j\neq i^*}}^{N} Q_i Q_j \sum_{\mathrm{u,v,w}=-L}^{L} V_{lr}(h_{ij}) \qquad \text{(A. 3.9)}$$

Where $u = n_1 = m_1, v = n_2 = m_2$ and $w = n_3 = m_3$ are lattice point in real or reciprocal space since we assume the same number of points in the two spaces.

$$V_{lr}(h_{ij}) = \frac{4\pi}{\mathrm{V}h_{ij}^2}\exp(i\vec{h}_{ij}\,.\,\vec{\mathrm{r}}_{ij})\exp\left(-\frac{\mathrm{h}_{\mathrm{ij}}^2}{4\zeta^2}\right) \approx \left(\frac{4\pi}{\mathrm{V}}\right)\frac{cos(\vec{h}_{ij}\cdot\vec{r}_{ij})}{h_{ij}^2}\exp\left(-\frac{h_{ij}^2}{4\zeta^2}\right) \quad (\mathrm{A.3.10})$$

Because partial charges represent a real physical property of an atom, the concept of imaginary or complex values does not apply to charges, thus, the imaginary part (sine part) of Eq. (A.3.10) is dropped after its trigonometric expansion. The self-interaction contribution to the energy is $\Phi^{self} = \left(\frac{\zeta}{\sqrt{\pi}}\right)Q_i^2$ and the sum over all particles amounts to

$$E_{Coul}^{self} = \frac{\zeta}{\sqrt{\pi}}\sum_{i=1}^{N} Q_i^2 \quad (\mathrm{A.3.11})$$

The overall Ewald-modified-Coulomb energy becomes:

$$E_{Coul} = \frac{k_C}{2}\sum_{i=1}^{N}\sum_{\substack{j=1\\ j\neq i^*}}^{N} Q_iQ_j \sum_{\mathrm{u,v,w}=-L}^{L}\left(V_{sr}(r_{ij}) + V_{lr}(h_{ij})\right) - \frac{k_C\zeta}{\sqrt{\pi}}\sum_{i=1}^{N} Q_i^2 \quad (\mathrm{A.3.12})$$

Total energy of the system with Ewald-modified-Coulomb interaction potential is:

$$E(Q_1,\dots,Q_N) = \sum_{i=1}^{N}\left(E_i^0 + Q_i\chi_i^0 + \frac{1}{2}Q_i^2J_{ii}^0 + \frac{k_C}{2}\sum_{j\neq i^*}^{N} Q_iQ_j \sum_{u,v,w=-L}^{L}(V_{sr}+V_{lr}) - \frac{k_C\zeta}{\sqrt{\pi}}Q_i^2\right) \quad (A.3.13)$$

Like in QEq, the total energy (Eq. A.3.13) is differentiated as a function Q_i following Eq. (A.3.8) and the decomposition of $j \neq i^{\star}$ explained in the paper. The result is the same as QEq but only different in the matrix elements.

B. Appendix for chapter 5

Table B. 1**:** Average of the Absolute Difference (AAD) between EQeq and the Python source code charges demonstrating the similarity performance between our Python source code and EQeq.

MOF Compound	Metal	AAD (e)
Co-MOF	Co	0.0000
HKUST	Cu	0.0169
IRMOF-1	Zn	0.0003
IRMOF-3	Zn	0.0003
Mg-MOF	Mg	0.0004
MIL-47	V	0.0003
Ni-MOF74	Ni	0.0002
Pd-2-pymo	Pd	0.0029
UMCM-150	Cu	0.0021
UMCM-150N2	Cu	0.0007
ZIF	Zn	0.0143
Zn-MOF74	Zn	0.0007

B.1 Charge evolution with number of cells.

This checks the convergence of charge with number of cells (shells), or periodic images considered along each direction in both real and Fourier space. By "cell," we mean all translated copies of the central unit box defined in terms of integer multiples of a_1, a_2 and a_3 box length in x, y, and z directions respectively, whereas "shell' means concentric spheres with radii $\sqrt{\sum_{\Lambda=1}^{3}(n_\Lambda \vec{a}_\Lambda)^2}$. The charge is observed in Figure B.1 to have converged at a maximum translated unit box of $L = 2$. Increasing the periodic image boxes, the charge varies negligibly from the previous calculation.

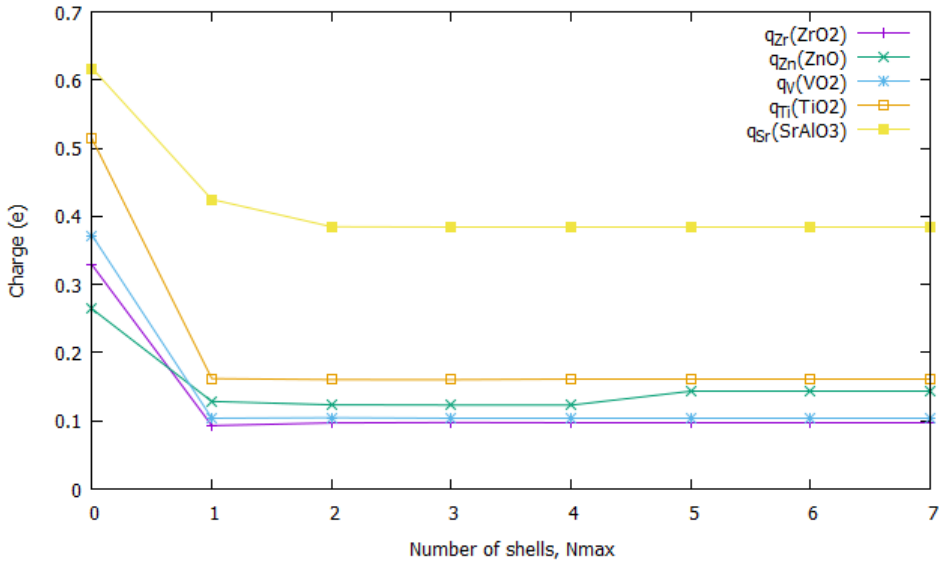

Figure B. 1: Charge as a function of number of cells for some test materials. This consolidates the convergence of charges at L = 2 considered in each direction.

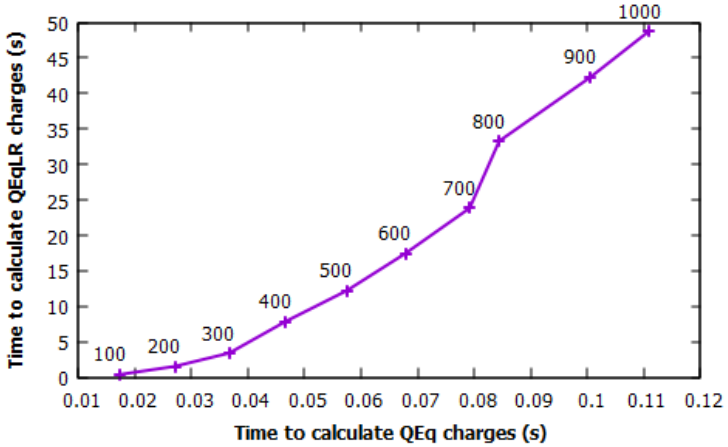

Figure B. 2: Plot of the time to calculate QEqLR charges in relation to time to calculate QEq charge. Data points represent the number of the SiO_2 atoms in a supercell.

It is not surprising the QEqLR is time consuming relative to QEq because all atomic pair interactions were sampled unlike in the QEq, which includes interactions only within 10Å distance around each atom.

Table B. 2: QEq net charge on the bottom electrode and the layers of the bottom electrode.

sep	BL1	BL2	BL3	BL4	BL5	BL6	BEnet
3.6	0.871	0.133	0.469	0.276	-0.325	1.862	3.286
5.6	0.895	0.124	0.376	0.371	-0.015	1.096	2.847
7.6	0.899	0.130	0.354	0.355	0.119	0.913	2.770
9.6	0.899	0.131	0.353	0.353	0.131	0.899	2.765
11.6	0.899	0.131	0.353	0.353	0.131	0.899	2.765
13.6	0.899	0.131	0.353	0.353	0.131	0.899	2.765
15.6	0.899	0.131	0.353	0.353	0.131	0.899	2.765
17.6	0.899	0.131	0.353	0.353	0.131	0.899	2.765
19.6	0.899	0.131	0.353	0.353	0.131	0.899	2.765
21.6	0.899	0.131	0.353	0.353	0.131	0.899	2.765
23.6	0.899	0.131	0.353	0.353	0.131	0.899	2.765
25.6	0.899	0.131	0.353	0.353	0.131	0.899	2.765
27.6	0.899	0.131	0.353	0.353	0.131	0.899	2.765
29.6	0.899	0.131	0.353	0.353	0.131	0.899	2.765
31.6	0.899	0.131	0.353	0.353	0.131	0.899	2.765
33.6	0.899	0.131	0.353	0.353	0.131	0.899	2.765
35.6	0.899	0.131	0.353	0.353	0.131	0.899	2.765
37.6	0.899	0.131	0.353	0.353	0.131	0.899	2.765
39.6	0.899	0.131	0.353	0.353	0.131	0.899	2.765

Table B. 3: QEqLR net charge on the bottom electrode and the layers of the bottom electrode.

sep	BL1	BL2	BL3	BL4	BL5	BL6	BEnet
3.6	-0.155	0.104	0.163	0.118	-0.113	2.493	2.610
5.6	-0.180	0.078	0.128	0.121	0.004	1.592	1.743
7.6	-0.190	0.055	0.099	0.106	0.038	1.231	1.340
9.6	-0.187	0.036	0.075	0.086	0.041	1.035	1.087
11.6	-0.175	0.021	0.055	0.067	0.033	0.902	0.904
13.6	-0.155	0.010	0.040	0.050	0.022	0.796	0.763
15.6	-0.130	0.001	0.028	0.037	0.011	0.704	0.651
17.6	-0.103	-0.005	0.019	0.027	0.003	0.623	0.562
19.6	-0.075	-0.010	0.012	0.018	-0.004	0.549	0.491
21.6	-0.047	-0.013	0.007	0.012	-0.009	0.484	0.435
23.6	-0.020	-0.014	0.004	0.008	-0.012	0.425	0.391
25.6	0.004	-0.015	0.002	0.005	-0.014	0.373	0.356
27.6	0.026	-0.014	0.001	0.003	-0.015	0.328	0.329
29.6	0.046	-0.014	0.001	0.002	-0.015	0.288	0.308
31.6	0.062	-0.012	0.001	0.002	-0.015	0.254	0.293
33.6	0.075	-0.011	0.002	0.002	-0.014	0.225	0.281
35.6	0.086	-0.009	0.003	0.003	-0.013	0.201	0.272
37.6	0.095	-0.007	0.004	0.004	-0.011	0.181	0.266
39.6	0.101	-0.006	0.005	0.005	-0.009	0.165	0.261

B.2 Debate on Choosing the Ewald splitting parameter.

In a computational implementation, several factors, such as system size, desired accuracy, CPU time in real- and reciprocal spaces, and cutoff distance, influence the choice of the Ewald

parameter. While [238] contains some suggested handy expressions for the Ewald splitting parameter, one of the best ways of selecting the Ewald parameter is by analyzing the error in the Coulomb potential energy or force calculation. But in practice, the Ewald splitting parameter is chosen from a set of tested values alongside the cutoff radius that is either $\leq l/2$ or assigned heuristically [137], [143], [239], [240]. Then, the lookout is a set of parameters with minimal error [137], [143] and the best correlation coefficient [239]. The values, which give the minimal (relative) root-mean-square error between theoretical and experimental results become the optimal Ewald parameter. In LAMMPS, the Ewald parameter is either user-specified (necessary for uncharged systems; see the kspace Ewald parameter in LAMMPS [37] documentary) or determined automatically through an expression that relates the parameter to the desired accuracy, cutoff, supercell size, and atomic charges. The requirement of particle charges makes the latter option unsuitable for partial charge calculation since the particle charges are unknown quantities to be determined. Intuitively, we can set the Ewald parameter to a value, for which the Ewald summation of the Coulomb energy yields the same total energy as the brute-force (direct) application of the Coulomb interaction. This step also requires full knowledge of the atoms' charges. We are unaware of any existing method that determines the Ewald splitting parameter with a focus on charge accuracy. All known methods for choosing the Ewald splitting parameter, the real- and Fourier space cutoffs trade on efficiency and accuracy. For example, in the traditional energy or force application, changing the Ewald splitting parameter means shifting the computational burden between real and reciprocal space, which implies we must also change the cutoff accordingly to maintain the same level of accuracy in energy and force calculations. Let us be clear here, Ewald implemented in LAMMPS is particularly for Coulomb energy and force and not for charge estimation. Energy and force computations require an *ab initio* supply of charges or at least a technique that determines the charge distributions should the atoms in the system be zero charged, the case, for which the Ewald parameter is user-specified. So, when we change the Ewald parameter in QEqLR, we are not shifting the computational burden between real and reciprocal space only but also toggle between the two spaces' contributions to the interaction functions in Eq (4.37) to obtain a match to the DFT method. The accuracy is fundamentally the (relative) root-mean-square difference between the direct Coulomb energy or force and the result from the Ewald summation, as is done in [143]. Extending this approach to charge calculation becomes expedient and implies that we need to state a referable standard method of determining charges. But it becomes densely challenging since charge estimation has no one best procedure for all purposes, coupled with the fact that atomic charges are not well-defined and measurable

quantum-mechanical observable. So, we user-specify the Ewald parameter by trial and error and scan through a small range to find the values that best fit the grid-based DFT Bader charges. It is, therefore, desirable in any application to optimize the Ewald parameter to improve QEqLR charges against any chosen ab initio method, with which one intends to compare results. This is the advantage of classical molecular dynamics; we try to mimic experiment or DFT so we could apply the methods on a larger system. Such optimization requires a mini-system of 5 – 10 atoms and takes almost zero seconds to complete. We found that the QEqLR yields reasonable charge both quantitatively and in polarity if the Ewald parameter is within $0 < \zeta < 0.5$ outside, which we obtain abominable charge values.

Table B. 4: Data for MIL-74 MOF compound

					Charge (e)		
Id	Atom	x	y	z	REPEAT	QEqLE	Qeq
1	C	3.2596	2.2051	8.8276	0.634	0.358	-0.057
2	C	0.1493	13.9379	1.8581	0.634	0.358	0.017
3	C	3.5583	10.2766	5.1114	0.634	0.358	-0.072
4	C	6.6686	5.8664	12.0809	0.635	0.358	0.009
5	C	3.5583	13.9379	5.1114	0.635	0.358	-0.057
6	C	6.6686	2.2051	12.0809	0.635	0.358	0.017
7	C	3.2596	5.8664	8.8276	0.635	0.358	-0.072
8	C	0.1493	10.2766	1.8581	0.635	0.358	0.009
9	C	3.3483	1.0477	7.8755	0.004	-0.01	0.079
10	C	0.0607	15.0953	0.906	0.004	-0.01	0.045
11	C	3.4696	9.1192	6.0635	0.004	-0.01	0.149
12	C	6.7572	7.0238	13.033	0.004	-0.01	0.047
13	C	3.4696	15.0953	6.0635	0.004	-0.01	0.079
14	C	6.7572	1.0477	13.033	0.004	-0.01	0.045
15	C	3.3483	7.0238	7.8755	0.004	-0.01	0.149
16	C	0.0607	9.1192	0.906	0.004	-0.01	0.047
17	C	2.1988	0.5311	7.3333	-0.143	-0.075	-0.016
18	C	4.5509	0.5214	7.4838	-0.128	-0.075	-0.003
19	C	1.2102	15.6119	0.3638	-0.143	-0.075	-0.018
20	C	5.6759	15.6216	0.5143	-0.128	-0.075	0.02
21	C	4.6191	8.6026	6.6057	-0.143	-0.075	0.029
22	C	2.267	8.5929	6.4552	-0.128	-0.075	0.026
23	C	5.6077	7.5404	13.5752	-0.143	-0.075	-0.011
24	C	1.142	7.5501	13.4247	-0.128	-0.075	0.013
25	C	4.6191	15.6119	6.6057	-0.143	-0.075	-0.016
26	C	2.267	15.6216	6.4552	-0.128	-0.075	-0.003
27	C	5.6077	0.5311	13.5752	-0.143	-0.075	-0.018
28	C	1.142	0.5214	13.4247	-0.128	-0.075	0.02
29	C	2.1988	7.5404	7.3333	-0.143	-0.075	0.029
30	C	4.5509	7.5501	7.4838	-0.128	-0.075	0.026
31	C	1.2102	8.6026	0.3638	-0.143	-0.075	-0.011
32	C	5.6759	8.5929	0.5143	-0.128	-0.075	0.013

33	H	1.3738	0.8943	7.5619	0.153	0.111	0.098
34	H	5.3384	0.8846	7.8212	0.133	0.118	0.131
35	H	2.0351	15.2487	0.5924	0.153	0.111	0.095
36	H	4.8884	15.2584	0.8517	0.133	0.118	0.089
37	H	5.4441	8.9658	6.3771	0.153	0.111	0.133
38	H	1.4795	8.9561	6.1178	0.133	0.118	0.152
39	H	4.7828	7.1772	13.3466	0.153	0.111	0.103
40	H	1.9295	7.1869	13.0873	0.133	0.118	0.081
41	H	5.4441	15.2487	6.3771	0.153	0.111	0.098
42	H	1.4795	15.2584	6.1178	0.133	0.118	0.131
43	H	4.7828	0.8943	13.3466	0.153	0.111	0.095
44	H	1.9295	0.8846	13.0873	0.133	0.118	0.089
45	H	1.3738	7.1772	7.5619	0.153	0.111	0.133
46	H	5.3384	7.1869	7.8212	0.133	0.118	0.152
47	H	2.0351	8.9658	0.5924	0.153	0.111	0.103
48	H	4.8884	8.9561	0.8517	0.133	0.118	0.081
49	O	6.6481	4.0357	9.6402	-0.597	-0.605	-0.084
50	O	3.5787	12.1073	2.6707	-0.597	-0.605	-0.245
51	O	0.1698	12.1073	4.2988	-0.597	-0.605	-0.084
52	O	3.2392	4.0357	11.2683	-0.597	-0.605	-0.245
53	O	2.1258	2.6345	9.137	-0.587	-0.499	-0.151
54	O	0.9647	2.6249	11.6182	-0.553	-0.487	-0.083
55	O	1.2831	13.5085	2.1675	-0.587	-0.499	-0.15
56	O	2.4442	13.5181	4.6487	-0.553	-0.487	-0.212
57	O	4.6921	10.706	4.802	-0.587	-0.499	-0.175
58	O	5.8532	10.6964	2.3208	-0.553	-0.487	-0.095
59	O	5.5348	5.437	11.7715	-0.587	-0.499	-0.162
60	O	4.3737	5.4466	9.2903	-0.553	-0.487	-0.235
61	O	4.6921	13.5085	4.802	-0.587	-0.499	-0.151
62	O	5.8532	13.5181	2.3208	-0.553	-0.487	-0.083
63	O	5.5348	2.6345	11.7715	-0.587	-0.499	-0.15
64	O	4.3737	2.6249	9.2903	-0.553	-0.487	-0.212
65	O	2.1258	5.437	9.137	-0.587	-0.499	-0.175
66	O	0.9647	5.4466	11.6182	-0.553	-0.487	-0.095
67	O	1.2831	10.706	2.1675	-0.587	-0.499	-0.162
68	O	2.4442	10.6964	4.6487	-0.553	-0.487	-0.235
69	V	1.3649	4.0357	10.3032	1.569	1.719	0.237
70	V	2.044	12.1073	3.3337	1.57	1.719	0.219
71	V	5.453	12.1073	3.6358	1.57	1.719	0.237
72	V	4.7739	4.0357	10.6053	1.57	1.719	0.219

Supercell info		
6.8179	16.143	13.939
90	90	90

References.

[1] C. Liu, Z. G. Neale, and G. Cao, “Understanding electrochemical potentials of cathode materials in rechargeable batteries,” *Materials Today*, vol. 19, no. 2, pp. 109–123, 2016.

[2] B. Dunn, H. Kamath, and J.-M. Tarascon, “Electrical energy storage for the grid: a battery of choices,” *Science*, vol. 334, no. 6058, pp. 928–935, 2011.

[3] I. Valov, R. Waser, J. R. Jameson, and M. N. Kozicki, “Electrochemical metallization memories—fundamentals, applications, prospects,” *Nanotechnology*, vol. 22, no. 25, p. 254003, 2011

[4] W. Lu, and C. M. Lieber, "Nanoelectronics from the bottom up." *Nature materials*, vol. 6, no. 11, pp. pp. 137-146, 2010.

[5] Y. Yang, P. Gao, S. Gaba, T. Chang, X. Pan, and W. Lu, “Observation of conducting filament growth in nanoscale resistive memories,” *Nature Communications*, vol. 3, no. 1, pp. 1 – 8, 2012.

[6] S. H. Jo, T. Chang, I. Ebong, B. B. Bhadviya, P. Mazumder, and W. Lu, “Nanoscale memristor device as synapse in neuromorphic systems,” *Nano letters*, vol. 10, no. 4, pp.1297 – 1301, 2010.

[7] N. Liu, R. Chen, and Q. Wan, “Recent Advances in Electric-Double Layer Transistors for Bio-Chemical Sensing Applications,” *Sensors*, vol. 19, no. 15, p. 3425, 2019.

[8] N. Onofrio, D. Guzman, and A. Strachan, “Atomistic simulation of electrochemical metallization cells: mechanisms of the ultra-fast resistance switching in nanoscale,” *Nanoscale*, vol. 8, no. 29, pp. 14037 – 14047, 2016.

[9] H. T. Yuan, H. Shimotani, J. T. Ye, S. Yoon, H. Aliah, A. Tsukazaki, M. Kawasaki, and Y. Iwasa, “Electrostatic and electrochemical nature of liquid-gated electric-double-layer transistors based on oxide semiconductors,” *J. Am. Chem. Soc.*, vol. 132, no. 51, pp. 18402 – 18407, 2010.

[10] J. Jiang, Q. Wan, J. Sun, and A. Lu, “Ultralow-voltage transparent electric-double-layer thin-film transistors processed at room-temperature,” *Appl. Phys. Lett.*, vol. 95, no. 15, p. 152114, 2009.

[11] N. Kang, Y. Lin, L. Yang, D. Lu, J. Xiao, Y. Qi, and M. Cai, “Cathode porosity is a missing key parameter to optimize lithium-sulfur battery energy density,” *Nature Communications*, vol. 10, no. 1, pp. 1 – 10, 2019.

[12] D. Y. W. Yu, K. Donoue, T. Inoue, M. Fujimoto, and S. Fujitani, “Effect of electrode parameters on LiFePO4 cathodes,” *J. Electrochem. Soc.*, vol. 153, no. 8, pp. A835 – A839, 2007.

[13] H. H. Zheng, J. Li, X. Y. Song, G. Liu, and V. S. Battaglia, “A comprehensive understanding of electrode thickness effects on the electrochemical performances of Li-ion battery cathodes,” *Electrochimica Acta.*, vol. 71, pp. 258 – 265, 2012.

[14] M. Doyle, J. Newman, A. S. Gozdz, C. N. Schmutz, and J. M. Tarascon, “Comparison of modeling predictions with experimental data from plastic lithium-ion cells,” *J. Electrochem. Soc.*, vol. 143, no. 6, pp. 1890 – 1903, 1996.

[15] R. Tian, S.-H. Park, P. J. King, G. Cunningham, J. Coelho, V. Nicolosi, and J. N. Coleman, "Quantifying the factors limiting rate performance in battery electrodes," *Nature Communications*, vol. 10, no. 1, pp. 1 – 11, 2019.

[16] C. Schindler, G. Staikov, and R. Waser, "Electrode kinetics of Cu-SiO2-based resistive switching cells: Overcoming the voltage-time dilemma of electrochemical metallization memories," *Appl. Phys. Lett.*, vol. 94, no. 7, p. 072109, 2009.

[17] G. Wu, H. Zhang, J. Zhou, A. Huang, and Q. Wan, "Proton conducting zeolite films for low-voltage oxide-based electric-double-layer thin-film transistors and logic gates," *Journal of Materials Chemistry C*, vol. 1, no. 36, pp. 5669, 2013.

[18] N. Onofrio, D. Guzman, and A. Strachan, "The atomic origin of the ultrafast resistance switching in nanoscale electrometallization cells," *Nat Matter*. Vol. 14, no. 4, pp. 440 – 446, 2015.

[19] M. Cibis, W. V. Potters, F. J. Gijsen, H. Marquering, P. van Ooij, E. vanBavel, … A. J. Nederveen, "The effect of spatial and temporal resolution of cine phase contrast MRI on wall shear stress and oscillatory shear index assessment," *PLOS ONE*, vol. 11, no. 9, p. e0163316, 2016.

[20] M. R. Armstrong, K. Boyden, N. D. Browning, G. H. Campbell, J. D. Colvin, W. J. DeHope, … B. R. Torralva, "Practical considerations for high spatial and temporal resolution dynamic transmission electron microscopy," *Ultramicroscopy*, vol. 107, no. 4-5, pp. 356 – 367, 2007.

[21] U. Celano, L. Goux, A. Belmonte, K. Opsomer, A. Franquet, A. Schulze, C. Detavernier, O. Richard, H, Bender, M. Jurczak, and W. Vandervorst, "Three-Dimensional Observation of the Conductive Filament in Nanoscaled Resistive Memory Devices," *Nano Letters*, vol. 14, no 5, pp. 2401–2406, 2014.

[22] M. Lanza, H. S. P. Wong, E. Pop, D. Ielmini, D. Strukov, B. C. Regan, L. Larcher, M. A. Villena, J. J. Yang, L. Goux, and A. Belmonte, "Recommended methods to study resistive switching devices," *Advanced Electronic Materials*, vol. 5, no. 1, p.1800143, 2019.

[23] Y. Chen, "ReRAM: History, Status, and Future," *IEEE Transactions on Electron Devices*, vol. 67, no 4, pp. 1420 – 1433, 2020.

[24] J. Tersoff, "Modeling solid-state chemistry: interatomic potentials for multicomponent systems," *Phys. Rev. B: Condens. Matter*, vol. 39, no. 8, p. 5566, 1989.

[25] D. L. Mobley, E. Dumont, J. D. Chodera, and K. A. Dill, "Comparison of Charge Models for Fixed-Charge Force Fields: Small Molecule Hydration Free Energies in Explicit Solvent," *J. Phys. Chem B*, vol. 111, no. 9, pp. 2242 – 2254, 2007.

[26] T. C. O'Connor, J. Andzelm, and M. O. Robbins, "AIREBO-M: A reactive model for hydrocarbons at extreme pressures," *J. Chem. Phys.*, vol. 142, no. 2, p. 024903, 2015.

[27] S. J. Stuart, A. B. Tutein, and J. A. Harrison, "A reactive potential for hydrocarbons with intermolecular interactions," *J. Chem. Phys.*, vol. 112, no. 14, pp. 6472 – 6486, 2000.

[28] A. C. Van Duin, S. Dasgupta, F. Lorant, and W. A. Goddard III, "ReaxFF: a reactive force field for hydrocarbons. *The Journal of Physical Chemistry A*, vol. 105, no. 41, pp. 9396 – 9409, 2001

[29] A. K. Rappe, and W. A. Goddard III, "Charge equilibration for molecular dynamics simulations," *J. Phys. Chem.*, vol. 95, no. 8, pp. 3358 – 3363, 1991.

[30] D. Ceperely, "Problem of long-range forces in the computer simulation of condensed media," *California Univ., Berkeley*. Lawrence Berkeley Lab., No. LBL-10634, CONF-800127, 1980.

[31] S. Ambrogio, B. Magyari-Kope. N. Onofrio, M. M. Islam, D. Duncan, Y. Nishi, and A. Strachan, "Modeling resistive switching materials and devices across scales," *J. Electroceram*, vol. 39, no. 1-4, pp. 39 – 60, 2017.

[32] M. Lübben, S. Menzel, S. G. Park, M. Yang, R. Waser, and I. Valov, "SET kinetics of electrochemical metallization cells: influence of counter-electrodes in SiO2/Ag based systems," *Nanotechnology*, vol. 28, no. 13, p. 135205, 2017.

[33] B. Kang, and G. Ceder, "Battery materials for ultrafast charging and discharging," *Nature*, vol. 458, no. 7235, pp. 190 – 193, 2009.

[34] E. R. Logan, E. M. Tonita, K. L. Gering, J. Li, X. Ma, L. Y. Beaulieu, and J. R. Dahn, "A study of the physical properties of Li-ion battery electrolytes containing esters," *J. Electrochem. Soc*., vol. 165, no. 2, pp. A21 – A30, 2018.

[35] J. Costard, M. Ender, M. Weiss, and E. Ivers-Tiffée, "Three-Electrode Setups for Lithium-Ion Batteries," *Journal of The Electrochemical Society,* vol. 164, no. 2, pp. A80 – A87, 2016.

[36] S. Tappertzhofen, I. Valov, and R. Waser, "Quantum conductance and switching kinetics of AgI-based microcrossbar cells," *Nanotechnology*, vol. *23, no.* 14, p. 145703, 2012.

[37] LAMMPS – "A flexible simulation tool for particle-based materials modelling at the atomic, meso, and continuum scales," *Comp. Phys. Comm*. 271, 108171, 2022.

[38] R. A. Nistor, J. G. Polihronov, M. H. Müser, and N. J. Mosey, "A generalization of the charge equilibration method for nonmetallic materials," *The Journal of Chemical Physics*, vol. 125, no. 9, p. 094108, 2006.

[39] P. P. Ewald, "Die Berechnung optischer und elektrostatischer Gitterpotentiale," *Annalen der physik*, vol. 369, no. 3, pp. 253-287, 1921.

[40] D. Linden, and T. B. Reddy (Eds), "Handbook of batteries," *McGill-Hill*., New York, 2001.

[41] J. B. Goodenough, "The Li-ion rechargeable battery: a perspective," *Journal of the American Chemical Society*, vol. 135, no. 4, pp: 1167 – 1176, 2013.

[42] S. Yayathi, W. Walker, D. Doughty, and H. Ardebili, "Energy distribution exhibited during thermal runaway of commercial lithium-ion batteries used for human spaceflight application," *J. Power Source*, vol. 329, pp. 197 – 206, 2016.

[43] J. B. Goodenough, "Rechargeable batteries: challenges old and new," *Journal of Solid-State Electrochemistry*, vol. 16, no. 6, pp: 2019 – 2029, 2012.

[44] F. Hui, C. Wen, S. Chen, E. Koren, R. Dechter, D. Lewis, and M. Lanza, "Emerging Scanning Probe–Based Setups for Advanced Nanoelectronic Research" *Advanced Functional Materials*, p.1902776, 2019

[45] J. K. Nørskov, F. Abild-Pedersen, F. Studt, and T. Bligaard, "Density functional theory in surface chemistry and catalysis," *Proceedings of the National Academy of Sciences,* vol. 108, no. 3, pp. 937 – 943, 2011.

[46] R. L. Gieseking, M. A. Ratner, and G. C. Schatz, "Benchmarking semi–empirical methods to compute electrochemical formal potentials," *J.Phys. Chem. A,* vol. 122, no. 33, pp. 6809 – 6818, 2018.

[47] L. E. Roy, E. Jakubikova, M. G. Guthrie, and E. R Batista, "Calculation of One-Electron Redox Potentials Revisited. Is It Possible to Calculate Accurate Potentials with Density Functional Methods?" *J.Phys. Chem. A,* vol. 113, no. 24, pp. 6745 – 6750, 2009.

[48] M. H. Hansen, L.-A. Stern, L. Feng, J. Rossmeisl, and X. Hu, "Widely Available Active Sites on Ni2P for Electrochemical Hydrogen Evolution–Insights from First Principles Calculations," *Phys. Chem. Chem. Phys*., vol. 17, no. 16, pp. 10823−10829, 2015.

[49] R. R. Nazmutdinov, M. D. Bronshtein, T. T. Zinkicheva, and D.V. Glukhov, "Modeling of Electron Transfer across Electrochemical Interfaces: State-of-the Art and Challenges for Quantum and Computational Chemistry," *Int. J. Quantum Chem.*, vol. 116, no. 3, pp. 189−201, 2016.

[50] L. D. Chen, M. Urushihara, K. Chan, and J. K. Nørskov, "Electric Field Effects in Electrochemical CO2 Reduction," *ACS Catal*., vol. 6, no. 10, pp. 7133−7139, 2016.

[51] E. J. Cairns, and P. Albertus, "Batteries for Electric and Hybrid-Electric Vehicles," *Annu. Rev. Chem. Biomol. Eng.*, vol. 1, no. 1, pp. 299 – 20, 2010.

[52] A. Eftekhari, "Lithium-ion Batteries with High Rate Capabilities," *ACS Sustainable Chemistry & Engineering*, vol. 5, no. 4, pp. 2799 – 2816, 2018.

[53] T. Tanimura, H. Tajima, A. Ogino, Y. Miyamoto, T. Kadoya, T. Komino, T. Yokomatsu, K. Maenaka, and Y. Ikemoto, "Accumulated charge measurement using a substrate with a restricted-bottom-electrode structure," *Organic Electronics*, vol. 74, pp. 251 – 257, 2019.

[54] B.-H. Guo, G. Y. Sun, G. Q. Su, J. Y. Xue, B. P. Song, and G. J. Zhang, "The mechanism of surface charge accumulation on alumina ceramics under impulse voltage in vacuum," In *2018 12th International Conference on the Properties and Applications of Dielectric Materials (ICPADM)*, pp. 1114-1118, IEEE, 2018.

[55] A. Yoshino, "The birth of the lithium-ion battery," *Angewandte Chemie International Edition*, vol. 51, no. 24, pp. 5798 – 5800, 2012.

[56] A. Groß, "Fundamental challenges for modeling electrochemical energy storage systems at the atomic scale." In Modeling Electrochemical Energy Storage at the Atomic Scale, pp. 1 – 22, *Springer*, Cham, 2018.

[57] O. Toprakci, H. A. K. Toprakci, L. Ji, and X. Zhang, "Fabrication and electrochemical characteristics of LiFePO4 powders for lithium-ion batteries," *KONA Powder and Particle Journal*, vol. 28, pp. 50 – 73, 2010.

[58] W. Du, A. Gupta, X. Zhang, A. M. Sastry, and W. Shyy, "Effect of cycling rate, particle size and transport properties on lithium-ion cathode performance," *International Journal of Heat and Mass Transfer*, vol. 53, nos. 17 – 18, pp. 3552 – 3561, 2010.

[59] M. R. Jongerden, and B. R. Haverkort, “Which battery model to use?” *IET software*, vol. 3, no. 6, pp. 445 – 457, 2009.

[60] K. Fujii, M. Matsugami, K. Ueno, K. Ohara, M. Sogawa, T. Utsunomiya, and M. Morita, “Long-Range Ion-Ordering in Salt-Concentrated Lithium-Ion Battery Electrolytes: A Combined High-Energy X-ray Total Scattering and Molecular Dynamics Simulation Study,” *The Journal of Physical Chemistry C*, vol. 121, no. 41, pp. 22720-22726, 2017.

[61] B. Hess, C. Kutzner, D. van der Spoel, and E. Lindahl, “Gromacs 4: Algorithms for Highly Efficient, Load-Balanced, and Scalable Molecular Simulation,” *J. Chem. Theory Comput*, vol. 4, pp. 435−447, 2008.

[62] E. Fortunato, P. Barquinha, and R. Martins, “Oxide semiconductor thin-film transistors: a review of recent advances,” *Advanced materials*, vol. 24, no. 22, pp. 2945 – 2986, 2012,

[63] F. Schwierz, “Graphene transistors,” *Nature nanotechnology*, vol. 5, no. 7, p. 487, 2010.

[64] D. M. Heyes, “Pressure tensor of partial-charge and point-dipole lattices with bulk and surface geometries,” *Physical Review B*, vol. 49, no. 2, pp. 755–764, 1994.

[65] T. Fujimoto, and K. Awaga, “Electric-double-layer field-effect transistors with ionic liquids,” *Physical Chemistry Chemical Physics*, vol. 15, no. 23, p. 8983, 2013.

[66] P. Simon, and Y. Gogotsi, “Materials for electrochemical capacitors,” In *Nanoscience and technology: a collection of reviews from Nature journals*, pp. 320-329, 2010.

[67] E. J. Cairns, and P. Albertus, “Batteries for Electric and Hybrid-Electric Vehicles,” *Annu. Rev. Chem. Biomol. Eng.*, vol. 1, no. 1, pp. 299 – 20, 2010.

[68] B. E. Conway, “Electrochemical supercapacitors: scientific fundamentals and technological applications,” *Springer Science & Business Media*. 2013.

[69] D. Myers, “Surfaces, interfaces, and colloids,” *New York etc.: Wiley-Vch*, vol. 358, pp. 79 – 96, 1999.

[70] R. Parsons, “The electrical double layer: recent experimental and theoretical developments,” *Chemical Reviews*, vol. 90, no. 5, pp. 813 – 826, 1990.

[71] H. von. Helmholtz, "Ueber einige Gesetze der Vertheilung elektrischer Ströme in körperlichen Leitern, mit Anwendung auf die thierisch-elektrischen Versuche (Schluss.)," *Annalen der Physik*, vol. 165, no. 7, pp. 353 – 377, 1853.

[72] M. Gouy, “Sur la constitution de la charge electrique a la surface d'un electrolyte,” *J. Phys. Radium*, pp. 457 – 468, 1910.

[73] D. L. Chapman, “LI A contribution to the theory of electrocapillarity,” *The London, Edinburgh, and Dublin philosophical magazine and journal of science*, vol. 25, no. 148, pp. 475 – 481, 1913.

[74] O. Stern, “The theory of the electrolytic double-layer,” *Z. Elektrochem*, vol. 30, no. 508, pp. 1014 – 1020, 1924.

[75] L. L. Zhang, and X. S. Zhao, “Carbon-based materials as supercapacitor electrodes,” *Chem. Soc. Rev.*, vol. 38, no. 9, pp. 2520 – 2531, 2009.

[76] A. D. Graves, "The electrical double layer in molten salts: Part 1. The potential of zero charge." *Journal of Electroanalytical Chemistry and Interfacial Electrochemistry* vol. 25, no. 3, pp. 349 – 35, 1970.

[77] A. D. Graves, and D. Inman, "The electrical double layer in molten salts: Part 2. The double-layer capacitance," *Journal of Electroanalytical Chemistry and Interfacial Electrochemistry* vol. 25, no. 3, pp. 357 – 372, 1970.

[78] C. Aliaga, C. S. Santos, and S. Baldelli, "Surface chemistry of room-temperature ionic liquids," *Physical Chemistry Chemical Physics*, vol. 9, no. 28, pp. 3683 – 3700, 2007.

[79] P. Snapp, J. M. Kim, C. Cho, J. Leem, M. F. Haque, and S. Nam, "Interaction of 2D materials with liquids: wettability, electrochemical properties, friction, and emerging directions," *NPG Asia Materials*, vol. 12, no. 1, pp. 1 – 16, 2020.

[80] S. Kondrat, C. Pe´rez, V. Presser, Y. Gogotsi and A. Kornyshev, "Effect of pore size and its dispersity on the energy storage in nanoporous supercapacitors," *Energy & Environmental Science*, vol. 5, no. 4, pp. 6474 – 6479, 2012.

[81] P. M. Biesheuvel, S. Porada, M. Levi, and M. Z. Bazant, "Attractive forces in microporous carbon electrodes for capacitive deionization," *Journal of solid state electrochemistry*, vol. 18, no. 5, pp. 1365–1376, 2014.

[82] J. Chmiola, G. Yushin, Y. Gogotsi, C. Portet, P. Simon and P.-L. Taberna, "Anomalous increase in carbon capacitance at pore size less than 1 nanometer," *Science*, vol. 313, no. 5794, pp. 1760–1763, 2006.

[83] J. Huang, B. G. Sumpter, and V. Meunier, "A universal model for nanoporous carbon supercapacitors applicable to diverse pore regimes, carbon materials, and electrolytes," *Chemistry–A European Journal*, vol. 14, no. 22, pp. 6614 – 6626, 2008.

[84] R. Burt, G. Birkett, and X. S. Zhao, "A review of molecular modelling of electric double layer capacitors," *Physical Chemistry Chemical Physics*, vol. 16, no. 14, pp. 6519 – 6538, 2014.

[85] P. J. Basser, and A. J. Grodzinsky, "The Donnan model derived from microstructure," *Biophysical chemistry*, vol. 46, no. 1, pp. 57–68, 1993.

[86] G. Jeanmairet, B. Rotenberg, D. Borgis, and M. Salanne, "Study of a water-graphene capacitor with molecular density functional theory," *The Journal of Chemical Physics*, vol. 151, no. 12, p. 124111, 2019.

[87] D. Ielmini, and R. Waser, "Resistive switching: from fundamental of nanoionics redox processes to memristive device applications," *Wiley-VCH Book*, ISBN: 978-3-527-33417-9, Wiley-VCH, Weinheim, Germany 2016.

[88] W. Lu, K.-H. Kim, T. Chang, and S. Gaba, "Two-terminal resistive switches (memristors) for memory and logic applications," in *Proceedings of the 16th Asia and South Pacific Design Automation Conference*, 2011, pp. 217-223: IEEE Press.

[89] S. Shirinzadeh, and R. Drechsler, "In-Memory Computing: The Integration of Storage and Processing," in Information Storage *Springer, Cham*, pp. 79 – 110, 2020.

[90] H. S. Yoon, I. G. Baek, J. Zhao, H., Sim, M. Y. Park, H. Lee, G. H. Oh, J. C. Shin, I. S. Yeo, and U. I. Chung, "Vertical cross-point resistance change memory for ultra-high-

density non-volatile memory applications," in *Proc. Symp. VLSI Technol.*, 2009, pp. 26–27.

[91] D. M. Guzman, N. Onofrio, and A. Strachan, "Stability and migration of small copper cluster in amorphous dielectrics," *Journal of Applied Physics*, vol. 177, no. 19, p. 195702, 2015.

[92] R. G. Parr, and W. Yang, "Density functional approach to the frontier-electron theory of chemical reactivity." *Journal of the American Chemical Society*, vol. 106, no. 14, pp. 4049-4050, 1984.

[93] P. Hohenberg, and W. Kohn, "Inhomogeneous Electron Gas." *Physical Review*, vol. 136, no. 3B, pp. B864–B871, 1964.

[94] Y. A. Wang, and E. A. Carter, "Orbital-Free Kinetic-Energy Density Functional Theory," In Schwartz, S. D, Ed. *Progress in Theoretical Chemistry and Physics*. pp. 117-184, 2000.

[95] Y. A. Wang, G. Niranjan, and E. A. "Carter Orbital-free kinetic-energy density functionals with a density-dependent kernel," *Phys. Rev. B* vol. 60, no. 16, p. 350, 1999.

[96] W. Kohn, and L. J. Sham, "Self-Consistent Equations Including Exchange and Correlation Effects," *Physical Review*, vol. 140, no. 4A, pp. A1133–A1138, 1965.

[97] A. J. Cohen, P. Mori-Sánchez, and W. Yang, "Challenges for density functional theory," *Chemical reviews*, vol. 112, no. 1, pp. 289-320, 2012.

[98] S. Reich, J. Maultzsch, C. Thomsen, and P. Ordejon, "Tight-binding description of graphene," *Physical Review B*, vol. 66, no. 3, p. 035412, 2002.

[99] A. P. Sutton, M. W. Finnis, D. G. Pettifor, and Y. Ohta, "The tight-binding bond model," *Journal of Physics C: Solid State Physics*, vol. 21, no. 1, p. 35, 1988.

[100] B. J. Leimkuhler, S. Reich, and R. D. Skeel, "Integration methods for molecular dynamics," In Mathematical Approaches to biomolecular structure and dynamics, *Springer*, New York, NY, pp. 161-185. 1996.

[101] L. Verlet, "Computer experiments on classical fluids. I. Thermodynamical properties of Lennard-Jones molecules," *Phys. Rev.*, vol. 159, no. 1, pp. 98–103, 1967.

[102] D. Frenkel, and B. Smit, "Understanding molecular simulation: from algorithms to application," *Academic Press*, San Diego, California, USA, 2002.

[103] R. T. Sanderson, "Chemical Bonds and Bond Energy," Academic: New York, 1976.

[104] C. Altona, and H. Hirschmann, "Empirical valence-force calculations of steroids—I: Conformations and relative energies of the 20-epimers of 5α-pregnane-3β, 20-diol", *Tetrahedron*, vol. 26, no. 9, pp. 2173-2183, 1970.

[105] N. C. Cohen, "Gemo, a computer program for the calculation of the preferred conformations of organic molecules," *Tetrahedron*, vol. 27, no. 4, pp. 789–797, 1971.

[106] N. L. Allinger, and F. Wu, "Conformational analysis—LXXVII: The relative stabilities of the isomeric androstane ring systems," *Tetrahedron*, vol. 27, no. 21, pp. 5093-5113, 1971.

[107] A. Lyubartsev, Y. Tu, and A. Laaksonen, "Hierarchical Multiscale Modelling Scheme from First Principles to Mesoscale," *Journal of Computational and Theoretical Nanoscience*, vol. 6, no. 5, pp. 951–959, 2009.

[108] C. Altona, and D. H. Faber, (n.d.), "Empirical force field calculations," *Dynamic Chemistry*, pp. 1–38.

[109] J. C. Fogarty, H. M. Aktulga, A. Y. Grama, A. C. T. van Duin, and S. A. Pandit, "A reactive molecular dynamics simulation of the silica-water interface," *The Journal of Chemical Physics*, vol. 132, no. 17, p. 174704, 2010.

[110] A. Warshel, "Molecular Dynamics Simulations of Biological Reactions*," Accounts of Chemical Research*, vol. 35, no. 6, pp. 385–395, 2002.

[111] J. Ziebarth, and Y Wang, "Molecular dynamics simulations of DNA-polycation complex formation," *Biophysical journal*, vol. 97, no. 7, pp. 1971-1983, 2009.

[112] R. Venkatasailanathan, W. C. N. Paul W, D. Sumitava, S. Shriram, D. B. Richard, and R. S. Venkat, "Modelling and Simulation of Lithium-Ion Batteries from a Systems Engineering Perspective." *Journal of Electrochemical Society*, vol, 159, no 3, pp. R31 – R45, 2011.

[113] G. Spavieri, G. T. Gillies, and M. Rodriguez, "Physical implications of Coulomb's Law," *MetroLogia*, vol. 41, no. 5, pp S159 – S170, 2004.

[114] ESPResSO Online Documentation, "Bonded and non-bonded interactions", https://espressomd.github.io/doc/ [Accessed Nov 13, 2020]

[115] S. L. Mayo, B. D. Olafson, and W. A. Goddard III, "DREIDING: a generic force field for molecular simulations," *Journal of Physical chemistry*, vol. 94, no. 26, pp. 8897-8909, 1990.

[116] A. Strachan, "From Atoms to Materials: Predictive Theory and Simulations," *nanoHUB-U* [Online]. Available: https://nanohub.org/courses/FATM/01a. [Accessed Nov 13, 2020]

[117] L. A. Girifalco and V. G. Weizer, "Application of the Morse potential function to cubic metals," *Physical Review*, vol. 114, no. 3, p. 687, 1959.

[118] S. M. Foiles, M. I. Baskes, M. S. Daw, "Embedded-atom-method functions for the fcc metals Cu, Ag, Au, Ni, Pd, Pt, and their alloys," *Physical review B*, vol. 33, no. 12, p. 7983, 1986.

[119] F. H. Stillinger, and T. A. Weber, "Computer simulation of local order in condensed phases of silicon" *Physical review B*, vol. 31, no. 8, p 5262,1985.

[120] H. M. Aktulga, S. A. Pandit, A. C. T. Van Duin, and A. Y. Grama, "Reactive molecular dynamics: Numerical methods and algorithmic techniques," *SIAM Journal on Scientific Computing*, vol. 34, no. 1, pp. C1-C23, 2012.

[121] J. Tersoff, *"*New empirical approach for the structure and energy of covalent systems," *Physical Review B,* vol. 37, no. 12, pp. 6991–7000, 1988.

[122] D. W. Brenner, Empirical potential for hydrocarbons for use in simulating the chemical vapor deposition of diamond films," *Physical Review B*, vol. 42, no. 15, pp. 9458–9471, 1990.

[123] J. Tersoff, "Carbon defects and defect reactions in silicon," *Physical review letters*," vol. 64, no. 15, p. 1757, 1990.

[124] K. B. Lipkowitz, and D. B. Boyd, "Reviews in Computational Chemistry," Volume 18. *John Wiley & Sons, Inc.* New Jersey, Canada

[125] T. Verstraelen, P. W. Ayers, V. Van Speybroeck, M. Waroquier, M. "8: Atom-condensed Kohn-Sham DFT approximated to second order," *The Journal of Chemical Physics,* vol. 138, no. 7, p. 074108, 2013.

[126] E. M. Pierce, P. Frugier, L. J. Criscenti, K. D. Kwon, and S. N. Kerisit, "Modeling interfacial glass-water reactions: recent advances and current limitations," *International Journal of Applied Glass Science,* vol. 5, no. 4, pp. 421 – 435, 2014.

[127] C. E. Wilmer, and R. Q. Snurr, "Towards rapid computational screening of metal-organic frameworks for carbon dioxide capture: Calculation of framework charges via charge equilibration," *Chemical Engineering Journal*, vol. 171, no. 3, pp. 775–781, 2011.

[128] A. Szabo, and S. N. Ostlund, "Modern quantum mechanics: introduction to advanced electronic structure theory," *Dover Publication Inc*. Mineola, NY, 1996.

[129] R. G. Mortimer, (3ed), "Physical Chemistry", *Elsevier Academic Press,* NY, 2008.

[130] A. Oda, and S. Hirono, "Geometry-dependent atomic charge calculations using charge equilibration method with empirical two-center Coulombic terms*," Journal of Molecular Structure: THEOCHEM,* vol. 634, no. 1-3, pp. 159–170, 2003.

[131] D. J. Griffith, "Introduction to quantum mechanics," *Prentise Hall Inc*. New Jersey, USA. 1994.

[132] J. N. Louwen, and E. T. C. Vogt, "Semi-empirical atomic charges for use in computational chemistry of molecular sieves," *Journal of Molecular Catalysis A*: Chemical, vol. 134, no. 1-3, pp. 63–77, 1998.

[133] M. P. Allen, and D. J. Tildesley, "Computer simulation of liquids," *Oxford University Press,* New York, NY 10016, United States of America, 2017.

[134] E. L. Pollock, and J. Glosli, "Comments on P3M, FMM, and the Ewald method for large periodic Coulombic systems," *Computer Physics Communications*, vol. 95, no. 2–3, pp. 93–110, 1996

[135] G. Sutmann, P. Gibbon, and T. Lippert, "Fast methods for long-range interactions in complex systems," *Forschungszentrum Jülich, IAS Series,* Vol. 6, 2011.

[136] S. W. de Leeuw, J. W. Perram, and E. R. Smith, "Simulation of electrostatic systems in periodic boundary conditions. I. Lattice sums and dielectric constants," *Proceedings of the Royal Society of London. A. Mathematical and Physical Sciences*, vol. 373, no. 1752, pp. 27–56, 1980.

[137] S. Kuwajima, and A. Warshel, "The extended Ewald method: A general treatment of long-range electrostatic interactions in microscopic simulations," *The Journal of chemical physics*, vol. 89, no. 6, pp. 3751 – 3759, 1988.

[138] J. Eastwood, and R. Hockney, "Shaping the force law in two-dimensional particle-mesh models*," Journal of Computational Physics*, vol. 16, no. 4, pp. 342–359, 1974.

[139] L. Greengard, and V. Rokhlin, "A fast algorithm for particle simulations*," Journal of Computational Physics,* vol. 73, no. 2, pp. 325–348, 1987

[140] D. N. Card, and J. P. Valleau, "Monte Carlo Study of the Thermodynamics of Electrolyte Solutions*," The Journal of Chemical Physics,* vol. 52, no. 12, pp. 6232–6240, 1970.

[141] J. C. Phillips, R. Braun, W. Wang, J. Gumbart, E. Tajkhorshid, E. Villa, C. Chipot, R. D. Skeel, L. Kael, and K. Schulten, "Scalable molecular dynamics with NAMD," *Journal of Computational Chemistry,* 26(16), 1781–1802, 2005.

[142] D. S. Shamshirgar, J. Bagge, and A.-K. Tornberg, "Fast Ewald summation for electrostatic potentials with arbitrary periodicity," *The Journal of Chemical Physics,* vol. 154, no. 16, p. 164109, 2021.

[143] J. Kolafa, and J. W. Perram, "Cutoff Errors in the Ewald Summation Formulae for Point Charge Systems," *Molecular Simulation,* vol. 9, no. 5, pp. 351–368, 1992.

[144] H. G. Petersen, "Accuracy and efficiency of the particle mesh Ewald method," *The Journal of Chemical Physics,* vol. 103, no. 9, pp. 3668–3679,1995.

[145] S. Y. Kim, A. C. T. van Duin, and J. D. Kubicki., "Molecular dynamics simulation of the interactions between TiO_2 nanoparticles and water with Na^+ and Cl^-, methanol, and formic acid using a reactive force field". *Journal of materials Research,* vol. 28, no. 03, pp. 513 – 520, 2013.

[146] R. S. Mulliken, "Electronic Population Analysis on LCAO–MO Molecular Wave Functions. I," *The Journal of Chemical Physics,* vol. 23, no. 10, pp. 1833–1840, 1955.

[147] L. Pauling, "Nature of the Chemical Bond, Third Ed.," *Cornell Univ. Press,* Ithaca, New York, 1960.

[148] R. G. Parr, and R. G. Pearson, "Absolute hardness: companion parameter to absolute electronegativity." *Journal of the American Chemical Society,* vol. 105, no. 26, pp. 7512–7516, 1983.

[149] P. Politzer, and H. Weinstein, "Some relations between electronic distribution and electronegativity," *The Journal of Chemical Physics,* vol. 71, no. 11, pp. 4218–4220, 1979.

[150] W. J. Mortier, S. K. Ghosh, and S. Shankar, "Electronegativity-equalization method for the calculation of atomic charges in molecules," *Journal of the American Chemical Society,* vol. 108, no. 15, pp. 4315–4320, 1986.

[151] D. Mathieu, "Split charge equilibration method with correct dissociation limits," *The Journal of Chemical Physics,* vol. 127, no. 22, p. 224103, 2007.

[152] J. Chen, and T. J. Martínez, "QTPIE: Charge transfer with polarization current equalization. A fluctuating charge model with correct asymptotic," *Chemical Physics Letters,* vol. 438, no. 4-6, pp. 315–320, 2007.

[153] J. Morales, and T. J. Martínez, "A New Approach to Reactive Potentials with Fluctuating Charges: Quadratic Valence-Bond Model," *The Journal of Physical Chemistry A*, vol. 108, no. 15, pp. 3076–3084, 2004.

[154] J. Cioslowski, and B. B. Stefanov, "Electron flow and electronegativity equalization in the process of bond formation," *The Journal of Chemical Physics*, vol. 99, no. 7, pp. 5151–5162, 1993.

[155] G. Lee Warren, J. E. Davis, and S. Patel, "Origin and control of superlinear polarizability scaling in chemical potential equalization methods," *The Journal of Chemical Physics*, vol. 128, no. 14, p. 144110, 2008.

[156] R. Chelli, P. Procacci, R. Righini, and S. Califano, "Electrical response in chemical potential equalization schemes," *The Journal of Chemical Physics*, vol. 111, no. 18, pp. 8569–8575 1999.

[157] J. L. Banks, G. A. Kaminski, R. Zhou, D. T. Mainz, B. J. Berne, and R. A. Friesner, "Parametrizing a polarizable force field from ab initio data. I. The fluctuating point charge model," *The Journal of Chemical Physics*, vol. 110, no. 2, pp. 741–754, 1999.

[158] L. Dosen-Micovic, D. Jeremic, and N. L. Allinger, "Treatment of electrostatic effects within the molecular-mechanics method. 1", *Journal of the American Chemical Society*, vol. 105, no. 7, pp. 1716–1722, 1983.

[159] S. Naserifar, D. J. Brooks, W. A. Goddard III, and V. Cvicek, "Polarizable charge equilibration model for predicting accurate electrostatic interactions in molecules and solids," *The Journal of Chemical Physics*, vol. 146, no. 12, p. 124117, 2017.

[160] A. Nakano, "Parallel multilevel preconditioned conjugate-gradient approach to variable-charge molecular dynamics," *Computer Physics Communications*, vol. 104, no. 1-3, pp. 59-69, 1997.

[161] C. Campañá, B. Mussard, and T. K. Woo, "Electrostatic Potential Derived Atomic Charges for Periodic Systems Using a Modified Error Functional," *Journal of Chemical Theory and Computation*, vol. 5, no. 10, pp. 2866–2878, 2009.

[162] C. E. Wilmer, K. C. Kim, and R. Q. Snurr, "An Extended Charge Equilibration Method," *The Journal of Physical Chemistry Letters*, vol. 3, no. 17, pp. 2506–2511, 2012.

[163] G. C. Martin-Noble, D. Reilley, L. M. Rivas, M. D. Smith, and J. Schrier, "EQEq+C: An Empirical Bond-Order-Corrected Extended Charge Equilibration Method," *Journal of Chemical Theory and Computation*, vol. 11, no. 7, pp. 3364–3374, 2015.

[164] K. D. Nielson, A. C. T. van Duin, J. Oxgaard, W.-Q. Deng, and W. A. Goddard III, "Development of the ReaxFF Reactive Force Field for Describing Transition Metal Catalyzed Reactions, with Application to the Initial Stages of the Catalytic Formation of Carbon Nanotubes," *The Journal of Physical Chemistry A*, vol. 109, no. 3, pp. 493–499, 2005.

[165] A. Strachan, A. C. T. van Duin, D. Chakraborty, S. Dasgupta, and W. A. Goddard, "Shock Waves in High-Energy Materials: The Initial Chemical Events in Nitramine RDX," *Physical Review Letters*, vol. 91, no. 9, 2003.

[166] K. Chenoweth, A. C. Van Duin, P. Persson, M. J. Cheng, J. Oxgaard, and W. A. Goddard III, "Development and application of a ReaxFF reactive force field for

oxidative dehydrogenation on vanadium oxide catalysts," *The Journal of Physical Chemistry C*, vol. 112, no. 37, pp. 14645-14654, 2008.

[167] W. Zhang, and A. C. T. van Duin, "Second-Generation ReaxFF Water Force Field: Improvements in the Description of Water Density and OH-Anion Diffusion," *The Journal of Physical Chemistry B*, vol. 121, no. 24, pp. 6021–6032, 2017.

[168] F. Castro-Marcano, A. M. Kamat, M. F. Russo, A. C. T. van Duin, J. P. Mathews, "Combustion of an Illinois No. 6 coal char simulated using an atomistic char representation and the ReaxFF reactive force field", *Combustion and Flame*, vol. 159, no. 3, pp. 1272–1285, 2012.

[169] K. Chenoweth, A. C. T. van Duin, and W. A. Goddard III, "ReaxFF Reactive Force Field for Molecular Dynamics Simulations of Hydrocarbon Oxidation," *J. Phys. Chem. A.* vol. 112, no. 5, pp. 1040 – 1053, 2008.

[170] G. M. Psofogiannakis, J. F. McCleerey, E. Jaramillo, and A. C. van Duin, "ReaxFF reactive molecular dynamics simulation of the hydration of Cu-SSZ-13 zeolite and the formation of Cu dimers," *The Journal of Physical Chemistry C*, vol. 119, no. 12, pp. 6678-6686, 2015.

[171] A. Lloyd, D. Cornil, A. C. T. Van Duin, D. van Duin, R. Smith, S. D. Kenny, J. Cornil, and D. Beljonne, "Development of a ReaxFF potential for Ag/Zn/O and application to Ag deposition on ZnO," *Surface Science*, vol. 645, pp. 67-73, 2016.

[172] F. Tavazza, T. P, Senftle, C. Zou, C. A. Becker, and A. T. van Duin, "Molecular dynamics investigation of the effects of tip–substrate interactions during nanoindentation," *The Journal of Physical Chemistry C*, vol. 119, no. 24, pp. 13580-13589, 2015.

[173] J. P. Perdew, K. Burke, and M. Ernzerhof, "Generalized Gradient Approximation Made Simple," *Physical Review Letters*, vol. 77, no. 18, pp. 3865–3868, 1996.

[174] G. Kresse, and J. Hafner, "Ab initio molecular dynamics for liquid metals," *Physical Review B*, vol. 47, no. 1, pp. 558–561, 1993.

[175] R. F. W. Bader, "Molecular fragments or chemical bonds," *Accounts of Chemical Research*, vol. 8, no. 1, pp. 34–40, 1975.

[176] R. F. W. Bader, P. J. MacDougall, and C. D. H. Lau, "Bonded and nonbonded charge concentrations and their relation to molecular geometry and reactivity," *Journal of the American Chemical Society*, vol. 106, no. 6, 1594–1605, 1984.

[177] W. J. Hehre, and J. A. Pople, "Molecular orbital theory of the electronic structure of organic compounds. III. Ab initio studies of charge distribution using a minimal Slater-type basis" *Journal of the American Chemical Society*, vol. 92, no, 8, pp., 2191–2197, 1970.

[178] K. L. Joshi, G. Psofogiannakis, A. C. T. van Duin, and S. Raman, "Reactive molecular simulations of protonation of water clusters and depletion of acidity in H-ZSM-5 zeolite", *Phys. Chem. Chem. Phys.*, vol. 16, no. 34, pp. 18433–18441, 2014.

[179] K. Ganeshan, Y. K. Shin, N. C. Osti, Y. Sun, K. Prenger, M. Naguib, M. Tyagi, E. Mamontov, D. Jiang, and A. C. T. van Duin, "Structure and Dynamics of Aqueous Electrolytes Confined in 2D-TiO2/Ti3C2T2 MXene Heterostructures", *ACS Applied Materials & Interfaces*, vol. 12, no. 52, pp. 58378–58389, 2020.

[180] A. Ostadhossein, S.-Y, Kim, E. D. Cubuk, Y. Qi, and A. C. T. van Duin, "Atomic Insight into the Lithium Storage and Diffusion Mechanism of SiO2/Al2O3 Electrodes of Lithium-Ion Batteries: ReaxFF Reactive Force Field Modeling", *The Journal of Physical Chemistry A*, vol. 120, no. 13, pp. 2114–2127, 2016.

[181] S. S. Han, A. C. T. van Duin, W. A. Goddard III, and H. M. Lee, "Optimization and Application of Lithium Parameters for the Reactive Force Field, ReaxFF," *The Journal of Physical Chemistry A*, vol. 109, no. 20, pp. 4575–4582, 2005.

[182] Y. K. Shin, M. Y. Sengul, A. S. M. Jonayat, W. Lee, E. D. Gomez, C. A. Randall, and A. C. T. van. Duin, "Development of a ReaxFF reactive force field for lithium ion conducting solid electrolyte Li1+xAlxTi2−x(PO4)3 (LATP)", *Physical Chemistry Chemical Physics*, vol. *20*, no. 34, pp. 22134-22147, 2018.

[183] A. K. Buckley, M. Lee, T. Cheng, R. V. Kazantsev, D. M. Larson, W. A. Goddard III, F. D. Toste, and F. M. Toma, "Electrocatalysis at Organic–Metal Interfaces: Identification of Structure–Reactivity Relationships for CO2 Reduction at Modified Cu Surfaces," *Journal of the American Chemical Society*, vol. 141, no. 18, pp. 7355–7364, 2019.

[184] S. K. Singh, S. G. Srinivasan, M. Neek-Amal, S. Costamagna, A. C. T. van Duin, F. M. Peeters, "Thermal properties of fluorinated graphene," *Physical Review B*, vol. 87, no. 10, 2013.

[185] A. Grzybowski, E. Gwóźdź, and A. Bródka, "Ewald summation of electrostatic interactions in molecular dynamics of a three-dimensional system with periodicity in two directions," *Physical Review B*, vol. 61, no. 10, pp. 6706–6712, 2000.

[186] A. Stukowski, "Visualization and analysis of atomistic simulation data with OVITO–the Open Visualization Tool," *Modelling and Simulation in Materials Science and Engineering*, vol. 18, no. 1, p. 015012, 2009.

[187] Y. Liu, W. Liu, Z. Wang, W. He, Q. Tang, Y. Xi, X. Wang, H. Guo, and C. Hu, "Quantifying contact status and the air-breakdown model of charge-excitation triboelectric nanogenerators to maximize charge density," *Nature Communications*, vol. 11, no. 1, pp. 1-8, 2020.

[188] S. Li, Y. Huang, D. Min, G. Qu, H. Niu, Z. Li, W. Wang, J. Li, and W. Liu, "Synergic effect of adsorbed gas and charging on surface flashover," *Scientific Reports*, vol. 9, no. 1, p. 5464, 2019.

[189] G. I. Guerrero-García, E. González-Tovar, M. Chávez-Páez, J. Kłos, and S. Lamperski, "Quantifying the thickness of the electrical double layer neutralizing a planar electrode: the capacitive compactness," *Physical Chemistry Chemical Physics*, vol. 20, no. 1, pp 262–275, 2018.

[190] H. Schreiber, and O. Steinhauser, "Cutoff size does strongly influence molecular dynamics results on solvated polypeptides," *Biochemistry*, vol. 31, no. 25, pp. 5856–5860, 1992.

[191] A. H. Castro Neto, F. Guinea, N. M. R. Peres, K. S. Novoselov, and A. K. Geim, "The electronic properties of graphene," *Reviews of Modern Physics*, vol. 81, no. 1, pp. 109–162, 2009.

[192] J. H. J. Ostrowski, and J. D. Eaves, "The Tunable Hydrophobic Effect on Electrically Doped Graphene," *The Journal of Physical Chemistry B,* vol. 118, no. 2, pp. 530–536, 2014.

[193] E. Persson, and B. Halle, "Nanosecond to Microsecond Protein Dynamics Probed by Magnetic Relaxation Dispersion of Buried Water Molecules," *Journal of the American Chemical Society,* vo. 130, no. 5, pp. 1774–1787, 2008.

[194] D. E. Moilanen, I. R. Piletic, and M. D Fayer, "Water Dynamics in Nafion Fuel Cell Membranes: The Effects of Confinement and Structural Changes on the Hydrogen Bond Network," *The Journal of Physical Chemistry C,* vol. 111, no. 25, pp. 8884–8891, 2007.

[195] C. Melios, C. E. Giusca, V. Panchal, and O. Kazakova, "Water on graphene: review of recent progress," *2D Materials,* vol. 5, no. 2, p. 022001, 2018.

[196] A. Aghigh, V. Alizadeh, H. Y. Wong, M. S. Islam, N. Amin, and M. Zaman, "Recent advances in utilization of graphene for filtration and desalination of water: A review," *Desalination,* vol. 365, pp. 389–397, 2015.

[197] A. A. B. Hamra, H. N. Lim, W. K. Chee, H. M. Huang, "Electro-exfoliating graphene from graphite for direct fabrication of supercapacitor," *Applied Surface Science,* vol. 360, pp. 213–223, 2016.

[198] A. Härtel, M. Janssen, S. Samin, and R. van. Roij, "Fundamental measure theory for the electric double layer: implications for blue-energy harvesting and water desalination." *Journal of Physics: Condensed Matter,* vol. 27, no. 19, p. 194129, 2015.

[199] D. Jiang, D. Meng, and J. Wu, "Density functional theory for differential capacitance of planar electric double layers in ionic liquids," *Chemical Physics Letters,* vol. 504, no. 4-6, pp. 153–158, 2011.

[200] R. S. Nicholson, "Theory and application of cyclic voltammetry for measurement of electrode reaction kinetics," *Analytical chemistry,* vol. *37,* no. 11, pp. 1351-1355, 1965.

[201] T. Liang, A. C. Antony, S. A. Akhade, M. J. Janik, and S. B. Sinnott, "Applied Potentials in Variable-Charge Reactive Force Fields for Electrochemical Systems," *The Journal of Physical Chemistry A,* vol. 122, no. 2, pp. 631–638, 2018.

[202] H. Nakano, and H. Sato, "A chemical potential equalization approach to constant potential polarizable electrodes for electrochemical-cell simulations," *The Journal of Chemical Physics,* vol. 151, no. 16, p. 164123, 2019.

[203] J. L. Siepmann, and M. Sprik, "Influence of surface topology and electrostatic potential on water/electrode systems," *The Journal of Chemical Physics,* vol. 102, no. 1, pp. 511–524, 1995.

[204] N. Onofrio, and A. Strachan, "Voltage equilibration for reactive atomistic simulations of electrochemical processes," *The Journal of Chemical Physics,* vol. 143, no. 5, p. 054109, 2015.

[205] C. Merlet, C. Péan, B. Rotenberg, P. A. Madden, B. Daffos, P.-L Taberna, P. Simon, and Salanne, M. "Highly confined ions store charge more efficiently in supercapacitors," *Nature Communications,* vol. 4, no. 1, pp. 1-6, 2013.

[206] C. Merlet, C. Péan, B. Rotenberg, P. A. Madden, P. Simon, and M. Salanne, "Simulating Supercapacitors: Can We Model Electrodes As Constant Charge Surfaces?," *The Journal of Physical Chemistry Letters*, vol. 4, no. 2, pp. 264–268, 2012.

[207] Z. Li, G. Jeanmairet, T. Méndez-Morales, B. Rotenberg, and M Salanne, "Capacitive Performance of Water-in-Salt Electrolyte in Supercapacitors: A Simulation Study," *The Journal of Physical Chemistry C*. vol. 122, no. 42, pp. 23917-23924, 2018.

[208] D. T. Limmer, "Interfacial Ordering and Accompanying Divergent Capacitance at Ionic Liquid-Metal Interfaces," *Physical Review Letters*, vol. 115, no. 25, p. 256102, 2015.

[209] J. Le Ma, Q. Meng, and J. Fan, "Charge driven lateral structural evolution of ions in electric double layer capacitors strongly correlates with differential capacitance." *Physical Chemistry Chemical Physics*, vol. 20, no. 12, pp. 8054–8063, 2018.

[210] C. Merlet, D. T. Limmer, M. Salanne, R. van Roij, P. A. Madden, D. Chandler, and B. Rotenberg, "The Electric Double Layer Has a Life of Its Own," *The Journal of Physical Chemistry C*, vol. 118, no. 32, pp. 18291–18298, 2014.

[211] O. Borodin, X. Ren, J. Vatamanu, A. von Wald Cresce, J. Knap, and K. Xu, "Modeling Insight into Battery Electrolyte Electrochemical Stability and Interfacial Structure," *Accounts of Chemical Research*, vol. 50, no. 12, pp. 2886–2894, 2017

[212] D. Laage, "A Molecular Jump Mechanism of Water Reorientation," *Science*, vol. 311, no. 5762, pp. 832–835, 2006.

[213] T. Ohto, H. Tada, and Y. Nagata, "Structure and dynamics of water at water–graphene and water–hexagonal boron-nitride sheet interfaces revealed by ab initio sum-frequency generation spectroscopy*," Physical Chemistry Chemical Physics*, vol. 20, no. 18, pp. 12979–12985, 2018.

[214] G. Stirnemann, F. Sterpone, and D. Laage, "Dynamics of Water in Concentrated Solutions of Amphiphiles: Key Roles of Local Structure and Aggregation," *The Journal of Physical Chemistry B*, vol. 115, no. 12, pp. 3254–3262, 2011.

[215] R. Smith, K. Jolley, C. Latham, M. Heggie, A. van Duin, D. van Duin, and H. Wu, "A ReaXFF carbon potential for radiation damage studies," *Nuclear Instruments and Methods in Physics Research Section B: Beam Interactions with Materials and Atoms*, vol. 393, pp. 49–53, 2017.

[216] G. Cicero, J. C. Grossman, E. Schwegler, F. Gygi, and G. Galli, "Water confined in nanotubes and between graphene sheets: A first principle study," *Journal of the American Chemical Society*, vol. 130, no. 6, pp. 1871-1878, 2008.

[217] S. Ruiz-Barragan, D. Muñoz-Santiburcio, and D. Marx, "Nanoconfined Water within Graphene Slit Pores Adopts Distinct Confinement-Dependent Regimes," *The Journal of Physical Chemistry Letters*, vol. 10, no. 3, pp. 329–334, 2018.

[218] I.-C. Yeh, and M. L. Berkowitz, "Dielectric constant of water at high electric fields: Molecular dynamics study," *The Journal of Chemical Physics*, vol. 110, no. 16, pp. 7935 – 7942, 1999.

[219] C. Calero, J. Martí, E. Guàrdia, and M. Masia, "Characterization of the Methane–Graphene Hydrophobic Interaction in Aqueous Solution from Ab Initio Simulations," *Journal of Chemical Theory and Computation*, vol. 9, no. 11, pp. 5070–5075, 2013.

[220] I.-C. Yeh, and M. L. Berkowitz, "Structure and dynamics of water at water|Pt interface as seen by molecular dynamics computer simulation," *Journal of Electroanalytical Chemistry*, vol. 450, no. 2, pp 313–325, 1998.

[221] L. B. Skinner, C. Huang, D. Schlesinger, L. G. Pettersson, A. Nilsson, and C. J. Benmore, "Benchmark oxygen-oxygen pair-distribution function of ambient water from x-ray diffraction measurements with a wide Q-range," *The Journal of chemical physics*, vol. *138*, no. 7, p. 074506, 2013.

[222] A. K. Soper, "The radial distribution functions of water as derived from radiation total scattering experiments: Is there anything we can say for sure?," *International Scholarly Research Notices*, vol. 2013, 2013.

[223] M. Chen, H. Y. Ko, R. C. Remsing, M. F. Calegari Andrade, B. Santra, Z. Sun, A. Selloni, R. Car, M. L. Klein, J. P. Perdwe and X. Wu, "Ab initio theory and modeling of water," *Proceedings of the National Academy of Sciences*, vol. 114, no. 41, pp. 10846-10851, 2017.

[224] Y. Zhang, G. Stirnemann, J. T. Hynes, and D. Laage, "Water dynamics at electrified graphene interfaces: a jump model perspective," *Physical Chemistry Chemical Physics*. Vol. 22, no. 19, pp.10581-10591, 2020.

[225] B. Demir, and D. Searles, "Investigation of the Ionic Liquid Graphene Electric Double Layer in Supercapacitors Using Constant Potential Simulations," *Nanomaterials*, vol. 10, no. 11, p. 2181, 2020.

[226] Z. Wang, Y. Yang, D. L. Olmsted, M. Asta, and B. B. Laird, "Evaluation of the constant potential method in simulating electric double-layer capacitors," *The Journal of Chemical Physics*, vol. 141, no. 18, p. 184102, 2014.

[227] M. V. Fedorov, and A. A. Kornyshev, "Ionic Liquids at Electrified Interfaces," *Chemical Reviews*, vol. 114, no. 5, pp. 2978–3036, 2014.

[228] A. P. Willard, S. K. Reed, P. A. Madden, and D. Chandler, "Water at an electrochemical interface—a simulation study," *Faraday Discuss*, vol. 141, pp 423–441, 2009.

[229] R. Parsons, "Electrochemical nomenclature," *Pure and Applied Chemistry*, vol. 37, no. 4, pp. 499–516, 1974.

[230] A. A. Kornyshev, "Double-Layer in Ionic Liquids: Paradigm Change?," *The Journal of Physical Chemistry B*, vol. 111, no. 20, pp. 5545–5557, 2007.

[231] D. T. Limmer, C. Merlet, M. Salanne, D. Chandler, P. A. Madden, R. van Roij, and B. Rotenberg, "Charge Fluctuations in Nanoscale Capacitors," *Physical Review Letters*, vol. 111, no. 10, p. 106102, 2013.

[232] Z. Wang, D. L. Olmsted, M. Asta, and B. B. Laird, "Electric potential calculation in molecular simulation of electric double layer capacitors," *Journal of Physics: Condensed Matter*, vol. 28, no. 46, p. 464006, 2016.

[233] J. N. Sachs, P. S. Crozier, and T. B. Woolf, "Atomistic simulations of biologically realistic transmembrane potential gradients," *The Journal of Chemical Physics*, vol. 121, no. 22, p. 10847, 2004.

[234] G. Feng, J. S. Zhang, and R. Qiao, "Microstructure and Capacitance of the Electrical Double Layers at the Interface of Ionic Liquids and Planar Electrodes," *The Journal of Physical Chemistry C*, vol. 113, no. 11, pp. 4549–4559, 2009.

[235] C. Merlet, M. Salanne, B. Rotenberg, and P. A. Madden, "Imidazolium ionic liquid interfaces with vapor and graphite: interfacial tension and capacitance from coarse-grained molecular simulators," *The Journal of Chemical Chemistry C*, vol. 115, no. 33, pp. 16613-16618, 2011.

[236] G. Feng, R. Qiao, J. Huang, S. Dai, B. G. Sumpter, and V. Meunier, "The importance of ion size and electrode curvature on electrical double layers in ionic liquids," *Physical Chemistry Chemical Physics*, vol. 13, no. 3, pp. 1152-1161, 2011.

[237] S. A. Kislenko, I. S. samoylov, and R. H. Amirov, "Molecular dynamics simulation of the electrochemical interface between a graphite surface and the ionic liquid [BMIM][PF 6]", *Physical Chemistry Chemical Physics*, vol. 11, no. 27, pp. 5584-5590, 2009.

[238] A. Y. Toukmaji, and J. A. Board, "Ewald summation techniques in perspective: a survey," *Computer Physics Communications*, vol. 95, no. 2-3, pp. 73–92, 1996.

[239] C. J. Fennell, and J. D. Gezelter, "Is the Ewald summation still necessary? Pairwise alternatives to the accepted standard for long-range electrostatics," *The Journal of Chemical Physics*, vol. 124, no. 23, p. 234104, 2006.

[240] P. E. Smith, and B. M. Pettitt, "Efficient Ewald electrostatic calculations for large systems," *Computer Physics Communications*, vol. 91, no. 1-3, pp. 339–344, 1995.